Ricardo Morel Hartmann

ESTUDO EXPERIMENTAL DA IGNIÇÃO, INFLAMABILIDADE E PROPAGAÇÃO DE CHAMA DE QUEROSENE DE AVIAÇÃO SOB CONDIÇÕES LAMINAR E TURBULENTA

Tese submetida ao Programa de Pós-Graduação em Engenharia Mecânica da Universidade Federal de Santa Catarina para a obtenção do Grau de Doutor em Engenharia Mecânica.
Orientador: Prof. Amir A. M. de Oliveira Jr., Ph.D.
Coorientador: Prof. Robert Schiessl, Dr.-Ing.

Florianópolis
2016

Ficha de identificação da obra elaborada pelo autor,
através do Programa de Geração Automática da Biblioteca Universitária da UFSC.

Hartmann, Ricardo Morel
Estudo experimental da ignição, inflamabilidade e propagação de chama de querosene de aviação sob condições laminar e turbulenta / Ricardo Morel Hartmann ; orientador, Amir Antônio Martins de Oliveira Jr. ; coorientador, Robert Schiessl . - Florianópolis, SC, 2016.
204 p.

Tese (doutorado) - Universidade Federal de Santa Catarina, Centro Tecnológico. Programa de Pós-Graduação em Engenharia Mecânica.

Inclui referências

1. Engenharia Mecânica. 2. Querosene de aviação. 3. Inflamabilidade e propagação de chamas pré-misturadas. 4. Biocombustível HEFA. 5. Combustão. I. , Amir Antônio Martins de Oliveira Jr.. II. , Robert Schiessl. III. Universidade Federal de Santa Catarina. Programa de Pós-Graduação em Engenharia Mecânica. IV. Título.

Ricardo Morel Hartmann

ESTUDO EXPERIMENTAL DA IGNIÇÃO, INFLAMABILIDADE E PROPAGAÇÃO DE CHAMA DE QUEROSENE DE AVIAÇÃO SOB CONDIÇÕES LAMINAR E TURBULENTO

Esta Tese foi julgada adequada para obtenção do Título de "Doutor em Engenharia Mecânica",e aprovada em sua forma final pelo Programa de Pós-Graduação em Engenharia Mecânica.

Florianópolis, 29 de Fevereiro de 2016.

_____

Prof. Armando Albertazzi Gonçalves Jr., Dr. Eng.
Coordenador do Curso

_____

Prof. Amir Antônio Martins de Oliveira Jr., Ph.D. – Orientador

_____

Prof. Robert Schiessl, Dr.-Ing. – Coorientador
Karlsruher Institut für Technologie

Banca Examinadora:

_____

Prof. Amir Antônio Martins de Oliveira Jr., Ph.D – Orientador
Universidade Federal de Santa Catarina

_____

Prof. Cristiane Aparecida Martins, Dr.
Instituto Técnico da Aeronáutica

_____

Edimilson Jesus de Oliveira, Dr.
CENPES/Petrobras

_____

Prof. Juan Pablo de Lima Costa Salazar, Ph.D.
UFSC/Joinville

_____

Prof. Jader Riso Barbosa Jr., Ph.D.
EMC/UFSC

_____

Prof. Edson Bazzo, Dr.
EMC/UFSC

To my parents. To all the former scholars of philosophy and science who devoted their skills and verve to develop the modern human knowledge.

ACKNOWLEDGEMENTS

The acknowledgement of an entire life work, like an engineering thesis, it is not an easy task. But in the end, the issue essentially is to determine the boundaries of the *acknowledgement control volume*.
Firstly, thanks to my parents, who show beautiful examples of motivation, overcoming and work, but never forget to smile and enjoy the life. I would like to thank the Brazilian National Scientific and Technological Council (CNPq) by the scholarships. Special thanks to Petrobras by supporting the project, mainly to Dr. Edimilson Oliveira, CENPES/Petrobras, who have always helped, encouraged and exchanged important insights about high performance fuel engineering.
To friends and colleagues. To all my friends in Brazil, from the undergraduate and graduate periods. Thanks to LABCET colleagues, that gave me nice insights and posed interesting questions during coffee times, football matches or happy hours. Especially to Ms. Eng. Amir. R. de Toni Jr. by the discussions about Jet fuels. To the engineer João Dourado Monteiro and Ms. Eng. Eduardo Hartmann, by the distinguished help with the experiments in Brazil, during the period I was in Germany.
To the friends and colleagues in Germany. To Dipl.-Ing. Marc Werler by the help in the experiments, bike rides and friendship, something hard to achieve in the German standards. To Dr. Heiner Wirbser by the help in lab activities and to tell me the secret about the best German beer, the so called "Frei Bier". To Dr. Robert Schiessl who always helped and guided me during all my period in Germany, telling histories about the Germany and Europe, about the Bayern München club and by inspiring talks about combustion and science in general.
Finally, I would like to thank prof. Ulrich Maas, who kindly received me at the Institute of Technical Thermodynamics of the KIT-Karslruhe/Germany, and to all my science masters at EMC/UFSC, specially prof. Edson Bazzo and prof. Amir Oliveira, who have guided and inspired me through the last 15 years.

Fueled by the energy from the challenge.
Inspired to overcome the entropic constraints of the nature.

RESUMO

Turbinas a gás aeronáuticas combinam uma alta relação potência/peso, desempenho eficiente e confiabilidade. Em uma câmara de combustão típica de turbinas aeronáuticas, é comum observar temperaturas de admissão da ordem de 750 K, pressões de 20 bar e velocidades média do escoamento de 100 m/s. Fenômenos de fase gasosa que limitam as taxas de combustão, durabilidade e emissões, afetando negativamente o desempenho da máquina, incluem os fenômenos da extinção de chama turbulenta, *Blow-off* para misturas pobres e *Relight*. A legislação sobre o tema tem avançado no sentido de impor o aumento na adição de biocombustíveis na indústria da aviação, como por exemplo a utilização de biocombustível tipo HEFA (*Hydro-Processed Ester Fatty Acid*). Este trabalho enfoca o efeito da adição de um tipo de biocombustível HEFA ao QAV1 (querosene de aviação), criando uma mixtura de combustível alternativo para aviação comercial. Para tanto, foi utilizado uma mistura substituta para reproduzir as caracteristícas físico-químicas de um querosene de aviação sintético tipo HEFA. Experimentos com metodologia canônica foram então utilizados para medir tempo de retardo de ignição, limite de inflamabilidade para misturas laminares, propação de chamas laminares e turbulentas e extinção de núcleo da chama (*flame kernel*) sob condições turbulentas. O tempo de retardo de ignição foi medido utilizando-se uma máquina de compressão rápida (RCM) para mixturas com razão de equivalência entre 0,3 até 1,3, pressões de 7 bar, 10 bar e 15 bar e temperaturas variando entre 650 K até 950 K. A ignição forçada, a propação e extinção de chama foram medidos utilizando-se dois reatores de volume contante (CVR). Um CVR esférico com volume de 15 litros foi utilizado para detectar ignição, utilizando um sistema de fotografia de alta velocidade Schlieren Tipo Z usando uma câmera CMOS capaz de obter 10.000 fotos por segundo. O mesmo CVR foi também utilizado para medir a velocidade de chama laminar aplicando o método da medição do perfil transiente de pressão interna do reator, para misturas com razão de equivalência entre 0,8 até 1,3, pressão inicial de 1 bar e temperatura inicial de 408 K. Com o objetivo de obter a velocidade de chama diretamente da curva de pressão transiente, desenvolveu-se um código computacional em linguagem FORTRAN, assumindo hipótese de gás ideal, equilíbrio termodinâmico e sucessivas compressões isentrópicas para reagentes e produtos. A propagação e extinção de chamas turbulentas foram medidos utilizando-se um CVR cilíndrico com volume de 55 litros, para mixturas com razão de equivalência entre 0,8 até 1,3, pressão inicial de 1 bar e temperatura inicial de 310 K. A

existência de um núclo inicial de chama foi detectado utilizando-se uma câmera do tipo ICCD, e subsequentemente, o perfil transiente de pressão foi medido para o cálculo da velocidade de chama turbulenta. Os resultados mostraram um aumento da velocidade de chama laminar entre 5-7% com a utilização do bio-aditivo. A velocidade de chama turbulenta apresentou um menor percentual de aumento, aproximadamente 2% para os maiores níveis de turbulência testados. O tempo de retardo de ignição e o limite inferior de inflamabilidade diminuiram aproximadamente 3% com a utilização do bio-aditivo, reduzindo assim também as limitações de operacionalidade devido a extinção de chama turbulenta. A análise conjunta das taxas de propagação de chama, ignição, limites de inflamabilidade e extinção de chama turbulenta indicaram um sensível aumento na estabilidade operacional de turbinas a gás aeronáuticas sob as condições testadas com a adição do biocombustível substituto.

Palavras-chave: Querosene de aviação, tempo de retardo de ignição, inflamabilidade e extinção, velocidade de chama turbulenta, substituto HEFA, combustão.

ABSTRACT

Jet engines combine a high power to weight ratio with efficient performance and reliable operation. In the combustion chamber of typical jet engines, inlet temperatures of 750 K, pressure of 20 bar and axial flow velocities of 100 m/s are common. Gas phase phenomena that limit the combustion rate, durability and emissions, affecting negatively the engine performance, include turbulent flame extinction, lean blow-off, and relight. Legislation recently advanced has enforced the increase in the content of biofuels in the aviation industry, such as the use of HEFA (hydro-processed ester fatty acid) fuels. This work focus on the effect of the addition of a HEFA biofuel to the Brazilian Jet A-1 fuel, creating alternative jet fuel mixtures. Here, a surrogate fuel mixture was used to reproduce the basic combustion physicochemical characteristics of a HEFA based aviation fuel. Then, canonical experiments were used to measure ignition delay time, laminar flammability limits, laminar and turbulent flame propagation and extinction. Ignition delay time was measured in a rapid compression machine (RCM) for equivalence ratios from 0.3 to 1.3, pressures of 7 bar, 10 bar and 15 bar, and temperatures from 650 K to 950 K. Flame ignition, propagation and extinction were measured using two constant volume reactors (CVR). A 15 liters, spherical CVR with optical access was used to detect ignition, using a Z-type Schlieren photography with a 10000 fps CMOS camera, and to measure the laminar flame speed from the pressure transient trace, for equivalence ratio from 0.8 to 1.3, pressure of 1 bar, and temperature of 408 K. In order to predict the burning velocity from the pressure trace, a FORTRAN code was written assuming the products in full equilibrium and both, reactants and products, are treated as ideal gases and follow isentropic compression. Turbulent flame propagation and extinction was measured for methane and PRF fuel using a 55 liters, cylindrical, turbulent CVR for equivalence ratio of 0.8 to 1.3, pressure of 1 bar, and temperature of 300 K and 310 K. The existence of a flame kernel was detected using an ICCD camera and, following combustion, the transient pressure trace was measured. The results show the laminar flame speed has increased about 5-7% with the biofuel additive. The turbulent flame speed has a lower increase of about 2% at the higher turbulence intensities tested. The ignition delay time and the lower flammability limit decreased in about 3% with the addition of the biofuel surrogate, thus reducing the limitations on turbulent flame kernel extinguishment. The joint behavior in terms of burning rates, ignition, flammability limits, and turbulent flame kernel extinguishment indicated a slight increase in

the jet engine operational stability under the conditions tested with the use of the biofuel surrogate.

Keywords: Jet Biofuels. Ignition delay time. Flammability and Extinction. Turbulent Burning Velocity. HEFA Surrogate. Combustion.

LIST OF FIGURES

LIST OF TABLES

ACRONYMS

AVGAS	Aviation Gasoline
BDC	Bottom Dead Center.
BOCLE	Ball-on-Cylinder Lubricity Evaluator
CEA	Chemical Equilibrium with Applications
CFD	Computational Fluid Dynamics
CMOS	Complementary Metal Oxide Semiconductor. A type of digital camera technology.
CNPq	Brazilian Science and Technology Council
CtL	Coal to Liquid
CVR	Constant Volume Reactor.
EU	European Union
FAE	Fatty Acid Esther.
FAME	Fatty Acid Methyl Esther.
FT	Fischer-Tropsch
GRIMECH	Gas Research Institute MECHanism
GtL	Gas to Liquid
HDS	Hydrodesulfurization
HEFA	Hydro Treated Esther and Fatty Acid.
IC	Internal Combustion
ICCD	Intensified Charge Coupled Device. A type of digital camera technology.
IDT	Ignition Delay Time
IPK	Iso Parafinic Kerosene
ITT	Institute of Technical Thermodynamics
JANAF	Joint Army Navy and Air Force
Jet A	Commercial denomination of kerosene type fuel. Civil use in the US market.
Jet A-1	Commercial denomination of kerosene type fuel. Civil use, international market.

JP-1	Jet Propulsion #1. A type of kerosene fuel. Military use.
JP-10	Jet Propulsion 10. A type of kerosene fuel. Military use.
JP-5	Jet Propulsion #5. A type of kerosene fuel. Military use.
JP-8	Jet Propulsion #8. A type of kerosene fuel. Military use.
KIT	Karlsruhe Institute of Technology
LDA	Laser Doppler Anemometry
LTO	Landing and Take-off Cycle
MIE	Minimum Ignition Energy.
NASA	National Aeronautics and Space Administration (US Government Agency)
NTC	Negative Temperature Coefficient
QAV1	Querosene de Aviação (Brazilian Jet A-1)
R&D	Research and Devlopent
RCM	Rapid Compression Machine.
RMS	Root Mean Square
TDC	Top Dead Center.
UFSC	Universidade Federal de Santa Catarina (University of Santa Catarina)
USA/US	United States of America (Country)
USAF	United States Air Force

LIST OF SYMBOLS

Greek:

α	[m²/s]	Thermal diffusivity
$\boldsymbol{\beta}$	[-]	Probability Coeficient
γ	[-]	Ratio of specific heats
Δ	[-]	Finite difference
ε	[m²/s³]	Turbulent Energy dissipation rate
η	[m]	Length scale
κ	[1/s]	Stretch rate
ν	[m²/s]	Momentum Diffusivity/kinematic viscosity
ρ	[kg/m³]	Density
τ	[s]	Characteristic time
Φ	[-]	Fuel equivalence ratio
ω	[kg/m³-s]	Reaction rate/coefficient of proportionality

Latins:

A	[m²/s]	Area
D	[m]	Diameter
Da	[-]	Damköhler Number
E	[kJ]	Energy
H/C	[-]	Hydrogen to carbon ratio
k	[kmol/m³-s]	Reaction rate constante
Ka	[-]	Karlovitz Number
Ma	[-]	Markstein Number
p	[atm], [bar], [kPa]	Pressure
r	[m]	Radius
R	[kJ/kmol-K]	Universal Constant of the Gases
Re	[-]	Reynolds Number
s	[kJ/kg-K]	Entropy
S	[m/s]	Speed
T	[K]	Temperature
t	[s]	Time
u	[kJ/kg], [m/s]	Internal energy, speed
$\hat{u}$	[-]	Unity normal vector

v	[m³]	Volume
V	[m/s]	Velocity
x	[-]	Mass fraction
y	[-]	Mole fraction

SUB AND SUPERSCRIPTS

b	Burned.
bg	Burned gases
c	Chemical
D	Diffusive
G	Gibbs turbulent scale
L	Laminar
T	Turbulent
th	Thermal.
u	Unburned.
ug	Unburned gases
κ	Kolmogorov turbulent scale
'	Turbulent fluctuation
^{o}	Refference state

TABLE OF CONTENTS

1 INTRODUCTION

The impact of human activities on global climate change has become an important issue, affecting economic and social development. Despite the debate on the amount of the human contribution and the required measures to counter act it, the direct course of global warming continues. The concerns on pollution and climate change have been fundamental in establishing metrics to measure the amount of change, regulating the emissions in the industrial, energy and transportation sectors and actively increasing the efficiency of combustion systems and sustainability of the use of fuels.

1.1 Motivation

The daily jet fuel consumption in the European Union is about 1.4 million barrels of kerosene, which corresponds to 1.6% of the world fuel consumption. The EU consumption of jet fuel leads to an emission of 551,000 tons of CO_2 per day. The problem of assessing the effect caused by this amount of fuel consumption remains. However, it is a consensus that this path can only be reversed through innovation in the way we move around and, in short term, in the way we use the available resources as fuels. (Nair & Paulose, 2014) discussed the emergence of a new “green business model” for aviation biofuels obtained from algae. They presented the whole intrinsic web of relationships and knowledge involved in this kind of new emergent business model, having distinct social, political, environmental, economic, technological, and business dimensions. Figure 1.1 shows the author´s suggested economic Kondratiev cycles and the waves of innovation directly related to the new aviation business model.

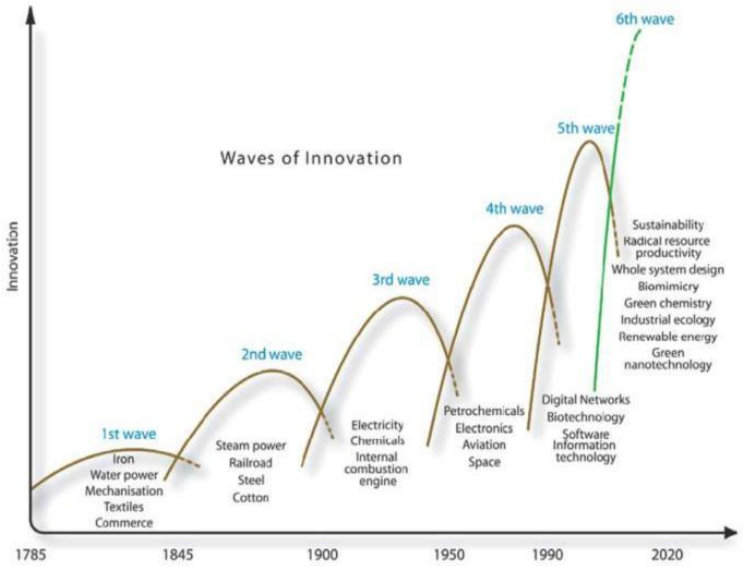

Figure 1.1– Kondratiev cycles and waves of innovation. Adapted from (Nair & Paulose, 2014).

The emergent biofuel green business model was considered as an example of the next-practice platform that could drive a sixth wave of innovation. It is interesting to note that the periods of the Kondratiev cycles became shorter with time while the amplitude of the innovation required to complete a given wave became progressively higher. Thus, the new aviation biofuel industry is expected to be very intensive in generation of innovations to fulfill the waves to come.

In terms of growth, the aviation industry has yet a large room for expansion. The so called emergent countries have huge potential markets. Comparing, for example, US and Brazil, both countries have almost the same surface area and comparable populations, about 300 million inhabitants in USA and 210 million in Brazil. However, as shown in Figure 1.2, the number and coverage of air routes present a higher density in US than in Brazil, with 11 times more aircrafts in service.

(Padilha, 2015) mentions the Brazilian aviation market has experienced an annual growth of 10% in the period 2004 – 2014. In the same period, the price of tickets decreased about 50%. A projection for the next 20 years forecasts a mean annual growth of 5.2%, increasing from 214 million of passengers in 2014 to 618 million passengers in 2035. The

projected Brazilian market growth is expected to be sustained also by the internal market growth. Considering only the regional airports, the forecasts project an annual growth of 9%, from 18 million passengers in 2014 to 118 million in 2035. Figure 1.3 shows the projected new regional airports in Brazil.

Since the Brazilian domestic aviation market is expected to present a remarkable growth, the same is valid for the aviation fuels and bio-additives market, whose projected growth will be strongly driven by R&D and innovation. Also, it is expected that some of those innovations will act as driving forces to economic and social development. Additionally, the use of bio-additives can save a huge amount of CO_2 emissions. Following (EPE, 2015), the consumption of Jet fuels in the Brazilian market in 2014 was about 28 million barrels. If 50% of this amount of jet fuel would be replaced by renewable fuels, the emission of about 5.2 million tons of CO_2 per year could be avoided. Following (Reis, 2011) the aviation industry is working with a goal to reduce the global CO_2 emissions in 2050 to 50% of the 2005 level.

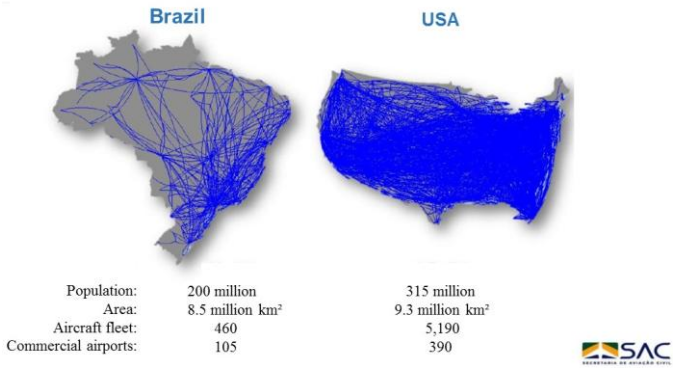

Figure 1.2– Main airway routes of Brazil and the USA (EUA). Adapted from (Padilha, 2015).

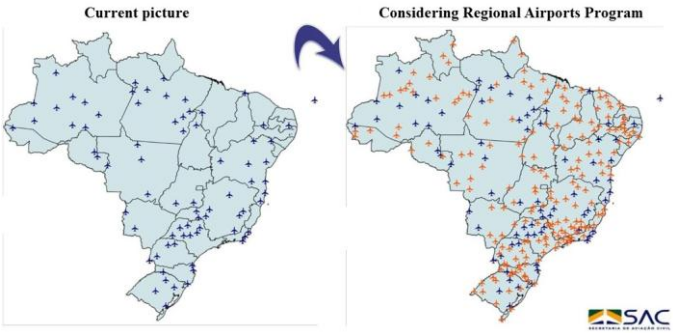

Figure 1.3– Comparison maps of the projected Brazilian Regional Airports. Adapted from (Padilha, 2015).

1.2 Objectives

The main goal of this work is to contribute to the assessment of the effects of the addition of bio-additives to the Brazilian Jet A-1 fuel in the gas-phase combustion within the combustion chamber of aviation gas turbines. The strategy used is: (1) To approximate the main chemical effects of the addition of HEFA – Hydro-processed Esther Fatty Acid bioadditives by using a surrogate formed by two chemical species, (2) to perform basic laboratory measurements of ignition delay time, laminar flammability limits, laminar and turbulent flame propagation and extinction; and (3) to perform a comprehensive interpretation of the results obtained from the point of view of combustion in aviation gas turbines.

The measurements were performed in the way to assess the gas phase combustion behavior in the jet engine combustion chamber. In this methodology, a set of experimental facilities are employed, instead a real jet engine, to obtain specific results of interest, under well controlled conditions. The measurements were carried out in two different laboratories, the Laboratory for Combustion and Thermal Systems Engineering – LABCET at UFSC, Florianópolis, Brazil, and the Institute of Technical Thermodynamics – ITT of the Karlsruhe Institute of Technology – KIT, in Karlsruhe, Germany. The work at the ITT/KIT was developed during a Sandwich Doctorate period, sponsored by the Brazilian Scientific and Technological Council – CNPq.

1.3 Overview of the Thesis Work

The jet fuel used in this work was the Brazilian commercial Jet A-1 fuel. The Jet A-1 sample was provided by Petrobras – Petróleo Brasileiro S.A. In Brazil, the commercial denomination of the Jet A-1 is QAV1 - "Querosene de Aviação 1". The provided sample was submitted to all the performance tests required by the International Civil Aviation Organization – ICAO and ASTM. The QAV1 sample was in accordance with all the mandatory tests. Table 1.1 summarizes the main physicochemical characteristics of the QAV1 sample.

Table 1.1– Physicochemical characteristics of the QAV1 sample. Source: Internal report.

Characteristics	Standard	Value
Density@15ºC, kg/m³	ASTM D4052	818.5
Density@20ºC, kg/m³	ASTM D4052	815.1
Kinematic Viscosity@20ºC, cSt	ASTM D7042	4.518
Total % Mass of carbon	ASTM D5373	86.45
Total % Mass of hydrogen	ASTM D5373	13.55
Molar mass, g/mol	GC/MS	160
Mean empirical formula	Calculated	$C_{11.53}H_{21.70}$
Saturated Hydrocarbons (%m/m)	ASTM D1319	76.4
Oleffinic Hydrocarbons (%m/m)	ASTM D1319	0.2
Monoaromatic Hydrocarbons (%m/m)	ASTM D1319	21.1
Diaromatic Hydrocarbons (%m/m)	ASTM D1319	2.1
Poliaromatic Hydrocarbons (%m/m)	ASTM D1319	0.2

The structure and properties of the HEFA type biofuel will be described in Section 2.2. The use of HEFA bioadditives is internationally regulated by the ASTM D7566 – 14a Standard (ASTM International, 2014). Besides the suitable properties, the future projections of the Brazilian Aviation programs and availability of different crops and feedstocks were also considered in selecting HEFA. As it will be presented in chapter Section 2.2, babassu, coconut and palm oils present a major fraction of fatty acid molecules having 12 carbons (C_{12}). These crops are among the feedstocks available in Brazil for the production of HEFA fuels, as illustrated in Figure 1.4. In the future, jatropha and

peanut crops could also be considered as supplementary candidates. Furthermore, considering the regional aviation growth forecasted for the Brazilian market and since the Brazilian offshore petroleum production is concentrated mainly in São Paulo and Rio de Janeiro states, the use of local feedstocks for aviation biofuels is environmentally and economically advantageous.

After the selection of a target HEFA composition, formed primarily by normal alkanes and iso-alkanes with 12 carbon atoms, a suitable surrogate must be formulated. The basic rules applied here are: (1) The surrogate must reproduce the carbon to hydrogen ratio of the HEFA fuel, (2) the physicochemical properties must remain within the limits fixed by the regulations, and (3) the composition must be amenable to theoretical treatment using detailed chemical kinetic mechanisms. Following these rules, and aiming mainly at simplicity as a first approach, a surrogate formed by 80% of n-dodecane and 20% of iso-octane was selected. Table 1.2 summarizes the main properties of interest of the two components, the Jet A-1 and the 50% mixture in volume (50% v/v) between the Jet A-1 and the HEFA surrogate.

Inspecting Table 1.2, we observe that the properties of the Jet A-1 fuel and of the 50% HEFA surrogate / Jet A-1 mixture are quite similar. Although the density is somewhat lower, this could be an advantage for pumps and metering systems in the aircraft engines. The volumetric energy content of the HEFA surrogate mixture is a little bit lower, which could be considered a drawback. At the same time, the *H/C* ratio is higher which is an indication of a cleaner combustion in the jet engine. Regarding chemical kinetics modeling, the choice of i-octane and n-dodecane as the HEFA surrogate components will facilitate future works. The chemical kinetics of these chemical species has been developed and analyzed in detail in many works, e.g., (Curran et al., 1998; Davis & Law, 1998; Kumar & Sung, 2010; Westbrook, Pitz, Herbinet, Curran, & Silke, 2009).

Figure 1.4– Some feedstocks for biokerosene production, common in Brazil. There are also shown, the suggested region for occurrence of the feedstocks. Adapted from (Bergmann et al., 2013).

Table 1.2–Main physic-chemical characteristics of the tested jet fuels and components characteristics of the tested QAV1 sample.

	i-octane	n-dodecane	Jet A-1	50% v/v Jet A-1 + HEFA Surrogate
Density@20ºC, kg/m³	703	749	815.1	777.45
Molar mass, g/mol	114.23	170.34	160	157.91
Mean composition formula	C_8H_{18}	$C_{12}H_{26}$	$C_{11.53}H_{21.70}$	$C_{11.26}H_{22.79}$
Carbon number	8	12	11.53	11.26
Hydrogen number	18	26	21.7	22.79
H/C ratio	2.25	2.17	1.88	2.02
Gravimetric LHV, MJ/kg	44.3	44.45	43.2	43.78
Volumetric LHV, MJ/l	31.14	33.29	35.21	34.035
Mixture volume fraction	0.1	0.4	0.5	1
Mixture mass fraction	0.08911	0.3860	0.5248	1

The selected mixture, as well as the pure components, were subjected to a series of experiments in order to determine a set of basic combustion

characteristics of importance to gas turbines. The main advantage of this method is to allow the evaluation of different characteristics of the combustion system isolated from other parameters that could eventually interfere with and bias the results. The jet engine is expected to provide an effective, efficient, reliable, safe and comfortable performance, which strongly depends on good combustion of the jet fuel mixture. Thus, the mixtures with HEFA must present reasonable performance when submitted to the typical combustion conditions in the jet engine combustion chamber in order to be effective as aviation fuel.

The experiments and conditions were selected to simulate the sequence of gas-phase combustion events. After atomization and vaporization of fuel droplets, thermal ignition is the first gas phase phenomenon. The ignition behavior was studied using the ignition delay time measured in a rapid compression machine. Low temperature ignition is especially relevant due to the needs of relight. Also, ignition delay time is an important target for the development of chemical kinetics mechanisms. Flame propagation is the next phenomena, both laminar and turbulent. The study of burning rate is important to predict the fuels mass conversion in premixed regions. It is also used to assess the propensity for lean blow-off. The laminar flame speed is also an important target for the development of detailed chemical kinetics mechanisms. A FORTRAN code was developed to analyze the pressure profile obtained in the constant volume reactor. Then, the lean laminar flammability limit was measured and the turbulent flame extinction was discussed, based on results obtained using additional hydrocarbon reference fuels. The results collected from these experiments were then analyzed to assess in what extent the blending of the HEFA surrogate with the Jet A-1 fuel is beneficial for the performance of the modern jet engines. This aspect was discussed and the conclusion of this work revisited this fundamental question. Figure 1.5 presents a diagram of the aspects covered in this work.

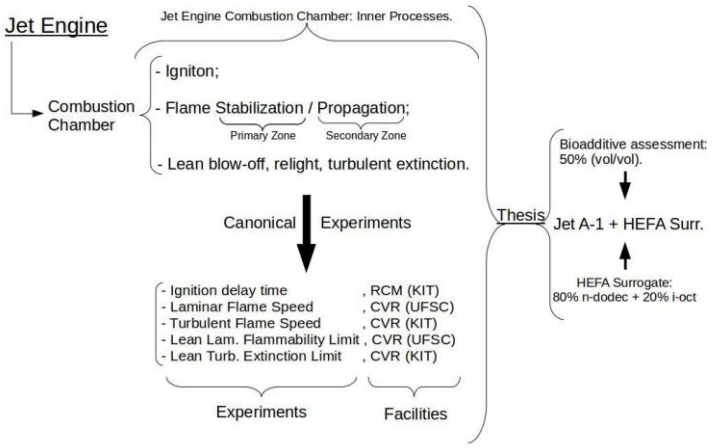

Figure 1.5– Thesis overview: materials and methods.

This thesis is organized as follows. Chapter 2 presents the review of the literature. Section 2.1 presents an overall review of the basic processes involved in the combustion in gas turbines. Section 2.3 reviews the formulation of the Jet fuels and bio-candidates. Chapter 3 presents a review of ignition, flammability limits, flame propagation and flame extinction. Chapter 4 presents the experimental facilities and methods. Section 4.4 presents the model to calculation of burning rates and describes the FORTRAN code used in the calculations. Chapter 5 presents the experimental results: Section 5.1 presents the results of ignition delay times obtained using a rapid compression machine – RCM, section 5.2 presents the results of the laminar flame speed and additional flame/burning characteristics using a constant volume reactor – CVR, post processed using the CVR Flame Code, Section 5.3 presents the results of the turbulent flame speed using a turbulent constant volume reactor – CVR, post processed using the same CVR Flame Code, Section 5.4 presents the results of the laminar flammability limits measured using the CVR, post processed using a Matlab code, adapted from the literature. Section 5.5189 presents the results of the turbulent lean extinguishment. The work ends with concluding remarks applied to the jet engine combustion and suggestion for future work in Chapter 6.

2 LITERATURE REVIEW

The actual jet engines operate as Brayton cycle machines. The main focus of this work is the combustion chamber of a representative jet engine of the actual commercial aviation fleet. Thus the thermodynamic aspects of the Brayton cycle, the compression and expansion phases, are not the scope of the work. The jet engine combustion chamber of interest is described in the following section.

2.1 Jet Engine Combustion Chamber

Figure 2.1 shows a modern jet engine combustion chamber. It is possible to identify three regions: the primary zone, the secondary zone and the dilution zone.

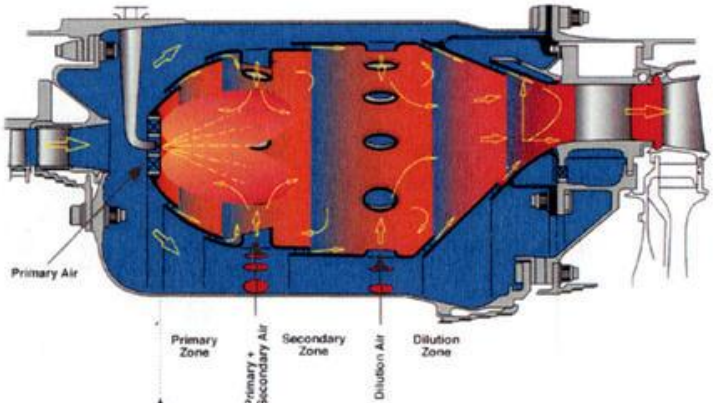

Figure 2.1– Modern jet engine combustion chamber description. Adapted from (Bauer, 2013).

The main goal of a combustion chamber is to achieve total conversion of the air/fuel mixture. The conversion rate of the fuel is proportional to the burning velocity. In the outlet of a typical compressor, the mean flow velocity is about 100 m/s. The estimated turbulent burning velocity of hydrocarbons fuels at the combustion chamber conditions is about 1 m/s (Bauer, 2013), making flame stabilization very hard to achieve. One of the adopted strategies is to use a divergent nozzle geometry in the primary zone of the combustion chamber, where the flow velocity is then reduced to about 20 – 30 m/s. But yet, the flow velocity is much higher than the burning velocity. Additional flame stabilization

strategies are needed. One of these strategies is to inject the fuel with tangential swirl, inducing turbulence, improving molecular mixture with the air and recirculating the flow within the primary zone. In order to improve the recirculating flow pattern, additional air is admitted through the combustion chamber walls, or liner (Boyce, 2002). The liner is perforated with several holes, known as dilution holes. The typical division of the air flow from the compressor is (Bauer, 2013):

- Cooling flow outside the liner: approximately 40 – 50%;
- Primary air (fuel nozzle / heat shield): approximately 15 – 20%;
- Primary air through 1st row: approximately 10 – 15%;
- Secondary air, 2nd row: approximately 10 – 20%;
- Dilution air, 3rd row: approximately 0 – 10%.

As a result, the equivalence ratio in the primary zone is normally rich for conditions far from the idle engine operation, such as takeoff, taxing, landing, and cruse flight. The complete oxidation of the fuel normally occurs at the end of the secondary zone, but it could also occur in the dilution zone, depending on the engine load and other parameters. Some chemical reactions could even occur after the outlet of the combustion chamber, increasing the temperature and damaging the turbine blades and guide vanes. One additional function of the split configuration is to lower the combustion chamber inner temperature, protecting the liner from thermal stress. Furthermore, the addition of air in the dilution zone lowers even more the temperature and is intended to promote a homogeneous radial temperature distribution at the combustion chamber outlet, in order to protect the turbine components (Bauer, 2013).

2.2 Conditions at Combustion Chamber

The extreme conditions in the jet engine combustion chambers pose continuous challenges to the engineers. The injection of the jet fuel through nozzles occurs into a flow field under a high degree of recirculation and swirl. The strain rates are high and the flow is turbulent. Considering a typical machine, the temperature of the compressed air in the combustion chamber inlet is about 750 K and the pressure about 16 bar (Bauer, 2014). Considering another extreme example, the conditions of the Rolls Royce Trent 900, used in the aircraft Airbus A380, the compressed air flow temperature is about 945

K and the pressure is about 45 bar (Bauer, 2013). The equivalence ratio in the region is rich.
After a successful ignition event and with a well-established flame in the primary zone of the combustion chamber, the temperature strongly increases, reaching about 2,000 K (Bauer, 2014). At 2,000 K, considering a typical jet fuel kerosene, some portions of the combustion chamber at some particular operational conditions can experience flame extinction with a subsequent temperature decrease. When the combustion is extinguished inside the combustion chamber, a successful new ignition event must be quickly accomplished, in a process known as relight.
Considering all the efforts to achieve an effective fuel conversion in the modern jet engine combustion chamber, the compressed air split strategy is fundamental to accomplish the combustion chamber key goals. The reliable operation of the jet engine and consequent safety and comfortable flight for the passengers in the aircraft depend on it. The joint operation of a well-designed jet machine with a good quality jet fuel is imperative in this process. Therefore, the behavior in terms of ignition, flammability, burning velocity and extinction of the fuel mixtures inside of the jet engine combustion chamber must be known in order to assess the jet fuel performance. The next section presents the physicochemical and energetic properties of the current and potential candidates for jet fuels.

2.3 Aviations Fuels

The first successful jet-powered aircraft, invented by the German engineer Hans Von Ohain, was flown in 1939. Von Ohain chose gasoline as the fuel because `it was available at the time' and was the fuel employed in all piston engine aircraft. Two years later, Sir Frank Whittle used `illuminating kerosene' as the fuel of his turbojet also because it was available (Maurice, Lander, Edwards, & Harrison, 2001). In fact turbojet engines proved more tolerant in terms of fuel properties than piston engines and these properties were dictated by fuel system limitations, operation requirements and, ultimately, by refining industry's capabilities.
According to (Maurice et al., 2001) AVGas – aviation gasoline, gasoline and the main refinery products at the time, were almost immediately recognized as far from ideal jet fuels since their high volatility would produce engine malfunction at altitude due to `vapor lock'. The lighter components in gasoline had poor lubricity thus wearing the metering

pumps whilst the octane enhancing additives, which contained lead, result in erosion in the hot turbine blades.

On the other hand, the middle distillate fraction of petroleum had little value or use for the refiners and presented some interesting characteristics, like higher volumetric heating values and higher hydrogen content thus producing less soot. This combination of factors would lead to the production of jet fuels, but only after the industry decided that the jet engine `had a future', since there were rumors that it was uncontrollable at higher speeds and certainly did not seem to have any future in commercial aviation.

The first fuel for aviation gas turbines was specified by the US Army Air Corps in 1944 and identified as Jet Propellant #1 or JP-1. It had a distillation range roughly between 149 - 260ºC and a freezing point below -60ºC, the latter requirement being especially difficult to attain by most refiners. Even with this setback, the JP-1 specification took the first step, clearly moving jet fuels from avgas towards the kerosene range. Other early fuel specifications, like JP-2 and JP-3, included a viscosity limit below 1 cSt at 38ºC, thus establishing the jet fuels as blends of gasoline and kerosene fractions. In 1951, four years after the creation of the US Air Force - USAF, the JP-4 fuel specification was issued as a result of a collective effort of USAF specialists and fuel suppliers, defining fuel specification based on general characteristics of available crude oil and the recognition that many fuel properties are interdependent.

As its predecessor, the JP-4 was a mixture of gasoline and kerosene fractions of crude oil but with strong vapor pressure restrictions to reduce boil-off losses, with reduced attention to viscosity since atomizers had been developed for thicker fuels like diesel. Jet fuels were then produced almost exclusively from straight distillation of suitable light crude oil, being a readily available product without major alternative use. The lowest boiling fraction of this fuel contained normal paraffins (straight chain alkanes) that had been removed from regular gasoline because their low octane ratings. The boiling range of JP-4 was 66 – 149ºC, which the US Navy considered too dangerous to store in its aircraft carriers, so the US Navy adopted only the kerosene fraction of JP-4, that presents a 182-260ºC distillation range, a flashpoint above 60ºC and freezing point specification below -40ºC. This fuel was designated JP-5 and was suitable for the lower altitude operation of the US Navy aircraft, even though its reduced volatility demanded the use of higher energy ignitors.

Thus, within a decade the definition of jet fuel requirements had

matured to a standard close to other liquid fuels but its ability to provide cooling to the engine lubricant, was still very limited. Problems with fuel `coking' occurred in fuel injectors and manifolds, albeit the quality control tests presented no indication of excessive deposition in conventional, gasoline-derived gum tests. The phenomenon of coking would be later defined as thermal oxidative stability resulting of a series of liquid oxidation reactions with minor components, like heterocompounds, with oxygen dissolved in the fuel. In the late 1950's a flow device was developed to evaluate more realistically the high temperature performance of jet fuels and the success of such effort reinforced the use of jet propulsion.

In the 1960's the availability of feedstock became a concern. Jet fuels were produced primarily from light, low sulfur crude oil, with little or no processing besides atmospheric distillation thus keeping the prices low. Then, increasing demands for imported light Arabian crudes were reducing the offer and the feedstock was being replaced with heavier crude, high in sulfur and difficult to refine into the existing product slate. At the same time, commercial aviation began its expansion into the jet age and a kerosene fuel designated as Jet A by ASTM was the baseline fuel for commercial aircraft. Considering passenger safety Jet A was defined as a pure kerosene fuel, similar to JP-1, with a flashpoint above 38ºC and freezing point below -40ºC, and -47ºC for international Jet A-1.

These specifications endured mostly unaltered since then, except for sulfur content limits. New policies demanded a decreasing in sulfur content aiming to reduce environmental impact but this also affects the fuel's lubricity, since the phenomenon of boundary lubrication (lubrication provided by metal-adhering films) is attributed to trace amounts of sulfur-, nitrogen- and oxygen-containing compounds. Such problem is amended with the use of additives.

It is important to notice that fuel specifications were developed considering crude oil as the only practical feedstock thus implying the presence of different classes of hydrocarbons in the fuel. In the current and future scenarios, with the development of alternative feedstocks and processes, the most likely near-term solution to meet regulations involves the blending of alternative components into conventional fuel, following the path established during the 1990's with the development of Sasol's synthetic paraffinic kerosene. More details about this alternative fuel will be presented later on.

The following section presents the properties for current Jet fuels, the different classes of species in its formulation, and the prospects for bio-

fuels.

2.4 Jet Fuel Specifications

The main properties of commercial jet fuels are presented in Table 2.1. As one would expect, these fuel properties are 'operational' requirements related to the intended application. The real Jet A and Jet A-1 greatly varies in composition, e.g. typical aromatic content between 8 and 22%, as a result of different quality of crude oil and refiner capability. As pointed out previously fuel specifications are `biased' since they include implicit assumptions that are met when petroleum is the feedstock, like smooth boiling range distribution and the absence of a specified minimum aromatic content.

Table 2.1– Main properties of commercial jet fuels. Adapted from (Bacha et al., 2006).

	Jet A	Jet A-1
Standard	ASTM D 1655	DEF STAN 91-91
Acidity, mg KOH / g	0.10	0.015
Aromatics, % vol max	25	25
Sulfur, % mass	0.30	0.30
Distillation, ºC, 10% recovered, max	205	205
Distillation, ºC, end point	300	300
Flash point, ºC, min	38	38
Density, 15ºC, kg/m³	775-840	775-840
Freezing point, ºC, max	-40	-47
Viscosity, -20ºC, mm²/s, max	8.0	8.0
Net heat of combustion, MJ/kg, min	42.8	42.8
Smoke point, mm, min	18.0	19.0
Naphthalenes, % vol, max	3.0	3.0
Filter pressure drop, mm Hg, max	25	25
Existent gum, mg/100 ml, max	7	7

Table 2.2, reported by (Edwards et al., 2007), presents two average compositions of jet fuels. The World Survey Average is the average composition of 55 jet fuel samples (Jet A, Jet A-1, JP-8 and JP-5)

collected from locations worldwide while the Composite Jet A (POSF 4658) is an average fuel obtained by mixing equal volumes of Jet A from five different US refiners.

Table 2.2– Average compositions of jet fuels. Adapted from(Edwards et al., 2007).

Compound	World Survey Average	Composite Jet A
paraffins, normal and iso	58.78	55.2
monocycloparaffins	10.89	17.2
Dicycloparaffins	9.25	7.8
Tricycloparaffins	1.08	0.6
Alkyl benzenes	13.36	12.7
Indalenes + tetralins	4.9	4.9
Naphthalene	0.13	< 0.2
Substituted naphthalenes	1.55	1.3

When studying such a complex mixture of hydrocarbons, one must have in mind the characteristics and roles of different classes of compounds regarding combustion behavior, storage and thermal stability, engine performance and emissions, lubricity and others. These issues will be discussed in the following subsections.

2.5 Jet Fuel Composition and Properties

As presented in Table 2.2, jet fuel is a mixture of many different hydrocarbons, separated from crude oil by distillation. By this process it is possible to assure that a kerosene fuel has carbon number distribution between 8 and 16 carbons, while for a 'wide-cut' jet fuel this distribution is about 5 and 15 carbons.

Most of the hydrocarbons in jet fuels are members of paraffinic, naphthenic (cycloalkane) or aromatic classes and it is important to know how some physical and chemical properties varies, for hydrocarbons within the C_8-C_{16} range, as a function of the class. The following table presents data of boiling and freezing points of some representative

hydrocarbons grouped by carbon number.

Table 2.3 – Boiling and freezing points of some representative hydrocarbons grouped by carbon number. Adapted from (Bacha et al., 2006).

Compound	Formula	Class	B.P. ºC	F.P. ºC
N-octane	C8H18	n-paraffin	125.7	-56.8
2-methylheptane	C8H18	i-paraffin	117.6	-109.0
1-methyl-1-ethylcyclopentane	C8H16	naphthene	121.5	-143.8
Ethylcyclohexane	C8H16	naphthene	131.8	-111.3
o-xylene	C8H10	aromatic	144.4	-25.2
p-xylene	C8H10	aromatic	138.4	13.3
cis-decalin	C10H18	naphthene	195.8	-43
tetralin	C10H12	aromatic	207.6	-35.8
naphthalene	C10H8	aromatic	217.9	80.3
n-dodecane	C12H26	n-paraffin	216.3	-9.6
2-methylundecane	C12H26	i-paraffin	210.0	-46.8
1-ethylnaphthalene	C12H12	aromatic	258.3	-13.8
n-hexylbenzene	C12H18	aromatic	226.1	-61.0
n-hexadecane	C16H34	n-paraffin	286.9	18.2
2-methylpentadecane	C16H34	i-paraffin	281.6	-7.0
n-decylbenzene	C16H26	aromatic	297.9	-14.4

From the Table 2.3 it is possible to notice an increase in boiling point for larger hydrocarbons, thus compounds of the middle kerosene range with boiling point around 220ºC probably are C_{10} aromatics, C_{11} naphthenes and C_{12} paraffins, with somewhat 5ºC variation occurring between linear and branched alkanes of the same carbon number. The freezing point also increases with carbon number within each class but is strongly influenced by molecular shape. Normal paraffins and unsubstituted aromatics crystallize at much higher temperatures than

other compounds with the same carbon number since their geometry allows them to easily pack together into a crystalline structure.
Table 2.4 lists density and energy content of representative jet fuel hydrocarbons. For compounds in the same class, density increases with carbon number, while for compounds with the same carbon number density increases by class in the order paraffin, naphthene and aromatic.

Table 2.4–Density and energy content of representative jet fuel hydrocarbons and freezing points of some representative hydrocarbons grouped by carbon number. Adapted from (Bacha et al., 2006).

Compound	Class	Density at 20ºC, g/cm³	N.E.C at 25ºC, MJ/kg	N.E.C at 25ºC, MJ/l
N-octane	C8 n-paraffin	0.727	44.42	31.21
2-methylheptane	C8 i-paraffin	0.679	44.38	30.97
1methyl-1ethylcyclopentane	C8 naphthene	0.7809	43.57	34.02
Ethylcyclohexane	C8 naphthene	0.7879	43.40	34.20
o-xylene	C8 aromatic	0.8801	40.81	35.92
p-xylene	C8 aromatic	0.8610	40.81	35.14
cis-decalin	C10 naphthene	0.8867	42.62	38.2
tetralin	C10 aromatic	0.9695	40.52	39.06
naphthalene	C10 aromatic	1.1750	40.12	47.14
n-dodecane	C12 n-paraffin	0.7488	44.11	33.03
2-methylundecane	C12 i-paraffin	0.7458	44.08	32.87
n-hexadecane	C16 n-paraffin	0.7735	43.95	33.99
n-decylbenzene	C16 aromatic	0.8554	42.23	36.12

For compounds of the same carbon number, the energy content increases per unit weight by class, from aromatic, to naphthene to paraffin, clearly matching the different hydrogen to carbon ratio of each class. In a volume basis the order is reversed and this becomes evident for fuels, i.e. less dense gasoline has higher energy content on a weight basis whereas denser diesel has higher energy content on a volume basis.
In terms of viscosity carbon number is more important than hydrocarbon class; for a given carbon number, naphthenes generally present higher viscosity than aromatics and paraffins. The following table summarizes

how the contribution of each class affects the overall jet fuel properties in terms of a beneficial effect (denoted by '+'), neutral or minor contribution (denoted by 'o') or a detrimental effect (denoted by '–').

Table 2.5 –Potential contribution of each hydrocarbon class to selected jet fuel properties. Adapted from (Bacha et al., 2006).

Property	n-paraffin	i-paraffin	naphthene	Aromatic
Gravimetric energy content	+	+	o	-
Volumetric energy content	-	-	o	+
Combustion quality	+	+	+	-
Low-temperature fluidity	- -	o/-	+	o/-

As can be seen in Table 2.5 the main benefit provided by aromatics in the fuel is a good volumetric energy content, while the main contribution of naphthenes is the reduction of freezing point hence improving the low-temperature fluidity of the fuel. The table also shows that i-paraffins present intermediate properties between aromatics and n-paraffins thus being interesting as a main component of the fuel mixture. While paraffinic and naphthenic fractions of the jet fuel present largely dispersive intermolecular forces, some aromatic compounds shows polar and hydrogen-bonding character thus increasing the water solubility in the fuel and also causing some types of elastomers used in fuel system to swell, which the industry considers as a safeguard against fuel leaks. This swelling occurs in seals made of nitrile rubber, a copolymer composed of poly(butadiene) and poly(acrylonitrile), the latter presenting a highly polar cyano group on adjacent polymer chains. The net negative charge in the cyano group interact with the electropositive aromatic hydrogens, therefore breaking the polymer-polymer and penetrant-penetrant intermolecular bonds and forming polymer-penetrant intermolecular bonds thus producing the swelling.

It is important to notice that the properties evaluated in Table 2.5 are bulk properties, so their values to a first approximation are close to the weighted averages of the property's values of the individual components. Properties like energy content, distillation range, fluidity and combustion characteristics are bulk ones, while lubricity and stability are related to trace amounts of certain heterocompounds that

may be presented in the base fuel as manufactured or are additives or even contaminants.

Regarding lubricity and stability, these fuel features are affected by the process of hydrotreatment or hydrodesulfurization. According to the DEF STAN 91-91 `mildly' hydrotreated components are those petroleum derived hydrocarbons subjected to hydrogen partial pressures below 70 bar while those submitted to hydrogen partial pressures greater than 70 bar are considered `severely' hydroprocessed. Refiners employ this `upgrading', catalytic process to remove sulfur-containing compounds like mercaptans, thiols, thiophenes and organic sulfides, but HDS also promotes saturation of olefins and, in severe conditions, saturation of aromatic rings and consumption of nearly all sulfur and nitrogen heterocompounds. In the absence of these naturally occurring species the use of additives is necessary.

Additives are fuel soluble chemicals added in small amounts to enhance or maintain properties important to fuel performance and handling. Many additives are derived from petroleum-based raw materials and their concentration is in the parts per million range. The use of additives is the main difference between commercial and military jet fuels. International Jet A-1 contains a static dissipator and eventually an antioxidant while the Jet A usually contains no additives or perhaps an antioxidant. Military fuels demand three or four additives, especially regarding thermal stability since high-performance military aircraft place higher thermal stress on fuel (Bacha et al ., 2006).

Regarding antioxidant additives, its use is required in any fuel or fuel blend that has been hydrotreated under Jet A-1 and US military specifications, being optional in non-hydrotreated fuels under these specifications and for Jet A. Approved antioxidants for jet fuels are sterically hindered phenols like 2,6-ditertiary butyl-4-methyl phenol. The addition of antioxidant must occur immediately after the hydrodesulfurization to avoid any initial oxidative reaction in the following steps of processing and storage.

Other important class of additives are corrosion inhibitors and lubricity improvers, since most of the tanks and pipelines in fuel distribution system are made of uncoated steel. Corrosion inhibitors prevent free water and oxygen from rusting and corroding parts whilst lubricity additives are employed to compensate for the poor lubricity of hydrotreated jet fuels. The latter additives contain a polar group, like a carboxylic acid, that adheres to metal surfaces forming a thin film that improves boundary lubrication.

2.6 Fuel Performance and Emissions

Since the primary function of aviation turbine fuel is to power the aircraft, energy content, combustion quality and emissions are key fuel performance features. Other significant properties are handling-related ones like fluidity, lubricity, and stability. The relationship between energy content and soot propensity is one of the major jet fuel performance features deserving careful assessment.

Energy content of hydrocarbons differ, as pointed out in Table 2.4, in terms of class and hydrogen to carbon ratio, with more paraffinic fuels being lighter, i.e. lower density, thus more energy per mass, whereas more aromatic ones being heavier, i.e. higher density thus more energy by volume. Usually a denser, high volumetric energy content jet fuel is preferred, considering that it is typically bought and sold by volume, unlike some gaseous fuels sold by heating value.

In terms of combustion behavior, however, higher aromatic fraction is related with increasing soot formation which must be minimized for several reasons (Dagaut & Cathonnet, 2006), including radiant heat loss, premature engine fails due to increased combustor liner temperatures and turbine erosion and effects in high altitude atmospheric chemistry. Fuel specifications include three main properties to evaluate fuel's soot tendency: maximum limits for aromatic and naphthalene, i.e. two fused aromatic rings, fractions and smoke point, a measurement of the maximum flame height achieved in a standard wick-fed lamp without smoking. Experimental studies in combustion rigs (Lohmann & Jeroszko, 1983; Rosfjord, 1984) showed that viscosity, surface tension, specific gravity and distillation temperatures also affect soot formation since these properties are related to fuel spray droplet size, hence residence time and rate of vaporization.

Unfortunately changes in fuel may or may not produce interpretable variations in soot production. Fuels with increased aromatic content, from typical 20% up to 52%, thus with correspondent H/C ratio decreasing from 1.89 to 1.59, were prepared for NASA's Broad Specification Fuels Technology Program (Lohmann & Jeroszko, 1983) and presented unexpected lower viscosity and higher volatility characteristics, producing less soot than Jet A. Since the higher aromatic fuels were prepared mixing Jet A with blending stocks and xylene tower bottoms, the authors attributed the unusual result to these 'narrow and unique cuts' of aromatics. On the other hand, if these blends resulted in higher viscosity and lower volatility, thus more soot, it will be difficult to ascertain which factor was predominant: the greater concentration of

carbon and precursors or the degradation in fuel's atomization and distribution that results in fuel-rich regions.

Regarding gaseous emissions, air transportation receives less attention than other sectors since its contribution to global emissions is small compared to ground vehicles and stationary sources like power plants. Some emissions from aircrafts are limited according to the landing and take-off cycle (LTO) defined by the International Civil Aviation Organization (ICAO), that regulates emissions near ground level but indirectly limit them in altitude too.

Carbon dioxide emission in aircraft is a minor concern and its future reduction is linked to engine and airframe improvements as well as the use of biofuels. Water vapor, the other major product of hydrocarbon combustion, forms contrails and aviation-induced cirrus clouds at cruise altitude and their effects on climate change is an area of ongoing research. Sulfur oxides and nitrogen oxides comprise the most hazardous gaseous emissions and their regulation is more stringent. Sulfur oxides are related to trace amounts of sulfur-containing heterocompounds and their presence in the jet fuels depend on the quality of the crude oil feedstock and the level of hydrotreating employed by the refiner. Even though the specifications allow a maximum of 3,000 ppm sulfur the worldwide average appears to be around 500-1,000 ppm (Bacha et al., 2006).

Nitrogen oxides are mostly formed from oxidation of atmospheric nitrogen at very high temperatures in the combustor, with fuel bound nitrogen representing some 2% of NOx total emission. Nitrogen oxides are thought to contribute to the formation of ozone near ground level as well as acid rain. Since NOx formation is controlled by maximum temperature, engine design and operating conditions are key factors to ensure complete, fast and uniform combustion thus lowering this emission. This issue becomes more important when burning fuels with higher aromatic content since there is an increase in flame temperature with reduced H/C ratio (Lohmann & Jeroszko, 1983).

Regarding fuel stability, most of the problems are related to oxygen-containing compounds, like peroxides and hydroperoxides that remain dissolved in the fuel and may attack fuel system elastomers. Additional reactions may result in the formation of insoluble particulates and soluble gums that deposit on surfaces and induces filter and small orifices' clogging. The thermal stability of a jet fuel is of critical importance since the fuel acts as heat exchange medium in many engine and airframe subsystems like hydraulic fluid and air conditioning equipment. The resulting heating of the fuel accelerates the formation of

particulates and gums in liquid phase. While the storage stability can be improved with antioxidant additives they are not usually effective in improving thermal stability.

The jet fuel is also expected to lubricate some moving parts in fuel pumps and fuel metering units. The lubrication mechanism is a combination of hydrodynamic lubrication and boundary lubrication. The former is the result of a layer of viscous liquid preventing opposing moving surfaces from contacting each other thus higher viscosity fuels, i.e. those presenting higher naphthenic fraction, provide better lubrication than lower viscosity ones. When the tolerances between surfaces are narrow, the boundary lubrication becomes important.

As noted previously, the boundary lubrication is associated with the presence of trace amounts, ca. 10 ppm, of heterocompounds containing oxygen, nitrogen or sulfur. The naturally occurring compounds that provide jet fuel with its intrinsic lubricity can be removed by hydrotreating, the refining process employed to reduce sulfur and aromatic content. Nevertheless, low sulfur or aromatics level are not necessarily indicatives of inadequate lubricity since the boundary lubricity cannot be predicted from bulk physical or chemical properties but it can only be measured in a designed test apparatus known as Ball-on-Cylinder Lubricity Evaluator (BOCLE).

Another fuel property that plays an important role is its `fluidity', the combination of viscosity and freezing point. Jet fuel specifications place an upper limit in viscosity to prevent excessive pressure drop in the fuel system and specially to assure the formation of a fine spray of droplets that evaporate quickly as they mix with air. More viscous fuels are also more difficult to relight in flight. Regarding freezing point, it is important to note that, being a mixture of hundreds of different compounds the jet fuel does not solidify at one temperature like pure substances. As the fuel is cooled, the hydrocarbons with highest freezing points solidify first, forming wax crystals. The freezing point of the jet fuel is defined as the temperature at which the last wax crystal melts. The presence of wax crystals affects fuel `pumpability' and the freezing point is an indicator of this low temperature characteristic. Typically a jet fuel remains pumpable some 4-15ºC below its freezing point, thus making the fuel freezing a concern only in special cases like polar route flights during the winter.

Also related to the fuel handling system is fuel's volatility, characterized by vapor pressure and distillation curve. A volatile fuel is one that has higher vapor pressure and lower initial distillation temperature. However, a too volatile fuel may cause vapor lock in the fuel system as

well as evaporative losses. This fuel property was the major problem in early fuel formulations and to this day there is still a double standard: the widely used Jet A/A-1, a kerosene-type, relatively non-volatile fuel, and Jet B, a wide-cut fuel, better suited for cold weather applications because it has lower viscosity and freezing point and it is used when evaporative losses are less of a concern.

Taken together, these findings indicate how complex it is to attain desired properties and performance with acceptable emissions in a fuel obtained as `straight run' as possible. Studies like those of (Rosfjord, 1984) demonstrate the nontrivial relationship between different compounds of the same hydrocarbon class and their effects on several fuel properties like ignition and soot propensity. A compromise between sophisticated combustion control, increased maintenance cost and broad specification fuels is the most likely middle to long term scenario. Moving on, alternative fuels will be discussed in the ensuing section.

2.7 Alternative Fuels

Petroleum products have always been the preferred transportation fuels since they offer an optimal combination of availability, ease of handling, energy content, performance and, most of all, price. However, since the 1973 oil embargo, concerns about energy security and continued availability prompted government and industry to look at alternative sources.

In the case of aviation fuels the search for an alternative fuel is more complex for several reasons: (i) any alternative fuel must be compatible with conventional fuel so it can be transported and stored within the existing infrastructure, i.e. drop in fuel; (ii) airlines keep their aircrafts in service for around forty years (Blakey, Rye, & Wilson, 2011). So, the alternative fuel must provide safe and reliable operation of engines and airframes with minimal increase in maintenance.

Another major issue is related to the energy content of the alternative fuel. First generation biofuels like alcohols and esters, already adopted in fuel blends for land transportation, contain oxygen which gives no contribution to the fuel's heating value. Table 2.6 presents a comparison of these energy ratings for conventional and alternative fuels.

Table 2.6–Density, gravimetric energy and volumetric energy of selected fuels. Adapted from (Bacha et al., 2006) and (Corporan et al., 2011).

Fuel	Density	Gravimetric	Volumetric

	at 15ºC, kg/l	Energy, MJ/kg	Energy, MJ/l
Jet A/A-1	0.808	43.2	34.9
Methanol	0.796	19.9	15.9
Ethanol	0.794	27.2	21.6
Biodiesel	0.870	38.9	33.9
Fischer-Tropsch Synfuel	0.759	44.2	33.6
Camelina HEFA	0.751	44.1	33.1
Beef tallow HEFA	0.758	44.1	33.4

As it can be seen in Table 2.6, Fischer-Tropsch - FT and `hydroprocessed esters and fatty acids' - HEFA fuels are the alternatives that more closely reproduce gravimetric or volumetric energy content of conventional fuel. These similarities are not enough to immediately establish them as potential near or mid-term alternative fuels since experimental work (Corporan et al., 2011) revealed that alternative paraffinic fuels produced via FT or hydroprocessing of several feedstocks like beef tallow, yellow and brown grease and camelina oil, present inferior lubricity, lesser seal swelling and low density, which impacts aircraft range.
The following subsections will discuss production, composition, properties and the tests carried out so far with some alternative fuel ,components.

2.7.1 Fischer-Tropsch Synthetic Fuels

The Fischer-Tropsch process was first developed by the German chemists Franz Fischer and Hans Tropsch in 1925. The FT process starts with the partial oxidation of the feedstock, usually coal or methane, in the presence of steam, oxygen and a catalyst to produce `syngas', a mixture of carbon monoxide and hydrogen. Methane is the preferred carbon source since its capital cost is around 30% lower and also because in coal gasification the unwanted CO_2 formation is typically close to 50% while in methane reforming this yield is about 20%.
The obtained syngas is then converted into paraffinic hydrocarbons employing iron or cobalt-based catalysts (Dry, 2002). Today two main FT operating modes are used: a high temperature (300-350ºC) process with iron-based catalysts for the production of gasoline and linear, low molecular mass olefins; and a low temperature (200-240ºC) process using either iron or cobalt catalysts to obtain high molecular linear

waxes. The general reaction describing Fischer-Tropsch synthesis is,

$$CO + H_2 \rightarrow (CH_2)n + H_2O, \quad (2.1)$$

which occurs in a catalytic site and mostly produces straight chain alkanes, according to the Anderson-Schulz-Flory polymerization model (Huber, Iborra, & Corma, 2006). At each stage of growth, the adsorbed hydrocarbon may suffer: (i) hydrogenation followed by desorption thus forming primary FT products; (ii) addition of another CH_2 monomer to continue chain growth; (iii) desorption.

It must be stressed that many detailed mechanisms have been proposed to describe the FT synthesis but the matter remains controversial. Since FT always produces a wide range and amount of olefins, paraffins and oxygenates like ketones, alcohols and aldehydes, these appear to be primary products, even though that, at the hydrogen's partial pressure, virtually all olefins should be hydrogenated to paraffins (Dry, 2002). Another important question is the process' selectivity, influenced by temperature, pressure, syngas H2/CO ratio, catalyst type and promoters.

According to (Dry, 2002), a FT plant employing iron catalysts and operating at 340ºC is able to produce 40% straight run, low octane and low aromatic gasoline, with additional 20% yield of propene and butene that can be oligomerised to produce highly branched, high octane gasoline. However the straight run gasoline demands hydrogenation of its C5-C6 cut, while the C7-C10 fraction needs severe reforming with platinum catalysts to enhance octane rating, making FT gasoline production less attractive than the diesel option.

The high linearity and low aromatic content that hamper the production of FT gasoline are very positive for producing high cetane diesel fuel. Using low temperature process and cobalt catalysts to enhance wax production, 20% straight run diesel is produced with a post-hydrotreatment cetane number of 75. Heavier than diesel products account for nearly 50% yield and, after a mild hydrocracking, a high quality, aromatic free diesel is obtained.

South African company Sasol pioneered the development of a synthetic FT jet fuel, when its iso-paraffinic kerosene-IPK was included in the DEF STAN 91-91 Issue 3 (1999) as a 50% by volume component for Jet A-1. According to (Corporan et al., 2011) this coal-to-liquid - CtL kerosene is produced via oligomerization of C3 and C4 olefins, followed by hydrotreating and fractionation, producing a fuel with very high degree of branching. The composition of the Sasol IPK is around 85%

of C_{10}-C_{14} iso-paraffins, 11% of C_{10}-C_{13} naphthenes and 4% of C_{10}-C_{12} n-paraffins (Blakey et al., 2011). In 2008, the Issue 6 of DEF STAN 91-91 was published with the certification of a fully synthetic jet fuel also developed by Sasol and, until 2009, Sasol IPK remained the only alternative to Jet A-1 in commercial use, fueling most of the aircraft leaving O.R. Tambo International Airport in Johannesburg.

Since then, Shell, Syntroleum and Rentech also developed FT kerosene fuels but using gas-to-liquid GtL processes, a pathway adopted by Sasol in its Oryx plant in Qatar. These GtL kerosenes do not present a naphthenic fraction, with Shell's fuel being close to a 75/25 blend of C_8-C_{12} branched and linear paraffins whilst Syntroleum and Rentech ones are 78 iso-/22 n- mixtures of C_8-C_{16} paraffins.

Even with the certification of Sasol's IPK, a test programme called Aircraft Alternative Fuel Emissions eXperiment – AAFEX (Anderson et al., 2011) was conducted by NASA in 2009 to evaluate gaseous and particulate emissions of standard JP-8, Shell GtL, Sasol CtL and 50/50 blends of each FT fuel with JP-8. The measurements were carried out in two CFM56-2C1 engines of a parked McDonnell Douglas DC-8 owned by NASA's Dryden Flight Research Center (now Neil A. Armstrong Flight Research Center). In the study was observed that burning FT fuel did not affect engine performance thus not offering advantage or penalty in terms of fuel economy. However the alternative fuels exhibited higher combustion efficiencies at low power settings, therefore indicating a general trend of being less polluting. When the 50/50 blends were burned, no significant reduction in certification gas emissions was obtained, pointing out a clearly relationship between aromatic content and emissions.

The test also showed that the aromatic-free FT fuels caused fuel-system seals to shrink, resulting in fuel leaks in the aircraft tank and in the tanker trucks used to store and deliver them. The leaks went away with the addition of JP-8, which presents an intrinsic aromatic fraction. This result is accordance with previous studies (Corporan et al., 2007; DeWitt, Corporan, Graham, & Minus, 2008; Graham, Striebich, Myers, Minus, & Harrison, 2006) where Syntroleum's GtL fuel and different aromatic solvents were tested regarding material compatibility with nitrile rubber. Other tests of engine performance were conducted by the US Air Force to study Syntroleum and Shell GtL fuels, and their blends with JP-8, in several transport and fighter platforms (Blakey et al., 2011) with only beneficial impacts being observed with the use of these FT blends.

Considering the several tests reported above, it is safe to assert that

alternative FT fuels are suitable as `drop-in' replacements for conventional Jet A/A-1, once they are corrected for density and heating value, i.e. present a minimum aromatic content that also prevents fuel leaks.

2.7.2 Biofuels

Biofuels, as the name implies, are fuels derived from living organisms such as microalgae, plants and animals. Different components in the biomass can be converted in liquid fuels: starch and sugar are converted in alcohol by fermentation; edible and nonedible oils and fats are used to produce fatty acid esters and hydrotreated oils; and new processes for the conversion of lignocellulose are emerging. Although these sources present great energy potential many problems regarding their production and quality remain unsolved.

As pointed out previously, the adoption of alcoholic biofuels in aviation is unlikely considering their low gravimetric energy content, see Table 2.6. Thus the remaining biofuels to be considered are fatty acid esters (FAE) and hydrotreated oils. Fatty acid esters, also commonly referred to as biodiesels, are long chain groups derived from transesterification of triglyceride fats in the feedstock, usually a vegetable oil. The transesterification is the most common way of upgrading vegetable oils (Huber et al., 2006) to avert their intrinsic disadvantages like high viscosity, low volatility and coking propensity. Figure 2.2 presents a generic transesterification reaction with ethanol.

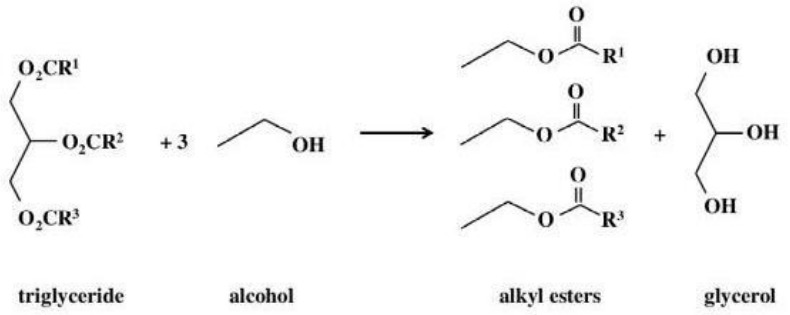

Figure 2.2– Generic transesterefication reaction. Adapted from (Huber et al., 2006).

Figure 2.2 does not show the presence of a catalyst in the reaction but most of the industrial biodiesel plants conduct the transesterification

with alkali catalysts, usually sodium methoxide (Huber et al., 2006), since the uncatalysed reaction only occurs at elevated pressure and temperature, i.e. 120 atm and 350ºC, thus being very energy intensive. There is much ongoing research to develop new catalysts, especially heterogeneous ones that can be easily removed from the product and recycled.

The composition of the alkyl groups, denoted by `R', in the resulting esters varies according to each different feedstock in terms of number of carbons and presence of carbon-carbon double bonds i.e. unsaturation. Table 2.7 shows the chemical composition of fatty acids present in several oil crops.

From the data in Table 2.7 one can see some of the reasons why vegetable-derived fuels demand further processing to be compatible with conventional jet fuel. Babassu, coconut, palm and olive oils are the only feedstocks that provide significant amounts of fatty acids with carbon chains similar to kerosene, i.e. up to 15 carbons. Most of the vegetable oils are primarily composed by carbon chains with 16 or 18 carbons, much of the latter presenting unsaturations, therefore the preference of using them to obtain biodiesel. Also noteworthy is the rapeseed oil composition, strongly concentrated on long chains with one unsaturation.

Table 2.7– Chemical composition of fatty acids in biodiesel feedstocks. Adapted from (Huber et al., 2006).

	Fatty acid composition, % weighted number of C : C=C bonds									
Oil or fat	8:0	10:0	12:0	14:0	16:0	18:0	18:1	18:2	18:3	22:1
Babassu	2.6-7.3	1.2-7.6	40.0-45.0	11.0-27.0	5.2-11.0	1.8-7.4	9.0-20.0	1.4-6.6		
Camelina					0.0-6.4	0.0-2.8	14.1-19.5	18.8-24.0	27.0-34.7	0.0-4.0
Canola					1.2-6.0	1.0-2.5	52.0-66.9	16.1-31.0	6.4-14.1	0.0-4.0
Coconut	4.6-9.5	4.5-9.7	44.0-51.0	13.0-20.6	7.5-10.5	1.0-3.5	5.0-8.2	1.0-2.6	0.0-0.2	
Corn				0.0-0.3	7.0-16.5	1.0-3.3	20.0-43.0	39.0-62.5	0.5-13.5	
Cotton-seed				0.6-1.5	21.4-26.4	2.1-5.0	14.7-21.7	46.7-58.2		
Jatropha					12.1-17.0	2.9-9.7	34.0-50.1	29.1-41.6		
Olive	0.0-1.3	7.0-20.0	0.5-5.0	55.0-84.5	3.5-21.0					

Palm	0.0-0.4	0.5-2.4	32.0-47.5	3.5-6.3	36.0-53.0	6.0-12.0				
Peanut				0.0-0.5	6.0-14.0	1.9-6.0	36.4-67.1	13.0-43.0		0.0-0.3
Rapeseed				0.0-1.5	1.0-6.0	0.5-3.5	8.0-60.0	9.5-23.0	1.0-13.0	5.0-56.0
Soybean					2.3-13.3	2.4-6.0	17.7-30.8	49.0-57.1	2.0-10.5	0.0-0.3
Sunflower					3.5-7.6	1.3-6.5	14.0-43.0	44.0-74.0		
Tallow(beef)				2.1-6.9	25.0-37.0	9.5-34.2	14.0-50.0	26.0-50.0		

A process like pyrolysis or zeolite upgrading, that could be employed before or after the transesterification, can eliminate the ester group as CO_2 and also promote the cleavage of the long alkyl chain to form smaller paraffins, olefins, naphthenes and aromatics by Diels-Alder reaction (Huber et al., 2006). Though technically possible, the transesterification followed by an upgrading would hardly be commercially viable.

Regarding test programs and flight demonstrations, (Blakey et al., 2011) reports several such initiatives, conducted by airlines, manufacturers and the military during the 2007-2010 span and it is remarkable that the use of FAEs was restricted to a single test by Virgin Atlantic. In February 23rd 2008, during a 45-minute flight between London and Amsterdam, one of the four GE CF6-80C engines of a Boeing 747-400 was fueled with a blend of 80% Jet A-1 and 20% fatty acid methyl ester from coconut and babassu palm oil. Regardless the successful demonstration, Boeing issued a disclaimer stating that the FAME used was the only suitable fuel available at the time and that it did not consider FAEs a viable option for aviation.

After this flight and following the introduction of biodiesel as a blend in conventional diesel for road transport in England, a problem with FAE contamination of jet fuel ensued due to the concurrent transport infrastructure. Since there is a carry through of contaminants, such as metals, from the raw oil into the FAE, the presence of typical contaminants of biodiesel, like zinc, nickel and vanadium, in jet fuel could cause severe damage to the hot end materials in the turbine. According to (Blakey et al., 2011), a contamination of 30 ppm of FAE in jet fuel is already accepted and the industry is working towards a 100 ppm limit.

The remaining type of biofuel is upgraded oil by hidrotreatment. The triglycerides present in oils and fats can be hydrotreated in a way similar to the latter stages of conventional refinery and Fischer-Tropsch processes thus promoting deoxygenation, saturation, hydrocracking and isomerization of the alkyl chains. Many different sources of triglycerides could be harnessed this way, like algae, animal fats, brown and yellow grease, camelina and jatropha. These two plants, camelina and jatropha, play an important role in the near to mid-term development of these HEFA fuels in the USA market, since camelina is an oil crop well established in some US states for its use in biodiesel production, while jatropha is able to grow under drought conditions and in sandy soils that are otherwise unused for farming, therefore presenting strong sustainability and social responsibility appeal. However many critics are raising doubts about the effective oil yield of jatropha in low-quality soils and the likely competition between food and this oil crop in developing countries. In Brazil there are several crops for HEFA production, as shown by figure 1.4, in Europe the main candidate is rapeseed, in sub-Saharan Africa is Jatropha and in Asia is Palm.

2.7.3 HEFA Biofuels

In the HEFA fuels production, the oil or fat is submitted to a sequence of reactions beginning with cracking the triglyceride into its respective fatty acids, following a hydrogenation, decarboxylation, decarbonylation, and a hydrodeoxygenation. The result is a mixture of CO, CO_2, H_2O, propane and the target synthetic fuel, composed by normal and branched alkanes, depending on the used feedstock. Figure 2.7 shows a typical reaction route for HEFA fuel production.

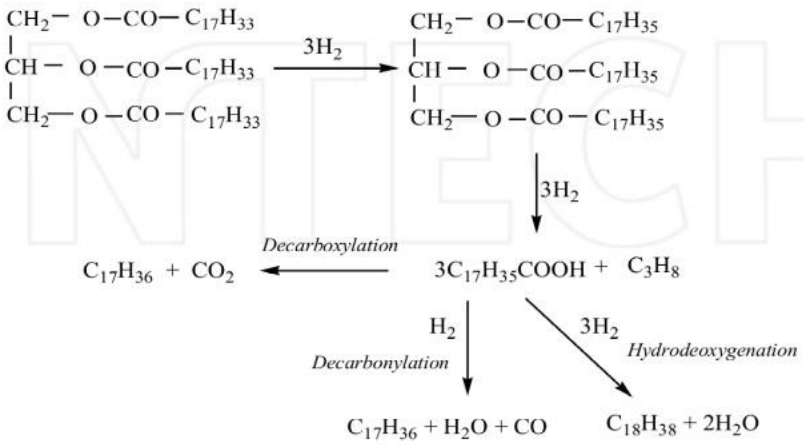

Figure 2.3– Typic reaction route for HEFA fuel production. Adapted from (Sotelo-Boyás, Trejo-Zárraga, & Felipe de Jesús Hernández-Loyo, 2012).

Hydroprocessing was used to produce fuel for many test flights, with the advantage that the resulting fuel looks very similar irrespective of the feedstock. The hydrotreating process branded ``Ecofining", developed by Honeywell's subsidiary UOP, yields a synthetic paraffinc kerosene (SPK) with around 85% iso and 15% n-paraffins in the C_9-C_{15} range, with high amounts of C_{10} and C_{11} compounds (Blakey et al., 2011; Corporan et al., 2011). According to (Meeks et al., 2011) albeit high in iso-paraffins these are much less branched compared to gasoline or diesel, usually containing only one methyl branch in a long-chain alkane, thus its effect is of little importance.

Regarding hydrotreated oil testing, it is possible to draw a parallel between airline efforts and military/manufacturer work. Tests flights conducted by Air New Zealand, Continental (now United) Airlines, Japan Airlines and KLM/Air France favored the use of HEFA fuels made from algae, camelina and jatropha oils. The HEFA fuels were blended with Jet A/A-1, in amounts up to 50%, and usually fueled one engine of the aircraft, thus allowing the study of engine relight and overall performance parameters like fuel consumption. The results of these test flights were mostly qualitative, with Air New Zealand claiming a potential fuel saving of 1.2% with its jatropha HEFA, which is in accordance with the data from UOP showing an energy content of 44.3 MJ/kg for this HEFA compared to 42.8 MJ/kg in Jet A-1 specification.

On the other hand, the US Air Force and US Navy, accompanied by

manufacturers like Boeing and Pratt & Whitney, elected HEFA fuels made from camelina and animal fats for their tests, that included engine performance, gaseous and particulate emissions (Blakey et al., 2011) . At first, all HEFA fuels produced less particle matter, which is expected due to the absence of aromatic compounds. In fuel blends, an increase in aromatic content and molecular weight resulted in a decrease in combustion efficiency, hence increasing carbon monoxide and unburned hydrocarbon emissions. The CO_2 and H_2O emissions are mostly related to the *H/C* ratio, hence the heating value, of the fuel, with HEFAs presenting hydrogen to carbon ratio above 2.0 while for conventional jet fuel this value is usually 1.95 or below. Finally, the nitrous oxide emissions, related to a combination of high temperature and residence time, are effectively dependent of the control system that drives the engine to a constant turbine inlet temperature.
(Blakey et al., 2011) concludes that an effective performance comparison between alternative and conventional fuels is hampered by the variable and extensive composition of Jet A/A-1 and JP-8. The authors also emphasize the need for a description of how the ratio of iso, normal and cyclic paraffins affect engine operation and material compatibility, as well as an extension of such model to aromatics.

2.7.4 Tests Using Alternative Fuels in the Brazilian Commercial Fleet

It were carried out in Brazil only a few experiments blending bioadditives to Jet A-1. Following (Soares, 2011) the first commercial flight using biodiesel blended Jet A-1 was carried out by the Brazilian AirLines TAM. One of the two CFM56-5B engines of an Airbus A320 aircraft was fueled by a mixture of 20% of Jatropha biodiesel and 80% of Jet A-1. The flight took about one hour and was considered a good flight and the engine worked fine.
The Brazilian aircraft assembler EMBRAER endeavored a series of tests in 2011. Following (Filogonio, 2011) EMBRAER was the first one to test the use of HEFA blended Jet A-1 in Brazil. (Filogonio, 2011) reported a series of experiments fueling one of the two GE CF34-8

engine of an EMBRAER 170 aircraft. They used a blend of 50% of camelina HEFA and 50% of Jet A-1. The results were reported as satisfactory confirming the use of HEFA fuels as a viable alternative to the aviation industry.

3 IGNITION, PROPAGATION AND EXTINCTION OF PREMIXED FLAME

The interest in this chapter are the flames that propagate in laminar and turbulent premixed mixtures. A premixed mixture is a molecularly homogeneous mixture of fuel and oxidizer. When the mixture is ignited locally and adequate conditions of temperature, pressure and composition exist, a flame is formed and propagates through the mixture converting reactants to products. Therefore, a flame is a chemical reaction oxidation front that propagates as a combustion wave. A deflagration wave is a combustion wave that propagates at speeds much lower than the speed of sound with respect to the unburned mixture. Figure 3.1 presents a flame propagating in the interior of a spherical constant volume vessel. This is the configuration of interest in this work. In the next sections, the ignition, propagation and extinction of premixed flames will be addressed.

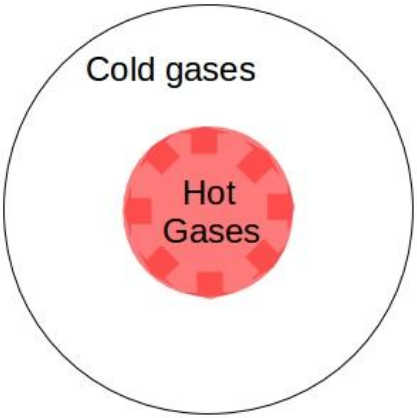

Figure 3.1– Flame propagation in constant volume reactor, dividing the gas in two homogeneous regions, a burned and an unburned region.

3.1 Flammability Limits after Spark Ignition

Flame propagation occurs when the premixed mixture is in a flammable condition. But, initially, the flame must be ignited. The main common ignition sources are the spark plug and the glow plug. Sometimes, a laser type source can also be applied. Consider the flame kernel created

in an n-dodecane/air mixture as shown in the rendering in Figure 3.1. If the mixture is within its ignitibility limits, combustion reactions will be initiated. The flame kernel has a radius r and uniform properties. Outside the kernel the gas has the properties of the unburned mixture. Figure 3.2 also presents a rendering of the temperature distribution within the kernel and external ambient. The heat flux from the flame kernel will be proportional to the temperature gradient between burned and unburned gases and to the mixture thermal conductivity. The presence of a laminar flow field or turbulence can enhance the heat transfer from the kernel to the unburned gases. As more reactants are brought to high temperatures upstream from the flame front, they are consumed by the combustion reactions and the flame moves forward. The propagation of the flame is also accompanied by volumetric expansion of the burned gases and by mass transfer in the flame region, caused by gradient of mass concentration.

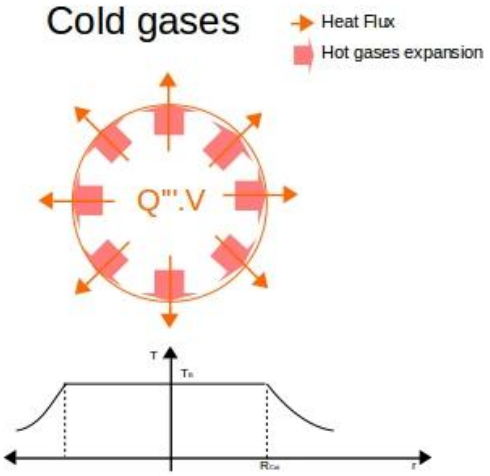

Figure 3.2– Spherical flame kernel representation. Q'''.V is the heat generated inside of flame kernel by the chemical reactions, Rcrit is the critical radius, TB is the temperature of the burned gases.

In general, the overall rate constant k for the combustion of hydrocarbon fuels increases with the increase in the temperature, an effect commonly modeled as an Arrhenius type equation,

$$k \sim exp\left(\frac{-E_A}{RT}\right) \tag{3.1}$$

where R is the universal gas constant and $E_A$is the overall activation energy. Therefore, the higher the temperature of the kernel, the faster is the consumption of chemical species and conversion to products. In a spark ignition, the temperature of the ionized medium increases to about 10,000 K (Glassman & Yetter, 2008; Turns, 2012; Warnatz, Maas, & Dibble, 2006) more than enough to overcome the explosion limit. Whether explosion will be followed by propagation depends on the relative magnitude between the thermal energy released by reaction within the kernel and the heat transfer rate by conduction to the surrounding unburned mixture. They contribute for propagation in opposite directions: the heat transfer rate cools the flame, which decreases the reaction rate, reducing the energy released, decreasing even more the temperature, and so on, in a feedback process. In this case, when the flame kernel suffers extinguishment, regardless of the power of the ignition source, the mixture is said to be out of its flammability limit. On the contrary, when the energy released from the chemical reactions overcomes the heat dissipation, the temperature in the flame front remains high enough to provide a high conversion rate of reactants, allowing a self-sustaining flame propagation. The mixture is said to be within its flammability limit. Applying a quasi-steady energy balance to the spherical flame kernel shown in the Figure 3.2, the simple order of magnitude argument for the minimum size of the flame kernel arises (Turns, 2012),

$$R_{crit} \sim \left(\frac{\alpha}{S_L}\right) \tag{3.2}$$

where R_{crit} is the minimum flame kernel radius that should be created by an ignition source in order to assure flame propagation, α is the thermal diffusivity, and S_L is the characteristic laminar burning velocity of the mixture. The burning velocity is proportional to the overall reaction rate. The higher the burning velocity, the smaller the critical radius can be, and thus the flame can be established using a weaker ignition source, or at least, consuming less energy.

(Coward & Jones, 1953) published a comprehensive report with results of flammability limits for gases and vapor mixtures covering 155 substances. The work was carried out in a joint project between the British and US Bureau of Mines, intended to be used as tool in safety efforts for the coal and mining industry. The experiments were done using a vertical glass tube with an inner diameter of 5 cm and 150 cm of height. In the bottom of the tube a spark plug was installed to ignite the

mixture. This ignition event may or may not induce an upward self-sustaining flame. The criterion to determine whether the mixture is considered flammable was visual. If the flame propagated along a predefined elapsed time at least half the length of the tube, the mixture was considered flammable. Figure 3.3 depicts the apparatus used by (Coward & Jones, 1953).

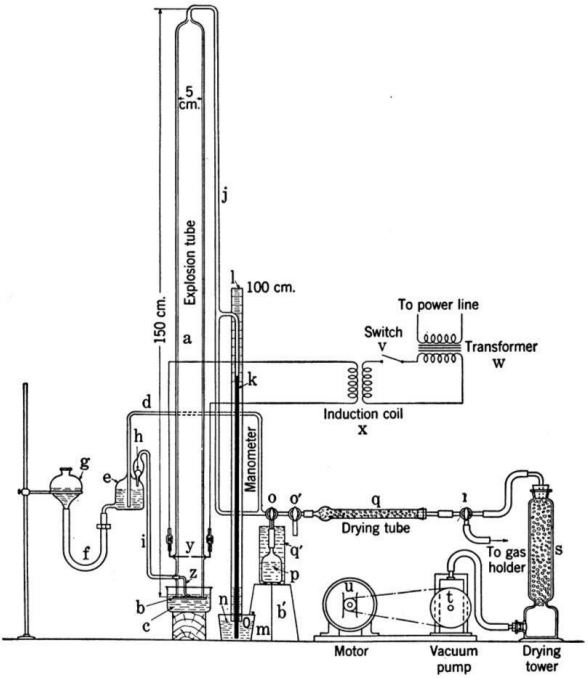

Figure 3.3– Apparatus for determining ignitability and limits of flammability of gases and vapors. Adapted from (Coward & Jones, 1953).

The methodology used by (Coward & Jones, 1953) was based on the fact that mixtures near their flammability limits, in both lean and rich sides, present such a weak flame that could only propagate in the upward direction. This occurs due the fact that the weak flame is not strong enough to balance the thermal convection induced by the burned hot gases, thus propagating only upwards. (Zabetakis, 1965) continued the work of Coward and Jones using the same facility. The methodology was also the same. (Zabetakis, 1965) published some new results and updated some already published. An important contribution was to publish results in terms of ignition energy curves. Figure 3.4 shows the

ignition and flammability limits for methane-air mixtures, in a plot of spark energy versus the methane volume-percent in the mixture. The use of the mixture strength in terms of the volume percentage instead the use of the fuel equivalence ratio is related with the operational practice in the mining and coal industry. The results showed in the Figure 3.4 are used until today as reference for methane flammability limits.

Presently, there are four main standards for the determination of flammability limits: DIN 51649-1, EN 1839T, ASTM E681-01 and EN 1839B. Three of them employ the visual criterion method to establish flammability. The last one utilizes a pressure method. When the final pressure in the experiment vessel is 5% higher the initial pressure, flame propagation was considered successful. (Coronado et al., 2012) published a comprehensive work on flammability limits for ethanol applied to the aviation industry, based on these standards.

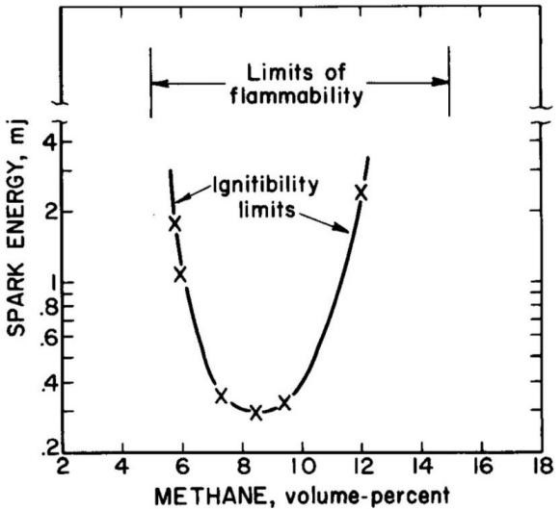

Figure 3.4– Ignitibility and flammability limits of methane/air mixtures. Adapted from (Zabetakis, 1965).

Since the work of (Zabetakis, 1965), ignition was also studied in the context of turbulent flows. Ignition becomes an statistical artifact whose probability is related to the following characteristics (Bane, 2010; Shepherd, Nuyt, & Lee, 2000): (1) the composition of the mixture, including the presence of diluents, humidity and burned gases; (2) the intensity of the turbulent flow; (3) the control and strength measurement of the ignition device; (4) the method of detection of the ignition event;

and (5) the electrodynamics and fluid dynamics near the spark.
Following this statistical concept, each experimental shot can evolve to only two events: ignition (1) or not ignition (0). The outcomes of a sequence of ignition tests, designed using the Langley Method (Langley, 1963), are statistically treated applying the cumulative probability of the ignition events. Considering a binary outcome model (Bane, 2010), the spark ignition tests give a binary array of results, *y*, where *y* = 1 for a "go" (ignition) and *y* = 0 for a "no go" (no ignition), as a response to a certain stimulus level (spark energy, equivalence ratio) *x*. If *W* is the threshold stimulus for a "go" result, then

$$\text{y} = 1, \text{ if } x \geqslant W$$
$$\text{y} = 0, \text{ if } x < W$$

Then a probability distribution for a "go" (ignition) at stimulus level *x* (spark energy) can be defined as,

$$P(x) = Probability(y = 1; x)$$

For n tests, all of them filled with new samples (mixtures), the following parameters are then defined: xi = stimulus level (spark energy) for the i_{th} test, yi = result for the i_{th} test (= 0 or 1), $P(xi)$ the probability that yi = 1 for the i_{th} test.

All the stimulus levels and the binary results for the n tests are represented using the likelihood function,

$$L = \prod_{i=1}^{n} \left(P(x_i)\right)^{y_i} \left(1 - P(x_i)\right)^{1-y_i} \tag{3.3}$$

The probability distribution function $P(x)$ can be represented with the parametric logistic distribution function,

$$P = \frac{1}{1 + exp(-(x - \beta_0)/\beta_1)} \tag{3.4}$$

where β_0 and β_1 are parameters that are obtained by maximizing the likelihood function. The β_0 result is used as the main result and β_1 is the inclination of the logistic distribution function, proportional to the standard deviation of the experiments outcome.

One of the main goals of the application of the statistical treatment to ignition events is to include in the response, the influence of the hard controlled experimental variables, such as mixture formation, turbulence, flame detection, and spark strength.
Following these considerations (Bane, 2010) reported results for ignition tests performed in lean hydrogen-based aviation test mixtures and two hexane/air mixtures, using a rectangular CVR with an inner volume about 11 liters (19 cm x 19 cm x 30.5 cm). The ignition was achieved using a low-energy capacitive spark ignition system. The CVR was equipped with a Schlieren set up and a dynamic pressure transducer. The spark energy range for each mixture was designed using the One Shoot Method, or Langley Method (Langley, 1963). A total number of 25 shots was deemed as sufficient to provide a statistically significant result. The author also provided a Matlab code that calculates the Logistic likelihood function from the measurements. Their results based on the SAE Aerospace Recommended Practice 5416 Aircraft Lightning Test Modes, using a reference mixture of 5% of hydrogen, 12% of oxygen and 83% of Argon in volume, were reported in terms of the ignition energy for 50% probability of a flame propagation to occur. The results for 5%, 6% and 7% of hydrogen in the mixture were 145.5, 351.5 and 951.5 microJoule respectively. Comparing the results obtained using the classical concept of the Minimum Ignition Energy – MIE (Bernard Lewis, 1961), the results reported by (Bane, 2010) were 42%, 134.33% and 375.75% higher, respectively. This difference was deemed due limitations of the MIE method, which are outdone by the statistical method.

3.2 Laminar Premixed Flame

3.2.1 Laminar Flame Structure

An unambiguous way to describe a flame is defining a perfectly planar deflagration wave. Consider a long cylindrical tube with open extremities. The tube is filled with a premixed homogeneous flammable mixture that is allowed to come to rest. The stationary mixture is then ignited and a flame propagates. Figure 3.5 presents a rendering of this situation. The velocity of the flame control volume with respect to the laboratory frame of reference is S_F. The velocity of the unburned mixture in respect to the laboratory frame of reference is depicted as u_{ug} while the velocity of the burned gases with respect to the laboratory frame of reference is depicted as u_{bg}. V is the velocity at which the gases

cross the flame control volume, the burning velocity. $V_{B/bg}$ is the burning velocity evaluated at the burned gases side and $V_{B/ug}$ is the burning velocity evaluated at the unburned gases side.

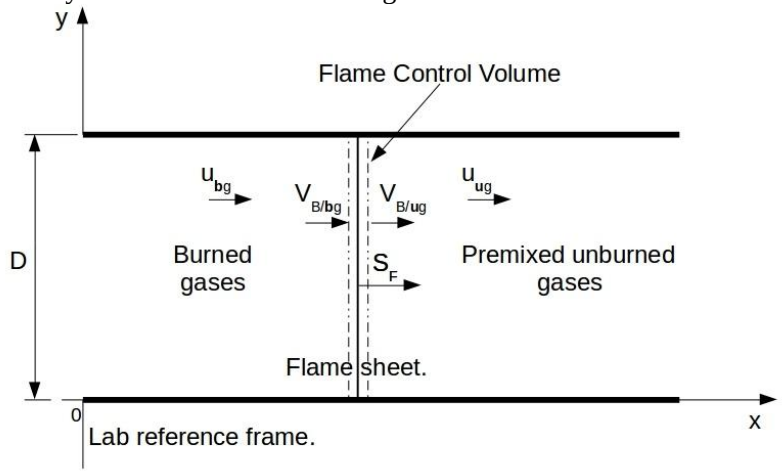

Figure 3.5– Laminar flat flame ignited inside of a very long tube with open extremities.

Stating x_{flame} as the position of the flame sheet with respect to the stationary frame of reference (a laboratory frame of reference), the speed of the flame sheet displacement, or simply, the flame speed S_F, is the time derivative of the distance the flame traveled, i.e.,

$$S_F = \frac{d\left(x_{flame}\right)}{dt} \tag{3.5}$$

In the concept of flame sheet, the flame is viewed as a thin front separating the burned gas and unburned gas regions. However, in the scale of the flame front, the flame structure would reveal the distribution of temperature, concentration of chemical species and reaction rate, evidencing that the flame itself has a characteristic thickness related to phenomena that occur at the flame level. Figure 3.6 presents a rendering of typical temperature, mass fraction of the deficient reactant and overall reaction rate distributions within the flame depicted in Figure 3.5.
Figure 3.6 shows that the mass fraction of the deficient reactant, say the fuel for a lean flame, Yu decreases along the flame, driven mainly by mass diffusion towards the reaction region. Conversely, the temperature

decreases from the burned to the unburned region, driven by the heat conduction to the unburned reactants. The important chemical reactions that promote most of the energy release in the flame occur in a very thin reaction region, at a temperature close to the flame temperature T_b. This concept is the basis of a comprehensive flame analysis tool named asymptotic flame analysis (Pereira, Oliveira, & Fachini, 2011; Williams, 1986).

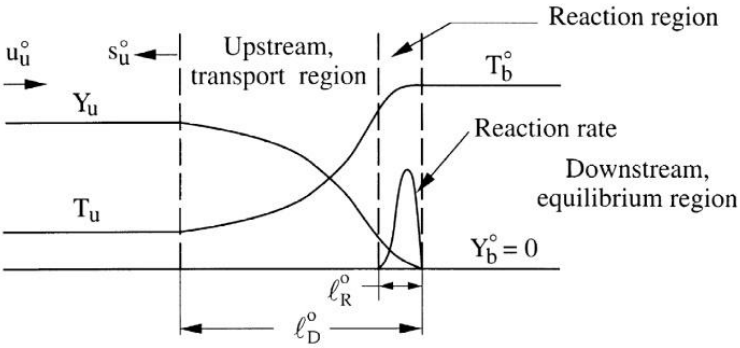

Figure 3.6– Detailed flame sheet with the indication of the thermal flame thickness l_D^0 and the reaction thickness l_R^0, called "reaction region". The letters "u" and "b" mean unburned and burned respectively. "Y" is the mass fraction of the deficient reactant, s_u^0 is the flame speed and u_u^0 is the speed of the unburned reactants related with the flame. Adapted from (Law & Sung, 2000).

The flame propagation occurs as a result of the heat transfer rate by conduction from the burned to the unburned regions. This heat transfer rate occurs over a diffusion length scale named the thermal flame thickness l_D^0. Mallard and Le Chatelier and then Z´eldovich, Frank-Kamenetskii and Semenov (Bernard Lewis, 1961; Glassman & Yetter, 2008; Turns, 2012; Warnatz et al., 2006; Williams, 1986) applied a simple heat balance around this region and obtained the simple order of magnitude concept,

$$l_D^0 = \frac{\alpha(\bar{T})}{S_L} \tag{3.6}$$

where α is the thermal diffusivity evaluated at the average temperature $\bar{T}$ between unburned T_u and burned T_b temperatures and S_L is the laminar flame speed. Since the overall activation energy is large for hydrocarbon flames, the thickness of the reaction region l_R^0 is much smaller than the

thickness of the thermally affected regionl_D^0. Therefore, the thickness of the flame front is basically equal to l_D^0. The flame temperature T_b is related to the amount of energy released in the flame and this is the main effect in the flame speed. Therefore, mixtures that promote stronger heat release, such as mixtures near stoichiometry, result in faster speed and thinner reaction fronts.

3.2.2 Effect of Mixture Flow

The flame propagation may occur superimposed to the expansion of hot gases and compression of the unburned mixture. This is a situation that occurs in a spherical flame confined within a closed reactor, as depicted in Figure 3.7. In this situation, the flame is ignited in the center of the reactor and propagates outwardly with the flame speed S_F given by,

$$S_F = \frac{d(r_F)}{dt} \tag{3.7}$$

where r_F is the position of the flame front.
Now, the flame propagation is influenced by two effects. First, the unburned gases are compressed by the expansion of the burned gases, and both are constrained by the reactor wall. Second, the curvature of the flame modifies its inner structure. The first effect will be analyzed in this section, while the effect of curvature will be analyzed in the next section.

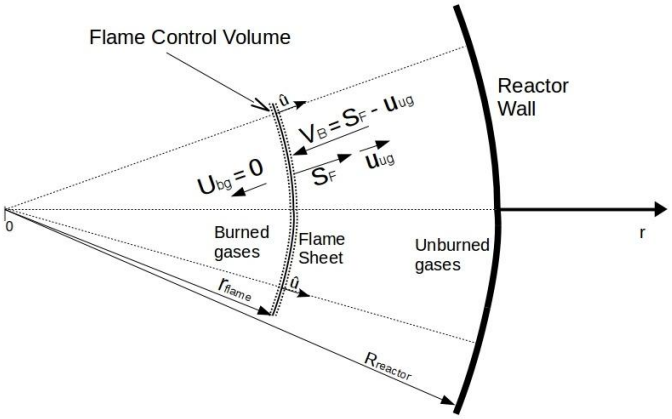

Figure 3.7– Sketch of a spherical flame propagating inside a constant volume reactor. VB is the burning velocity and û is the unity normal vector.

In this flame, the unburned gases are pushed forward as a result of the expansion of the burned gases. Considering the same nomenclature showed in Figure 3.5, a mass balance applied to a control volume around the flame moving with the flame speed S_F provides,

$$\rho_u A(u_{ug} - S_F) = \rho_u A(u_{bg} - S_F) \tag{3.8}$$

where ρ_u and ρ_b are the densities of the unburned and burned mixtures, respectively, and A is the flame surface area.
The velocity of the unburned mixture with respect to the laboratory frame of reference u_{ug} has two components: one due to the expansion of the burned gases and the other related to the consumption of reactants in the flame front. On the other hand, the velocity of the burned gases in respect to the laboratory frame of reference is zero, since they are constrained to occupy the center of the reactor. The mass balance applied to the control volume around the flame then becomes,

$$\rho_u A(u_{ug} - S_F) = -\rho_u A S_F \tag{3.9}$$

Since the velocity of the burned gases with respect to the laboratory frame of reference was considered zero, only the burning velocity at the unburned gases side exist,

$$V_B = u_{ug} - S_F \tag{3.10}$$

Equation 3.10 can also be written as,

$$V_B = \frac{\rho_b}{\rho_u} S_F \tag{3.11}$$

where ρ_b/ρ_u is named the expansion factor. For common hydrocarbon flames at 100 kPa, and temperatures near 400 K, chemical equilibrium calculations give $\rho_b/\rho_u \simeq 8$.
The results of burning velocity for perfectly planar, stretch free and

adiabatic flames are normally presented as the *Laminar Flame Speed* – S_L. This laminar flame speed coincides with the consumption speed defined by (Poinsot & Veynante, 2005).

3.2.3 Effect of Flame Curvature

Flames observed in combustion devices and in laboratory experiments are seldom perfectly planar. The flow may produce flame curvatures and the flame propagation itself induces instabilities, intrinsically related with the hot gases expansion (Matalon, 2007).
The propagation of the flame in the spherical vessel, presented in the previous section, is affected by curvature. The flame expansion produces a thinning effect in the thermal region. In the limit for very high curvature, i.e., small flame radius, the mass diffusion and heat flux vectors may be nonaligned in respect to the unburned and burned velocity vectors, resulting in two-dimensional mass and heat transfer over an essentially one-dimensional flow field. The two-dimensional heat and mass transfer modifies the internal structure, altering the flame consumption speed. This type of flame alteration caused by geometrical constraints is commonly called *curvature stretch*.

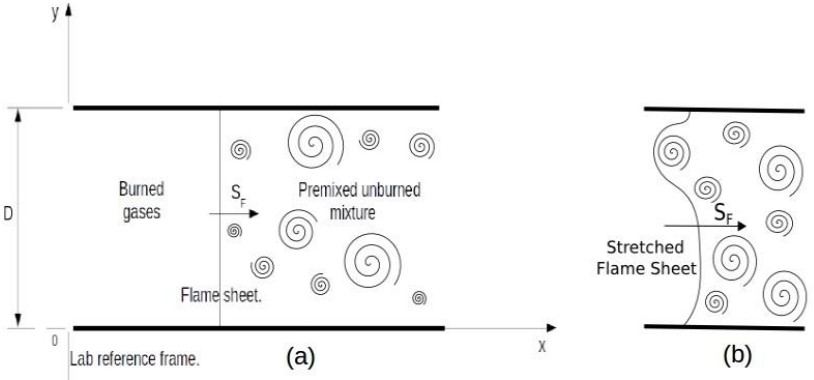

Figure 3.8– Tube flame configuration propagation into a swirled flow field. The picture (a) is the downstream swirled flow field. Picture (b) shows some possible effects of the interaction between the flame sheet and the swirls.

Another source of interference on the flame structure can be caused by downstream flow structures, such as recirculation zones, swirls, and vortices, which can be induced by turbulence or obstacles placed across the flow field. Figure 3.8 presents a rendering of a hypothetical plane

flame before and after interaction with a downstream swirled flow.
The type of flame interactions shown in Figure 3.8 are normally called *strain stretch*. The flames of interest for practical application and for laboratory studies are almost always submitted to curvature stretch, strain stretch, or both. Flame stretch can even lead to local flame extinction.
The flame stretch rate quantifies the magnitude of the flame stretch (Law & Sung, 2000; Law & Wu, 1984; Matalon, 2007; Poinsot & Veynante, 2005). It is fundamentally calculated as,

$$\kappa = \frac{1}{A}\frac{dA}{dt} \tag{3.12}$$

where κ is the flame stretch rate and A is the flame front area, evaluated at the reactants side. The flame stretch rate will be a key parameter in the further flame measurements description. For the spherically expanding flame,

$$\kappa = \frac{2}{R_F}\frac{d(R_F)}{dt} \tag{3.13}$$

Therefore, the smaller the radius the larger is the flame stretch rate.
Early measurements of flame speed did not take into account effects of flame stretch. Figure 3.9 illustrates the values of laminar flame speed near stoichiometry for methane – air flames measured over the last 100 years. The scatter observed in the results presents a remarkable reduction around the beginning of the 1980's. Following (Egolfopoulos et al., 2014), this improvement is attributed to advances in measurement methods and modeling, mainly due the inclusion of the *flame stretch rate*.

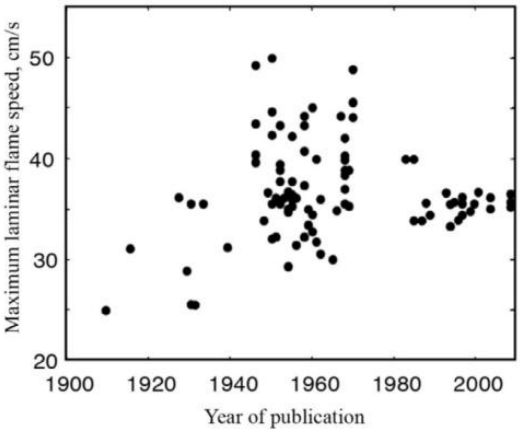

Figure 3.9– Measurements of laminar flame speed of stoichiometric air/methane mixture at 298 K, 101 kPa, obtained by several research groups during the 20th century. Adapted from (Ranzi et al., 2012).

(Law & Wu, 1984) were pioneers in this approach when they proposed a simple linear relation between the laminar flame speed and stretch rate,

$$S_L = V_B + Ma\kappa \tag{3.14}$$

where S_L is the laminar flame speed, V_B is the burning velocity measured with respect to the unburned mixture, Ma is the Markstein Length and κ is the flame stretch rate. The laminar flame speed S_L is obtained from an extrapolation of measurements of V_B at different values of κ to $\kappa = 0$. The Markstein length is the slope of the straight line. This method is applied in particular to two methods of measurement of laminar flame speed: the counter flow burner and the spherically expanding flame. The analysis of the spherically expanding flame will be presented later.

3.3 Turbulent Premixed Flame

The majority of flames in applications occur under or, at least, are influenced by turbulent flows. A flame occurring on a turbulent flow is called a turbulent flame.

Turbulent flows are inherently unsteady and chaotic. Statistically isotropic turbulence means that all statistics applied over the field of flow variables are invariant under translation, rotation and reflection of

the coordinate system. Turbulent motions are distributed over a large range of spatial and velocity scales. The turbulent kinetic energy $\bar{k}$ is related to the root mean square (rms) of the velocity fluctuations. The rate of dissipation ϵ expresses the rate in which turbulent kinetic energy is dissipated by viscous effects. The Kolmogorov hypothesis (Kolmogorov, 1941) states the turbulent kinetic energy is continuously transferred from the vortices with the largest length scale l_0 to the vortices with the smallest length scales η_k, where viscosity dissipates the turbulent kinetic energy into internal energy. The range of length scales between η_κ and l_o is named the inertia subrange.
The velocity fluctuation for the largest vortices u', named the integral velocity, scales with the turbulent kinetic energy as,

$$u' \sim \sqrt{\frac{2}{3}\bar{k}} \tag{3.15}$$

The velocity fluctuation u' is also the turnover velocity of integral scale eddies. Denoting l_0 as the characteristic length scale of these integral eddies, the integral time scale is given by,

$$\tau_t \sim \frac{l_0}{u'} \tag{3.16}$$

Kolmogorov's theory states that the energy transfer from large eddies is equal to the dissipation of energy at the Kolmogorov scale. Then,

$$\epsilon \sim \frac{(u')^3}{l_0} \tag{3.17}$$

Since ϵ is constant along the inertial subrange, the same scaling applies to any eddy of characteristic size l_n and velocity u'_n,

$$\epsilon \sim \frac{(u'_n)^3}{l_n} \tag{3.18}$$

In particular, at the Kolmogorov scale,

$$\epsilon \sim \frac{(u'_\kappa)^3}{l_\kappa} \tag{3.19}$$

where u'_κ is the turnover velocity of an eddy at the Kolmogorov scale. Comparing the integral and the Kolmogorov scales, we obtain the relation,

$$\left(\frac{u'}{u'_\kappa}\right)^3 \sim \frac{l_0}{\eta_\kappa} \tag{3.20}$$

Therefore, eddies with larger sizes are associated to larger turnover velocities.
From the Kolmogorov hypothesis, the inertia and viscous forces are in balance at the Kolmogorov scale, and therefore, a Reynolds number at the Kolmogorov scale provides,

$$Re_\kappa \equiv \frac{u'_\kappa \eta_\kappa}{\nu} = \frac{\epsilon^{(1/3)} \eta_\kappa^{(4/3)}}{\nu} = 1 \tag{3.21}$$

where ν is the kinematic viscosity. This hypothesis leads to a relation between the Kolmogorov length scale and the rate of dissipation of the turbulent kinetic energy,

$$\eta_\kappa \equiv \left(\frac{\nu^3}{\epsilon}\right)^{(1/4)} \tag{3.22}$$

The Kolmogorov velocity fluctuation is then given by,

$$u'_\kappa \equiv (\nu\epsilon)^{(1/4)} \tag{3.23}$$

Therefore, a Kolmogorov time scale can also be defined as,

$$\tau_\kappa \equiv \frac{\eta_\kappa}{u'_\kappa} \sim \left(\frac{\nu}{\epsilon}\right)^{(1/2)} \tag{3.24}$$

The interaction between a premixed flame and a turbulent flow may be conveniently described by the interplay between the turbulence and the premixed flame length and velocity characteristic scales.
At the integral scale, the turbulent Reynolds number is defined as,

$$Re_t = \frac{u' \imath_0}{\nu} \tag{3.25}$$

The Schvab-Zeldovich approximation is used and we may assume that both the Prandtl and the Schmidt numbers are unit, i.e., $\nu \sim \alpha$ and $\alpha \sim D$. Assuming that the laminar flame structure provides suitable chemical velocity and length scales, we may write $\alpha \sim l_D^o S_L$.Then, the turbulent Reynolds number is rewritten as,

$$Re_t = \frac{u'}{S_L} \frac{\imath_0}{\imath_D^0} \tag{3.26}$$

The turbulent Damköhler number relates the chemical τ_c and the integral turbulent τ_t time scales as,

$$Da = \frac{\tau_t}{\tau_c} \tag{3.27}$$

Assuming that the characteristic time of the chemical reactions may be conveniently based on the laminar flame thermal characteristic length l_D^o and speed S_L,

$$\tau_c = \frac{\imath_D^0}{S_L} \tag{3.28}$$

the turbulent Damkohler number may be written as,

$$Da = \frac{\tau_t}{\tau_c} = \frac{S_L}{u'}\frac{\iota_0}{\iota_D^0} \tag{3.29}$$

This number relates the rate of turbulent transport of species at the integral scale and the rate of consumption by chemical reaction. When$Da < 1$, the rate of transport of species provided by turbulence in the larger scales is faster than reaction can consume. Therefore, even the largest eddies embed themselves within the flame before they can be burned. The flame structure is completely destroyed and reaction occurs in a homogeneous way. When $Da > 1$, the chemical reactions are faster than the largest eddies and the flame moves over these eddies consuming the reactants before they can complete their turn. However, smaller eddies can still penetrate the flame thermal region affecting the flame structure. Therefore, the flame becomes distorted by the larger eddies and thickened by the enhanced transport provided by the smaller eddies.

The Karlovitz number relates the chemical $\tau_c$and Kolmogorov turbulent $\tau_\kappa$characteristic time scales as,

$$Ka = \frac{\tau_c}{\tau_\kappa} \tag{3.30}$$

The thermal length scale for the laminar flame scales with the laminar flame speed as $l_D^o \sim \alpha/S_L$. Therefore, the chemical time scale can also be written as,

$$\tau_c = \frac{\iota_D^0}{S_L} \sim \frac{\alpha}{(S_L)^2} \tag{3.31}$$

Taking the Kolmogorov time scale and recalling that ν ~ α, we obtain,

$$Ka = \frac{\tau_c}{\tau_\kappa} = \left(\frac{u'_\kappa}{S_L}\right)^2 \tag{3.32}$$

The Karlovitz number, also called the first Karlovitz number (Peters, 2000), relates the rate of species turbulent transport at the Kolmogorov scale and the species consumption by chemical reaction. When $Ka > 1$, the chemical time scale is larger than the time scale for the turnover of a

Kolmogorov eddy. Therefore, even the smallest eddies penetrate the flame structure before they are completely burned. They enhance the internal heat and mass transfer, resulting in enlargement of the thermal flame thickness and increase of the burning rate. However, the reaction length scale may remain unaltered since it is about 10 times smaller than the thermal length scale. Conversely, when $Ka < 1$, chemical reaction is faster than the turn over of the smallest turbulent eddies. Then, the flame can burn the smaller eddies before they can significantly affect the flame structure, which keeps its quasi-steady structure. However, larger eddies have higher velocity and eddies larger than a given size, the Gibson scale, can still deform the flame sheet. Therefore, this regime results in highly distorted flame fronts that tend to propagate along the border of the larger turbulent eddies consuming reactants from the external layer to the center. When the distortion is sufficiently high, the flame front may bend and snap off, forming pockets of burned or unburned gases. The snap off may be followed by either local reignition or extinction.
The Borghi diagram identifies the regimes for turbulent combustion as delimited by the turbulent Reynolds, the Damköhler and the Karlovitz numbers. The Borghi diagram is reproduced in Figure 3.10.

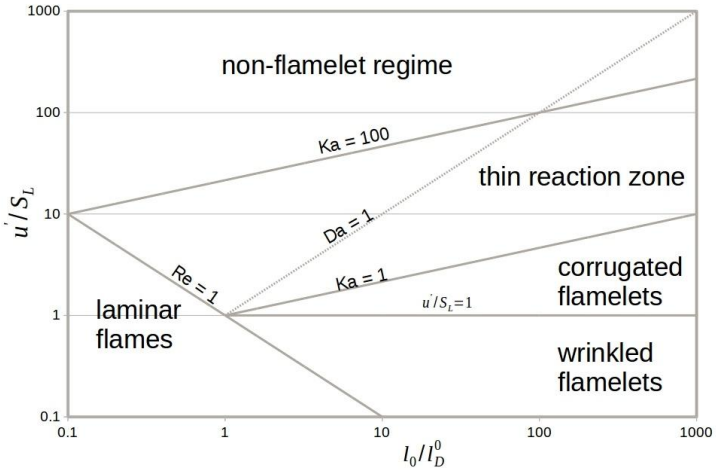

Figure 3.10 – Borghi diagram. In the abscissa axis, the nondimensional length is the quotient between the turbulent integral length scale and the flame thermal thickness. In the ordinate axis, the nondimensional velocity is the quotient between the turbulent RMS velocity and the laminar flame speed. Adapted from (Warnatz et al., 2006).

The laminar regime is the limit for small turbulent Reynolds number. The turbulent region can be reached either by increasing the velocity fluctuation, or by increasing the integral length scale. The region under the line $u'/S_L = 1$, the wrinkled flamelet regime, is characterized by small turbulence intensity and small flame surface interactions. Basically, an essentially laminar flame sweeps over the mixture burning all the turbulent structures without alteration of the laminar flame structure or flame sheet. The region for $u'/S_L > 1$and $Ka < 1$is the corrugated flamelet regime, where vortices larger than the Gibson scale cause significant bending and stretching of the flame sheet. The Gibson scale is the characteristic eddy size that turns with velocity equal to the laminar flame speed,

$$\iota_G \sim \frac{S_L^3}{\epsilon} \tag{3.33}$$

Therefore, eddies with characteristic length scale smaller than l_G are engulfed by the flame before they can distort it, while eddies with size larger than l_G deform and stretch the flame sheet. The line $Ka = 1$defines the limit where $l_D^o \sim \eta_\kappa$, i.e., the Kolmogorov eddies penetrate the thermal flame region before they are burned. This is called the Klimov-Williams limit. The region delimited by $Ka > 1$and $Da > 1$is named the distributed reaction regime. In this region, $\eta_\kappa < l_D^o$ and the thermal flame region is thickened by the enhanced turbulent transport provided by the smaller eddies. However, the flame reaction thickness is still larger than the Kolmogorov length scale, $\eta_\kappa > l_R^o$. Assuming that $l_R^o \sim 0.1 l_D^o$, $\eta_\kappa \sim l_R^o$ when $Ka = 100$. In this case, the Damköhler number becomes smaller than 1 and the entire flame structure is changed by the turbulent flow. Finally, the region for $Da < 1$ is the well stirred reactor regime, where turbulent mixing promotes homogeneous reaction in the whole mixture. A flame sheet is no longer existent.
(Gomez, 2011) related the regimes in the Borghi diagram to the combustion patterns observed in internal combustion engines and gas turbines, as shown in Figure 3.11.

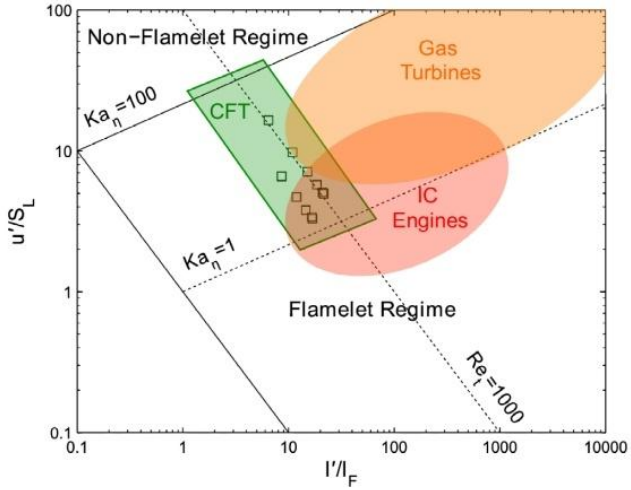

Figure 3.11 – Turbulent combustion regimes and the respective regions related with IC engines and gas turbines. Adapted from (Gomez, 2011).

We note that the combustion regime for gas turbines is mostly located in the distributed reaction regime, in the region where eddies enlarge the flame thermal region, but do not change the flame reaction region ($1 < Ka < 100$). The structure of the flame reaction region remains the one obtained from a quasi-steady solution for a laminar flame and no appreciable distortion of the flame sheet is observed. A laminar flamelet concept is no longer applicable. Combustion in internal combustion engines, on the other hand, may extend to the corrugated flamelet regime, where eddies with size above the Gibson scale distort the flame sheet and eddies with size below the Gibson scale affect the structure of the flame thermal region. The flame becomes thicker and appreciably distorted. There is the formation of cold and hot pockets and, possibly, local extinction and reignition events. A laminar flamelet concept is, in principle applicable, but the flame thermal region must be modeled including the effect of turbulence.

Assuming that combustion occurs in a flamelet regime, the velocity of propagation of a turbulent flame brush is related to the laminar flame velocity and in some measure to the entrainment of turbulent eddies. The idea originally developed by Damkohler has evolved in many different models and approaches (Poinsot & Veynante, 2005; Warnatz et al., 2006). One simple relation that approximately accounts for these effects is,

$$\frac{S_T}{S_L} = 1 + \omega \left(\frac{u'}{S_L}\right)^n \quad (3.34)$$

where S_T is the turbulent flame speed, S_L is the laminar flame speed u' is the RMS turbulent velocity, $\omega > 0$and $n > 0$ are constants.
In order to apply this correlation, S_L must be known or measured in an independent way. The velocity fluctuation must be characterized for the given flow or experiment, if possible, under hot conditions. The constants, in principle, depend on stoichiometry and other characteristics of the flow field. They are in no sense general for a given fuel, but are strongly dependent on the characteristics of the combustion system, or laboratory device (Bradley, Lawes, Liu, & Mansour, 2013). Therefore, for a given laboratory device, this correlation is more suitable as a means to compare the relative behavior of different mixtures.

3.4 Ignition Delay Time

Prior to flame propagation, or during a reignition event on a flame brush, the fuel/air mixture must undergoes auto ignition. During auto ignition, i.e., ignition without the aid of an ignition device, a homogeneous premixed fuel mixture is brought to high temperature and pressure and undergoes thermal ignition. Thermal ignition is the homogeneous ignition event in a reactant mixture as a result of a sudden increase in temperature. Ignition delay time is the time elapsed from the temperature change to the thermal runaway of the mixture. The ignition delay occurs as a result of the required time for the initiation reactions to build up the radical pool needed to propagate the chain mechanism (Glassman & Yetter, 2008).
The fast temperature increase is produced in laboratory usually by fast compression, either promoted by a piston, or by the passage of a shock wave. The former is carried out using a rapid compression machine - RCM, while the latter is obtained using a shock tube - ST. In both experiments the initial pressure is set to a desired value. The temperature range for shock tube experiments is above 950 K and for the RCM, the range is about 650 K to 1000 K. ST may operate up to 130 bar, while RCM usually operate up to 30 bar. Both instruments rely on the recording of pressure history or light emission from the combustion section to evaluate the ignition delay time. The conditions that prevail in the combustion region are assumed uniform and adiabatic (Werler et al.,

2015), a hypothesis known as the adiabatic core hypothesis. (Mittal & Sung, 2006) published a comprehensive study about the effects of the combustion chamber and piston head design on the aerodynamic and temperature fields within the RCM. In ST, the formation of boundary layer causes deviations from the adiabatic core hypothesis. The time window of measurement is in the range of 0.001 to 10 ms for the ST and from 1 to 100 ms for the RCM. Therefore, both measurements are complementary, the RCM being more indicated to measure low temperature ignition, while the ST being more appropriate to high pressure, high temperature measurement.

The ignition delay usually decreases as temperature increases and pressure increases. This has been usually modeled using Arrhenius type equations. This typical high-temperature kinetics behavior derives from the detailed chemical kinetics of the smaller chemical species included, for example, in the kinetics mechanism for methane. The kinetics of hydrogen peroxides, included in the mechanism for hydrogen, are of particular importance. The rate constants for the small species depend strongly on pressure, but these effects are well accounted for by the formalism proposed by Troe and is taken into account in many chemical kinetics models available. These have been extensively tested for temperatures above 900 K and are currently quite reliable as tools for estimates (Simmie, 2003). However, when ignition occurs at temperatures lower than 900 K, a behavior known as Negative Temperature Coefficient (NTC) can occur. Figure 3.12 shows ignition delay time results for mixtures between n-heptane and iso-octane/air, at variable initial pressures. N-heptane presents a lower ignition delay time when compared with iso-octane. In the region from 700 K to 900 K the ignition delay time actually decreases as temperature is decreased. Normal alkanes such as n-heptane, contrary to branched alkanes such as iso-octane, present a very pronounced NTC. Also, NTC becomes weaker as pressure is increased, and is almost inexistent for iso-octane at 41 bar. For n-heptane instead, the NTC is still noticeable, even for higher pressures like 50 atm. Alkanes larger than n-butane present a NTC behavior as a result of the competition among alkyl radical production and recombination paths. Following (Battin-Leclerc, 2008), the reaction of hydrocarbons with air begins with an H-abstraction from the fuel by oxygen molecules. Alkanes form alkyl and hydroperoxy radicals.

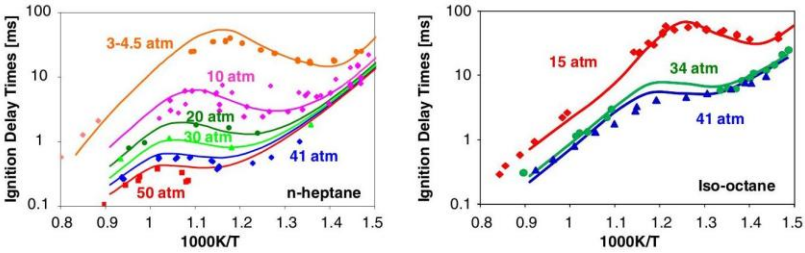

Figure 3.12 –Ignition delay times for n-heptane and iso-octane air stoichiometric mixtures. Adapted from (Naik, Westbrook, Herbinet, Pitz, & Mehl, 2011).

The peroxides include an O-OH bond which can be easily broken, leading to the formation of two radicals. These radicals in turn react with the alkanes giving more alkyl radicals. The growth of the number of radicals accelerate exponentially the chain reaction leading to ignition. At lower temperatures, on the other hand, the reversibility of the formation of alkyl radicals, i.e., the recombination of alkyl radicals with oxygen leading to the formation of alkenes, competes with the creation of radicals, leading to an overall reduction of the rate of reaction, resulting in the NTC. This is also common to longer alkanes. (S S Vasu, Davidson, & Hanson, 2009) presented results of ignition delay times of Jet-A and n-dodecane/air mixtures using a shock tube facility. Figure 3.13 shows some of their results.

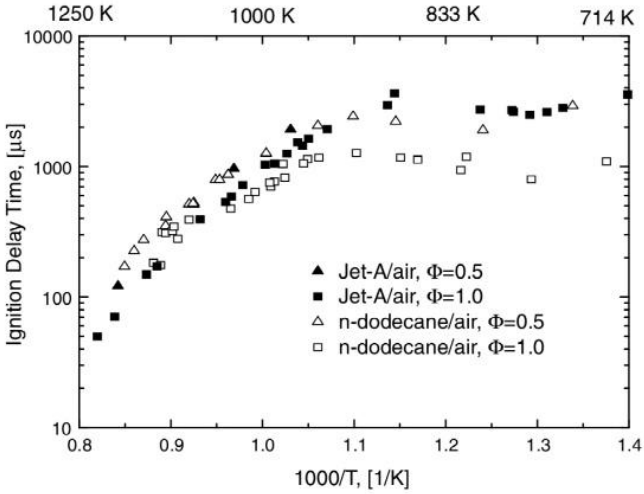

Figure 3.13 – Ignition delay times of Jet-A and n-dodecane air mixtures, normalized to a pressure of 20 atm. Adapted from (Subith S. Vasu, Davidson, & Hanson, 2008).

Figure 3.13 indicates n-dodecane mixtures have a shorter ignition delay time compared with the Jet-A, but the NTC behavior is similar for both. Therefore, chemical surrogates for Jet fuel must include alkanes in order to predict the lower temperature NTC region.

3.5 Concluding Remarks

This chapter summarized the basic phenomenology related to ignition, flammability, flame propagation and extinction of the fuel mixtures, suited to be burned inside of the jet engine combustion chamber. In this work, it is proposed that reliable methods for measurement of ignition, both thermal and spark-ignition, flammability limits, both in laminar and turbulent conditions, and burning velocity, both in laminar and turbulent conditions, comprise the minimum set of experiments needed to qualify the chemical suitability of a given fuel mixture.
The next chapter presents the experimental facilities and methods used for measurement of ignition, flammability limits and flame burning rates in this work.

4 EQUIPMENT AND METHODS

The combustion in the primary zone of a gas turbine, in a first approximation, may be considered a constant pressure process. As discussed above, the temperature can vary from 700 K in the coldest region to about 2200 K in the core combustion zone. For engine performance analysis, the cold region, where extinction and re-ignition events are more likely to occur, is more important. The development and use of jet fuels must take into account the combustion performance and stability along the normal operational envelope and through eventually unexpected events. The laboratory experiments used to qualify the fuel under the conditions in gas turbines must reflect the combustion phenomena and cover the desired range of temperature, pressure and stoichiometry. Besides, they should isolate the important chemical from physical phenomena that do not affect chemistry. Turbulence affects the formation and propagation of flames, as already discussed. Considering these requirements, the following laboratory measurements and analysis are proposed as reflecting the important chemical phenomena and chemistry-flow interactions that occur in the

combustion chamber of gas turbines:

- Thermal ignition, as measured by ignition delay time;
- Lean laminar flammability limits;
- Flame propagation in laminar and turbulent conditions;
- Flame kernel extinguishment caused by turbulence.

These measurements cover gas-phase, steady-state combustion phenomena and part of the transient phenomena. Critical stretch rate is measured only indirectly, while instability, wall quenching, and production of gas pollutants are not addressed.
In the following each equipment and method used in this work is described.

4.1 Ignition Delay Time

Ignition delay time is the time elapsed from a sudden temperature change to the thermal runaway of the mixture, leading to combustion. Here, a rapid compression machine (RCM) was used as a means to study low temperature, low pressure ignition.

4.1.1 Rapid Compression Machine Facility

The RCM facility used was described by (Werler et al., 2015). It is installed at the Institute of Technical Thermodynamics (ITT) of the Karlsruhe Institute of Technology (KIT), Karlsruhe/Germany. In this equipment, the reactant mixture is compressed by a piston driven by a pneumatic system. The combustible mixture is prepared within a mixing vessel, shown as number 2 in Figure 4.1. The mixing vessel was designed for temperatures up to 150 ºC. The vessel has an inner magnetic stirrer to provide a homogeneous mixture between the fuel and the oxidizer. The combustion chamber is preheated by an oil thermal bath. The pressure variation in the combustion chamber is recorded using a quartz sensor with a charge amplifier (Kistler 6061B, 5011B). A National Instruments interface programed in LabView is used for control and measurement.

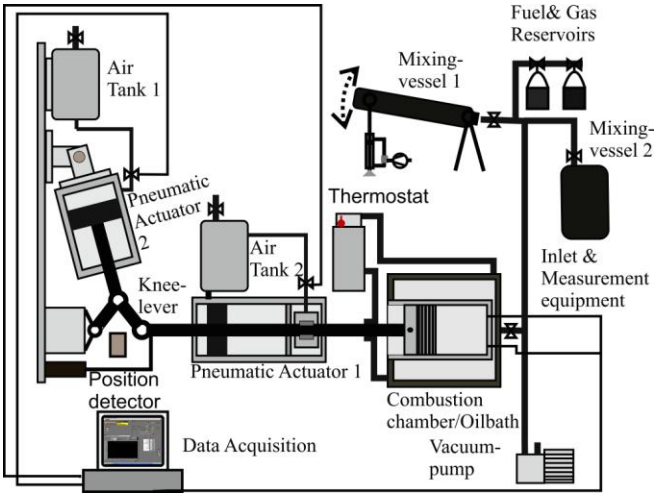

Figure 4.1 – Schematic of the ITT rapid compression machine facility. Adapted from (Werler et al., 2015).

A typical experiment starts with the application of vacuum in the RCM combustion chamber, connections and mixing tank. The mixture is prepared in the mixing chamber. Then, the combustion chamber is filled with the mixture, while the piston remains locked at the bottom dead center (BDC). The initial pressure and temperature are recorded. The start of the experiment is triggered by the Labview code and the pressure and piston displacements are then recorded. The synchronized operation of the pneumatic actuators number 1 and 2, showed in Figure 4.1, provides the movement of the piston towards the top dead center (TDC). The knee-lever mechanism provides deceleration of the piston and arrests it at TDC. As a result of the arresting mechanism, the piston presents a low level of oscillation in its position at TDC, keeping a steady pressure. Table 4.1 shows the main geometrical and operational characteristics of the RCM facility.

Table 4.1– Main geometrical and operational characteristics of the ITT RCM.

Bore	82.05 mm
Compression ratio	9.5 – 11.5
Stroke	77 – 80 mm
Compression time	15 – 25 ms
Driving pressure	3 – 10 bar

Accessible pressure range (post-compression)	2 – 25 bar
Initial temperature range	288 – 473 K
Accessible temperature range (post-compression)	500 – 1050 K

4.1.2 RCM Thermodynamics

Knowing the geometrical characteristics and the recorded time variation of pressure, it is possible to calculate all the thermodynamic data of interest. After the compression stroke, the homogeneous gas temperature inside the combustion chamber at TDC can be calculated from,

$$\int_{T_0}^{T_{eff}} \left(\frac{\gamma}{1-\gamma}\right)\frac{dT}{T} = log\left(\frac{p_{eff}}{p_0}\right) \tag{4.1}$$

where T and p are the temperature and pressure respectively, the subscripts 0 and eff are related with the initial, at the BDC, and final compression, at TDC, conditions respectively and γ is the ratio between the specific heats at constant pressure and volume.

The use of Equation 4.1 is based on the assumption that the mixture within the RCM has a homogeneous temperature, a hypothesis known as the adiabatic core hypothesis. This homogeneity condition can be approximated through the use of a creviced piston, instead of a conventional flat head piston. (Lee & Hochgreb, 1998; Mittal & Sung, 2006) published a comprehensive study about the effects of the combustion chamber design on the aerodynamic and temperature fields within the RCM, comparing the use of a flat and a creviced piston. The RCM used in this work has a creviced piston designed following the recommendations of (Mittal & Sung, 2006). Figure 4.2 shows the temperature calculated from a CFD solution of the compression in the RCM used here. The temperature fields show that the use of the creviced piston provides an almost ideal adiabatic homogeneous core.

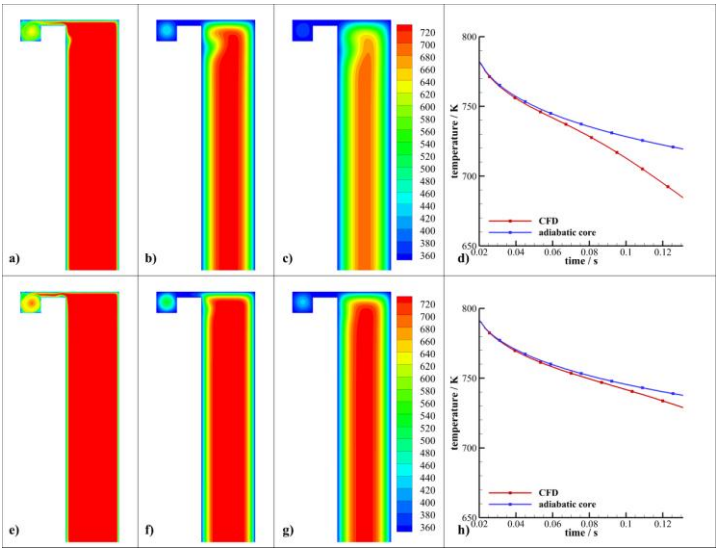

Figure 4.2– Temperature calculated from a CFD solution of the compression in the RCM used here showing the effects of a creviced piston. The time sequence is 0 ms, 50 ms and 100 ms after the TDC. The figures a-d are related with experiments at compression pressure of 2.75 bar. The sequence g-h is for compression pressure of 4.70 bar. Simulations for the RCM filled only with nitrogen. Adapted from (Werler et al., 2015).

4.1.3 Definition of Ignition Delay Time

The definition of the ignition delay time must be consistent to other measurements described in the literature. Even if the detailed design of different RCMs are not the same, the measured values of IDT should be quite similar (Bradley, Lawes, & Materego, 2015). Figure 4.3 presents the recorded pressure distribution of a typical experimental run of the ITT RCM.

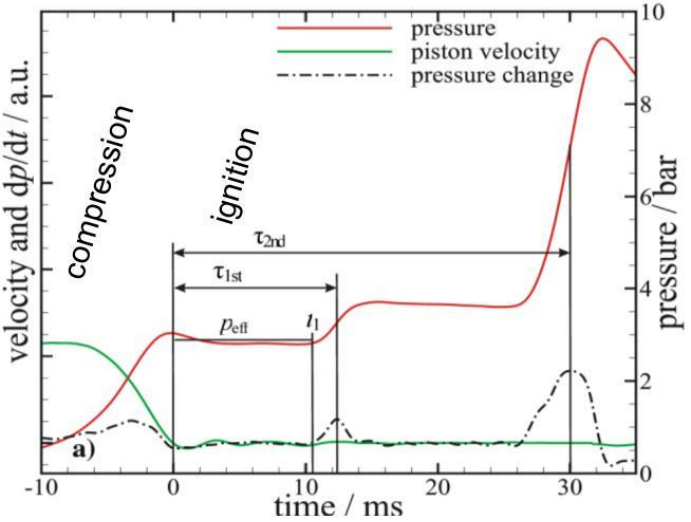

Figure 4.3–Pressure and piston velocity recorded profiles depicting a typical experimental run of the ITT RCM. Adapted from an internal technical report, contract FEESC-UFSC / ITT-KIT. Schiessl, R., 2015.

The time axis in Figure 4.3 starts at the instant t = -10 ms, after the compression stroke started. The instant t = 0 ms is the initial time reference for the calculation of the first IDT, τ_{1st}, the second IDT, τ_{2nd} and also, for the effective pressure p_{eff}. The instant t = 0 ms is defined using the graph of the piston velocity. When the piston velocity reaches zero, the piston is at TDC and the time is set to t = 0 ms. The p_{eff} is a time averaged pressure calculated by,

$$p_{eff} = \frac{1}{(t_1 - t_{TDC})} \int_{t_{TDC}}^{t_1} p dt \qquad (4.2)$$

where t_{TDC} corresponds to the time t = 0 ms in Figure 4.3, with the piston at TDC. The t_1 corresponds to the instant when the pressure starts to increase due the beginning of the combustion. This point is exactly defined by the first non-zero value of dp/dt in the region t > 0. dp/dt is also used to obtain the exact final points of the first and the second IDTs. The first dp/dt peak curve is used to define the end of the first IDT period. The second dp/dtpeak curve is used to define the end of

the second IDT period. The second IDT period is often also called the overall IDT.
The majority of the RCM reports present the ignition delay time, as a function of the initial temperature, pressure and fuel equivalence ratio. The graphs are normally presented as Arrhenius plots.

4.1.4 Mixture Preparation

Flammable mixtures between jet fuels and oxidants are hard to obtain, mainly due to the low volatility of the jet fuels. The composition characteristics of the jet fuels impose additional difficulties to obtain accurate relationships for its vapor pressure. As the Jet-A and Jet A-1 are standardized denomination that must be valid for all samples obtained from hundreds or even thousands of refineries around the world, it is not feasible to have an unique general curve or function to predict the jet fuels vapor pressure.
The common approach for the jet fuels mixture formation is to heat up a mixing chamber and then inject, normally using a syringe, the fuel into the vessel. The ideal gas and partial pressure laws are used in conjunction, to calculate the theoretical partial pressure of the injected jet fuel and oxidizer, the so called partial pressure method. Normally, the mass of the jet fuel is measured previously to injection into the mixing chamber, and this measured mass is used to calculate the theoretical jet fuel partial pressure, considering total vaporization. The last step is to compare the inner vessel measured pressure with the theoretical partial pressure calculated using the ideal gas equation.
(Subith S. Vasu et al., 2008) carried out experiments with Jet-A and JP-8/oxidizer mixtures in a heated shock tube. The covered temperature range was 715-1229 K, pressure in the range of 17 – 51 bar and equivalence ratio of 0.5 and 1.0. The flammable mixture was made using a heated mixing chamber with an inner volume of 12.5 l and working temperature of 125ºC. (Kumar & Sung, 2010) reported a similar approach to experiments conducted in a rapid compression machine, also using Jet-A and JP-8 as fuel.
The mixing chamber used in this study has an inner volume of ≅12.3 l. The heating system controller is commonly set up to 125ºC, or 130ºC. Before the fuel injection, vacuum is made, up to one militorr. The jet fuel is then injected and the partial pressure is monitored between 1 and 3 hours to check condensation and/or wall adsorption. In all of the valid experiments, the partial pressure of the injected Jet A-1 and the mixtures, remained stable for all the experimental period, indicating

total fuel vaporization and no further condensation and/or wall adsorption. The use of an inner magnetic stirrer guarantees a homogeneous mixture. The connections between the mixing chamber and the RCM were also heated and insulated, using the same material and control system as the mixing chamber.

4.2 Flame Ignition and Flammability Limits

The experiments for the determination of the flammability limits and flame propagation of premixed mixtures were carried out using two constant volume reactors, one at LABCET/UFSC-Brazil and the other at ITT/KIT-Germany. For simplicity the CVR installed at UFSC will be called Laminar CVR and the CVR installed at KIT will be named Turbulent CVR.

4.2.1 The Laminar CVR

The laminar CVR was designed and built at the Combustion and Thermal Engineering Laboratory – LABCET of the Federal University of Santa Catarina UFSC, Florianópolis-Brazil (Ricardo Morel Hartmann, 2009). It is a spherical reactor, casted in AISI 316 stainless steel, with an inner diameter of 300 mm. It is rated for maximum pressure of 350 bar. The reactor is equipped with a Kistler 6441 pressure transducer and a Schlieren Photography set up. The laminar CVR has two opposite quartz glass windows with 150mm of diameter, to provide the optical access to Schlieren measurements. (E. M. Hartmann, 2014) presents additional details on the pressure signal acquisition and treatment, the Schlieren set up and the control of the experiment. Figure 4.4 shows an exploded view of the laminar CVR.

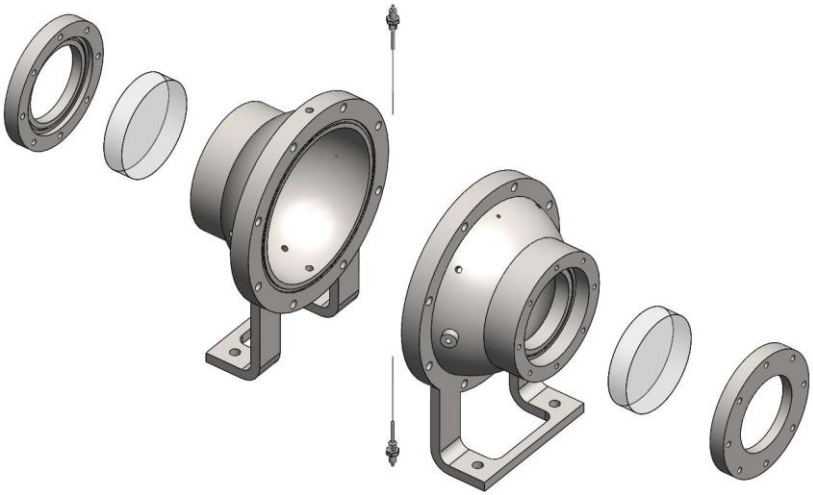

Figure 4.4– Laminar CVR exploded view.

4.2.2 The Turbulent CVR

The turbulent CVR is installed at the Institute of Technical Thermodynamics (ITT) of the Karlsruhe Institute of Technology (KIT), Karlsruhe/Germany. It is a large cylindrical constant volume bomb with volume of 55 liters and internal diameter of 40 cm, equipped with four radially symmetric fans for generation of turbulence. Measurements with Laser Doppler Anemometry (LDA) were previously performed in the vessel, providing a relationship between the low temperature turbulent field RMS velocity and the speed of the fans (Lindenmaier, 2002). The diameter of the fans is 14 cm and the range of the RMS velocity measured was up to 3.5 ms. The turbulent CVR has a front quartz glass windows with 100 mm of diameter and two side windows with 50 mm of diameter. One of the side windows is used to assess the ignition of the flame kernel using an ICCD-camera. The pressure is recorded using a Kistler 6061B, 5011B transducer. Figure 4.5 shows a picture of the turbulent CVR facility.

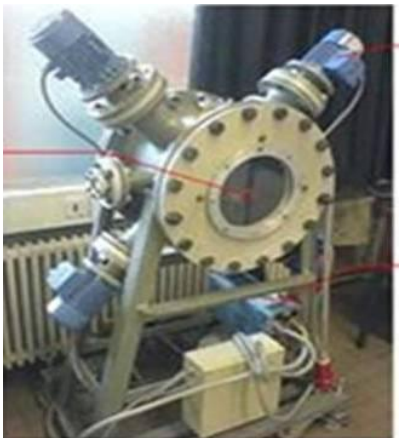

Figure 4.5– ITT/KIT turbulent CVR.

4.2.3 Method of Measurement of Flammability Limits

Following the statistical interpretation of ignition events, the flammability limits of fuel/air mixtures were measured using the laminar CVR. The data post processing method reported by (Bane, 2010) was employed. The spark energy was controlled and measured using a capacitive-inductive device specially designed for the laminar CVR. The device is described by (E. M. Hartmann, 2014). The fuel equivalence ratio was the stimulus variable, instead the spark energy as in the results reported by (Bane, 2010). Figure 4.6 shows results for a set methane/air experiments, for a fixed spark energy. The criterion to define the flame propagation was the pressure criterion, if the peak pressure after the spark was 5% higher than the initial pressure, a flame was propagated. Sometimes, Schlieren images were also used to confirm the result of the experiments.

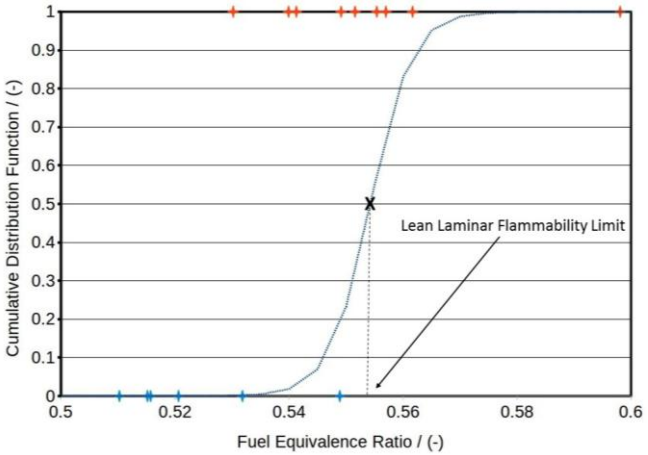

Figure 4.6– Probability cumulative logistic functions P(x) of a laminar mixture between methane and synthetic air at 300 K and 1 bar. The horizontal axis is the fuel equivalence ratio (phi), the red crosses are flammable mixtures and the blue ones are not flammable. There were carried out 15 experiments to build the curves.

It is interesting to note that the inclination of the central blue curve is quite noticeable. This inclination is proportional to the experimental scatter, i. e., the overlapping region between flammable and no flammable mixtures. It could be due the low quantity of experiments, 15, instead 25 as suggested by (Bane, 2010). The flammability limit is defined as the fuel equivalence ratio that crosses the probability curve for a CDF of 0.5.

4.2.4 Flame Kernel Extinction Limits of Turbulent Premixed Mixtures

The methodology here is similar as used for determination of the laminar flammability limits, but using the turbulent CVR. Firstly, the lean flammability limit for laminar condition was measured. The ignition was made using a commercial Bosch automotive coil, controlled by a Labview code. The spark voltage and current were measured using a Tektonix Voltage probe and a Hameg current probe. The criterion to define the flame propagation was the pressure criterion, if the peak pressure after the spark was 5% higher than the initial pressure, a flame was propagated.
The next step was to evaluate the effect of turbulence. Using the same

spark energy, the turbulent RMS velocity was increased. The criterion to detect the successful event, was modified. The concern now is the flame kernel extinction caused by the turbulence.

The methodology to detect extinction is based on the optical assessment of the flame kernel. Using an ICCD camera installed at the turbulent CVR facility, it is possible to detect the luminosity of the flame kernel and the luminosity of the spark. Figures 3.7 (a), (b) and (c) show a picture sequence of the luminosity from the spark plasma channel, captured by the ICCD camera. The picture were taken for the turbulent CVR filled only with synthetic air (20% O2 and 80% N2). The pictures were taken 3.1 ms, 3.7 ms and 4.1 ms after the spark trigger. The synchronization between the trigger and the spark was electronically made, using the Davis Imaging Pro, provided by the ICCD camera company. The Davis Imaging Pro and the turbulent CVR controlling software Labview-based were wired through the spark trigger signal cable.

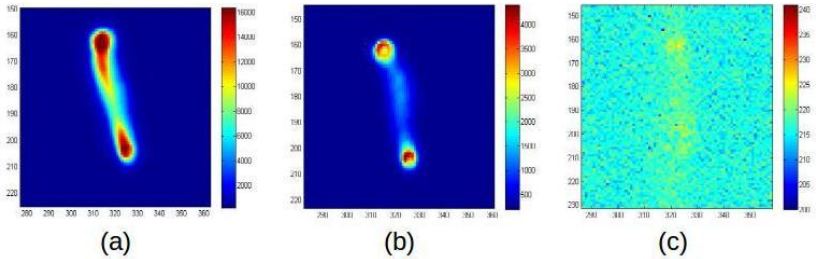

Figure 4.7– Pictures of the spark plasma channel using the ICCD camera installed at the turbulent CVR. The pictures were taken for the turbulent CVR filled only with synthetic air. The time sequence is: picture (a) 3.1 ms; picture (b) 3.7 ms and picture (c) 4.1 ms after the spark trigger. Laminar flow. The color scale in the right sides are related with the light intensity measured by the camera, in arbitrary units.

It is possible to infer that after 4.1 ms the luminosity from the spark has vanished. Thus, for a mixture with air and any fuel of interest, any luminosity captured after 4.1 ms represents a flame kernel ignited by the spark. Figure 4.8 and Figure 4.9 show two examples of ethanol-air flame kernels, captured by the ICCD camera. The initial conditions were quite similar, with a slight difference for the equivalence ratios 0.79 and 0.76 respectively. Figure 4.8 depicts a kernel that did evolve to a flame propagation. Figure 4.9 depicts a kernel that did not evolve to a flame propagation. This flame kernel was thus extinguished by the turbulent

field. The criterion to define the flame propagation was again the pressure criterion: when the peak pressure after the spark was 5% higher than the initial pressure, a flame is considered to have successfully propagated. Conversely, when a flame kernel is detected by the ICCD camera, but no flame propagation was detected by the pressure criterion, a flame kernel is assumed to have suffered extinguishment.

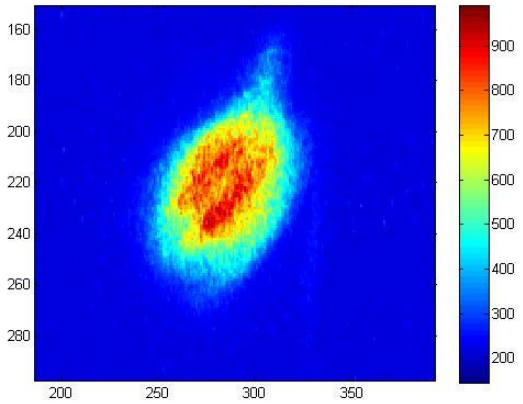

Figure 4.8– Ethanol-air turbulent flame kernel, phi = 0.79, Ti = 300 K, pi = 1 bar, turbulence RMS velocity = 3.5 m/s. Picture 4.2 ms after the spark trigger. There was a flame propagation.

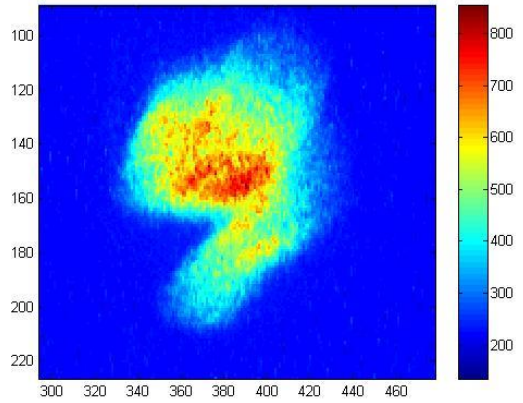

Figure 4.9–Ethanol-air turbulent flame kernel, phi = 0.76, Ti = 300 K, pi = 1 bar, turbulence RMS velocity = 3.5 m/s. Picture 4.2 ms after the spark trigger. There was **no** flame propagation.

The inspection of Figure 4.9 reveals the flame geometry was strongly perturbed by the turbulence. Considering the application in jet engines, Figure 4.10 shows the extinction limits curves for methane and ethanol. The plot was made using the turbulent field RMS velocity as function of the fuel/air equivalence ratio. The gray shadow around both curves represents an uncertainty estimation due mainly the uncertainties induced by the presence of the turbulent field.

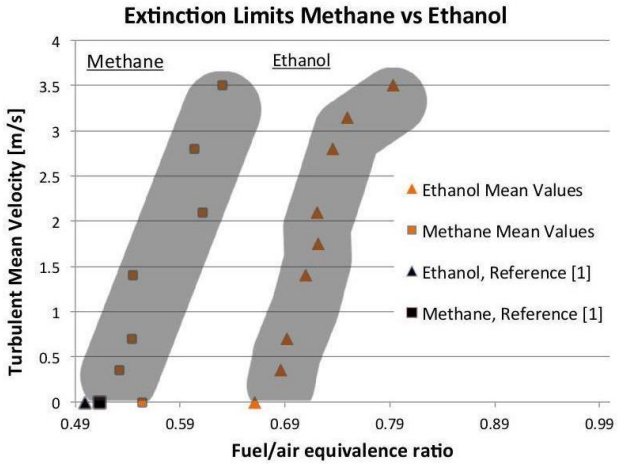

Figure 4.10–Extinction limit curves of methane and ethanol-air premixed mixtures at 305 K and 1 bar. The reference 1 is (Zabetakis, 1965). Adapted from (R. M Hartmann, Schiessl, Oliveira, & Maas, 2014).

These measurements are not directly comparable to the laminar flammability measurements. The flammability limit, as briefly discussed in section 3.1, is mostly related to the capacity of the mixture to provide enough thermal energy for the propagation of the flame kernel. The turbulent extinction limit, depicted by Figure 4.10, is related to the effect of the flow in stretching, diluting and cooling a flammable mixture previously ignited.

The main goal of the Figure 4.10 is to provide a basis to further predictions of the flame extinction behavior of fuel-air mixtures under turbulent conditions. For the both fuels analyzed, methane and ethanol, it is possible to see that the turbulent fields pushes the extinction limits to the richer side, i.e., to higher equivalence ratios, thus becoming a hampering effect to flame propagation.

4.3 Flame Propagation

The laminar CVR used in this work was described in (E. M. Hartmann, 2014). The laminar CVR has a heating system capable to heat it up 140ºC. Before the experiments, the CVR was heated and stabilized at 135ºC, 10ºC higher compared with the RCM experiments. For each shot, the reactor was vacuumed down to 0.01 militorr. The fuel was then injected and flash vaporized. The fuel mass is measured using a very sensitive weight machine (Shimadzu, uncertainty 10E-4 mg). The air mass is measured using the partial pressure method. The overall uncertainty related with the laminar flame speed is about 0.5 cm/s, while for the flame thickness the uncertainty is 0.01 mm. Section 4.5 brings an introductory report about the laminar CVR experimental uncertainties.

4.3.1 Pressure Trace Inputs in the CVR Experiments

The CVR method was originally developed almost a century ago to assess the propensity for accidents in mines (Hopkinson, 1906). When some flammable mixture is confined in a CVR, and properly ignited, a spherical flame propagates towards the unburnt reactants. As the flame consumes the reactants a measurable flame profile evolves with the time. A careful record of this pressure profile allows to assess the speed of the flame propagation (Andrews & Bradley, 1972; Bernard Lewis, 1961; Metghalchi & Keck, 1982; Poinsot & Veynante, 2005; Rahim, Eisazadeh-Far, Parsinejad, Andrews, & Metghalchi, 2008; Williams, 1986; Zabetakis, 1965).
(Zabetakis, 1965) carried out experiments using a cylindrical CVR with 19.7 cm diameter and 9 liter inner volume. Experiments for central ignited stoichiometric air methane flames were reported. Figure 4.11 shows the measured pressure versus time. After a slow increase in pressure during the first few milliseconds, the pressure curve presents a rapid increase. Finally, the flame reaches the walls of the reactor and suffers quenching.

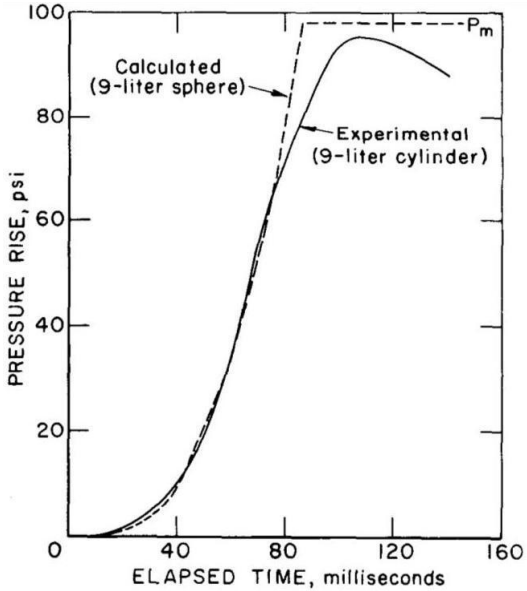

Figure 4.11– Pressure profiles for the central ignited stoichiometric methane-air mixtures, using a cylindrical vessel with 19.7 cm diameter and 9 liter inner volume. The calculated profile was done using the equation 4.3 with the constant K evaluated at time = 75 ms. Adapted from (Zabetakis, 1965).

(Zabetakis, 1965) used a very simple thermodynamic model to describe the pressure increase due to flame propagation,

$$\Delta p = K p_i \frac{S_L^3 t^3}{V} \tag{4.3}$$

where Δp is the pressure increase during the combustion, K is a proportionality constant, p_i is the initial pressure, S_L is the burning velocity, t is the time and V is the vessel volume.

Figure 4.11 also presents the prediction of equation 4.3 (curve named "calculated"). The calculated and measured profiles match quite well until approximately t = 80 ms. After that, quenching and heat loss become important.

Because of its simplicity, equation 4.3 is useful for a quick analysis of the measurements from the CVR. In principle, the proportionality constant K, the initial pressure pi and the vessel volume V are constants. Additionally, at a first guess, the burning velocity could also be

considered constant for some intervals. Then, equation 4.3 becomes a simple cubic equation for pressure versus time, allowing to estimate the flame speed.

(Metghalchi & Keck, 1982) presented a more complete model to calculate the burning velocity that takes into account the variation of flame speed along flame propagation. The model is based on volume conservation only. The proposed approach considers the reactants and products as ideal gases, the burnt gases at chemical equilibrium and the pressure is assumed uniform in the reactor. The flame sheet is considered spherical, smooth and with an infinitesimal thickness. As the inner pressure increases with the time, the model considers also the isentropic compression of the burned and unburned gases. The conservation of volume states that,

$$v_i = \int_0^x v_b\,dx + \int_x^1 v_u\,dx \tag{4.4}$$

where v_i is the initial specific volume, v_b is the specific volume of the burned gases, v_u is the specific volume of the unburned gases and x is the mass fraction of the burned gases.

After manipulating the conservation of volume and using the kinematic definition of flame speed, they arrived at,

$$S_b = \frac{\rho_i}{\rho_u}\left(\frac{V_c}{V_f}\right)^{(2/3)} \frac{r_c}{3}\left(\frac{dx}{dp}\right)\frac{dp}{dt} \tag{4.5}$$

where ρ_i is the initial density, ρ_u is the unburned gas density, V_c is the inner chamber volume, V_f is the volume occupied by the burnt gases and r_c is the radius of the vessel and S_b is the burning velocity. Equation 4.5 is a single analytical solution that provides the burning velocity as function of the pressure profile and consequently as function of time. One of the drawbacks is the need to obtain accurate functions dx/dp and dp/dt from the measurements.

(Rahim et al., 2008) presented an updated thermodynamic model. Their model considers both the conservation of volume and internal energy. Using the mass conservation equation in terms of mass fraction, the conservations of internal energy and internal vessel volume become,

$$u_i = u_b x_b + u_{flame}\, x_{flame} + u_u\left(1 - x_{flame} - x_b\right) - e_{transf} \qquad (4.6)$$

$$v_i = v_b x_b + v_{flame}\, x_{flame} + v_u\left(1 - x_{flame} - x_b\right) - v_{layers} \qquad (4.7)$$

where u is the internal energy and the subscripts u and b mean unburned and burned mixtures. The e_{transf} term embodies all the flame energy transfer and dissipation: the heat transfers to the ignition electrodes, to the reactor walls through convection, radiation and conduction, the energy dissipation related with the compression work done on the boundary layers of the flame front and reactor walls. The term v_{layers} in equation 4.7 is related with the displacement of the boundary layers. For a detailed description of equations 4.6 and 4.7 the reader should refer to (Rahim et al., 2008).

Using the experimental pressure profile as input data in addition with the ideal gas equation, the system of equations can be solved using a Newton-Raphson algorithm. The solution of equations 4.6 and 4.7 provides flame temperature and burned mass fraction as function of time. Thus, the burning velocity can readily be calculated using the equation 4.8,

$$V_B = \frac{\dot{m_{burned}}}{\rho_{reactants}\, A_{flame}} = \frac{m_i \dot{x}}{\rho_{reactants}\, A_{flame}} \qquad (4.8)$$

where m_i is the initial mixture mass inside of the reactor and $\dot{x}$ is the rate of the burned gases mass fraction. It is important to note that equation 4.8 yields the instantaneous value of the burning velocity and this value is affected by the flame stretch. Additional attention must be paid to the energy transfer terms, whose magnitude can also affect the results of equation 4.8. A key concern when one works with the pressure input method is, of course, the quality of the pressure signal.

4.3.2 Optical Measurements of the Flame Propagation in CVR Experiments

The optical methods are based on the image recording of the flame propagation. One of the more common optical methods used for the high speed photography of flames is the Schlieren Method.
The basic set-up for the Schlieren method consists of a punctual light source, mirrors and/or lenses and a high speed camera. The method takes advantage from the gradient of the refractive index in a flow, induced by temperature gradient. For a comprehensive description on the physics and application of the Schilieren method the reader should refer to (Settles, 2001).
The Schlieren setup used was the "Z" type. This setup was selected due to its intrinsic low optical aberrations (E. M. Hartmann, 2014; Settles, 2001). Figure 4.12 shows a schematic of a Z type Schlieren setup. Figure 4.13 shows a simplified flowchart of the Schlieren setup as described by (E. M. Hartmann, 2014).

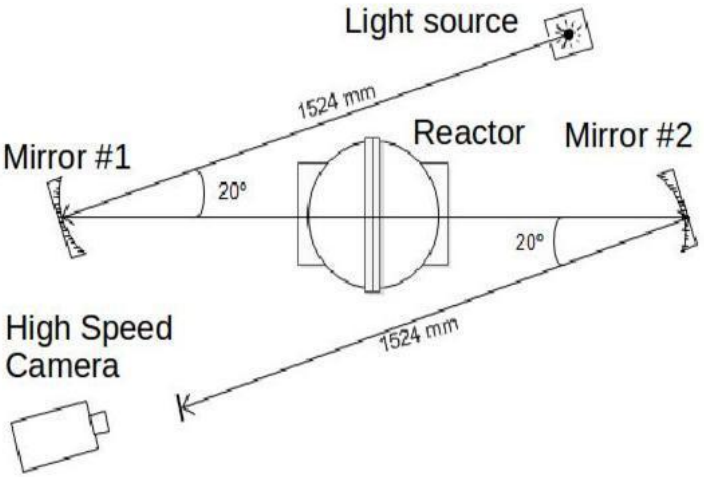

Figure 4.12– Schematic of the Z type Schlieren setup installed at LAB-CET/UFSC. Adapted from (E. M. Hartmann, 2014).

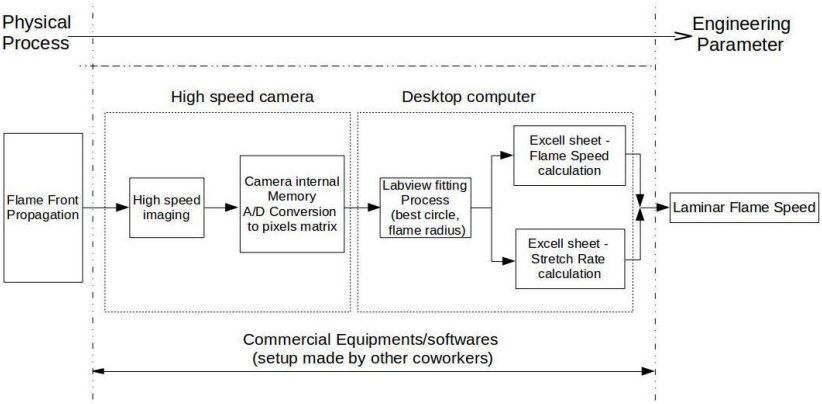

Figure 4.13– Simplified flowchart Schlieren setup described by (E. M. Hartmann, 2014).

From the images recorded, a flame radius versus time profile is obtained. Figure 4.14 shows an example of the flame propagation of an air-methane mixture at equivalence ratio 0.8, Ti = 300 K and pi = 1 bar.

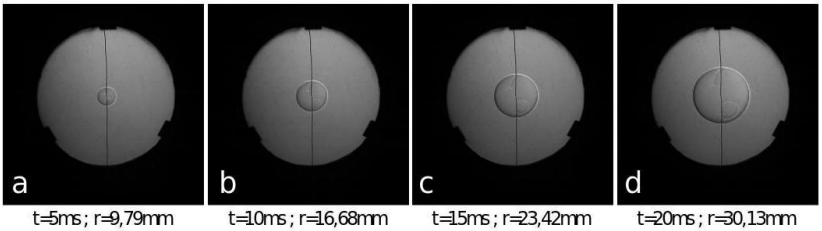

Figure 4.14– Pictures of a flame propagation process. Air-methane mixture at phi = 0.8, Ti = 300 and pi = 1bar. It is showed also the respective time and radius values for each picture. Acquisition rate = 10 kHz, spatial resolution 256 x 256 pixels. Adapted from (E. M. Hartmann, 2014).

The image analysis was performed using the Labview image treatment package. Shortly speaking, the image algorithm calculates a best fit circle, based on the brightness distribution of the image pixel matrix. Figure 4.15 shows the Figure 4.14-d, when the image was been treated using the Labview image post-processing code. It is possible to identify three main circles: the green one is the optical outer reference diameter, the blue is an auxiliary virtual circle and the red circle, inside of the yellow annular region, is the best fitted circle calculated by the Labview code. The flame radius is then obtained as being the radius of the red circle.

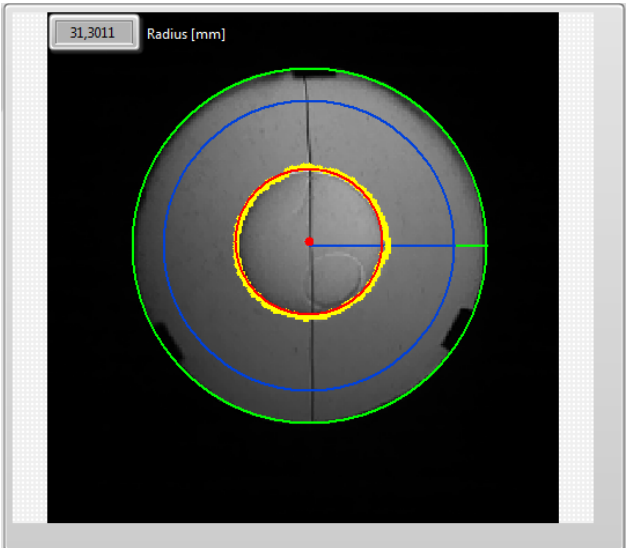

Figure 4.15– Labview image post-processing applied to the Schlieren photography setup. This figure shows figure 4.14-d under imaging processing. Adapted from (E. M. Hartmann, 2014).

The majority of the flame pictures resemble the one shown in Figure 4.15. The yellow annular region is clearly thicker compared with the red circle. The fitting process applied to the Schlieren images brings uncertainties related to the flame thermal thickness and with the image pixels brightness distribution. The boundary of the red circle detects the region where the temperature gradient is maximum. Taking a value of 40 cm/s for the laminar flame speed and a mean thermal diffusivity of 10E-05 m^2/s results in a thermal flame thickness in the order of 0.1 mm. Therefore, there is an initial uncertainty in flame radius of this order of magnitude. (E. M. Hartmann, 2014) evaluated the effect of blurring caused by low pixel resolution and reported an uncertainty of 0.5 mm in the radius calculation, when using a fast camera set to 256x256 pixels of resolution and 10,000 fps (frames per second) of acquisition rate. We can conclude that the main source of uncertainty is the pixel resolution and a resolution larger than 256x256 pixels is required for lower uncertainty.

4.4 Calculation of Burning Rates

This section describes the post processing FORTRAN code applied to measurements obtained with the laminar CVR. The code is called *CVR Flame Code*. Basically, the model calculates the burned gases mass fraction as function of the reactor pressure time profile. It starts with the discretization of the gas volume into a number of layers. The model is based on an implementation of the conservation of mass and volume within the reactor. Additionally, the burned fraction is considered in equilibrium. The NASA CEA (Chemical Equilibrium with Applications) code (McBride, 1994) is used to (1) provide thermodynamic properties of the gas mixtures, i. e. of the burned and unburned gases mixtures inside of the CVR, (2) calculate the equilibrium state of the burned gases, considering stable species and radicals involved in flame propagation and, (3) to calculate the temperature of the burned gases considering constant pressure or constant volume process.
The CEA NASA is also used to estimate the final conditions for a global constant volume combustion of the reactant mixture within the CVR. As an example, Table 4.2 summarizes such results for a stoichiometric methane/air mixture, considering no products dissociation case and with dissociation. Two conditions are considered, one for a combustion to saturated products, CO_2, N_2, and H_2O, and the other assuming a more complete list of products, CO_2, N_2, H_2, H_2O, CO, NO, N_2O, NO_2, OH and O_2.

Table 4.2–Theoretical results for a stoichiometric air-methane mixture. The "i' letter means initial, the "f" letter means final.

Process	Saturated combustion products: CO_2, N_2, and H_2O	More complete list: CO_2, N_2, H_2, H_2O, CO, NO, N_2O, NO_2, OH and O_2
phi	1	1
Ti, K	300	300
pi, bar	1	1
Tf, K	2,811.47	2,606.49
pf, bar	9.4952	8.9114
sf, kJ/kg-K	9.4818	9.4979

The higher value of entropy achieved for the more complete list indicates that this condition is thermodynamically more stable, as expected.

4.4.1 Thermodynamic Model

The CVR Flame code was based on previous works of (Andrews & Bradley, 1972; Metghalchi & Keck, 1982; Rahim et al., 2008). It is based on three main simplifying assumptions: (1) ideal gas, (2) the flame is spherical and the flame front is smooth and (3) the burned gases are in mechanical and chemical equilibrium.
The volume conservation equation, for the inner reactor volume is expressed as,

$$V_i = V_b + V_u \tag{4.9}$$

where V_i is the initial reactor volume, V_b is the burned gases volume and V_u is the unburned gases volume. Writing the Equation 4.9 in terms of the specific volume,

$$v_i m_i = v_b m_b + v_u m_u \tag{4.10}$$

where m is the respective mass and v is the specific volume. Dividing the equation 4.10 by the initial mass m_i,

$$v_i = v_b x_b + v_u x_u \tag{4.11}$$

where x is the respective mass fraction.
Applying the mass conservation condition and considering the burned gases are comprised of n-1 burned shells, it follows that,

$$v_i = \sum_{j=1}^{n-1}\left(v_j x_j\right) + v_n x_n + v_u\left(1 - x_n - \sum_{j=1}^{n-1}\left(x_j\right)\right) \tag{4.12}$$

where n is the actual time steps and indicates the actual burning layer or, the flame sheet. Figure 4.16 shows the sketch of the multi zone model employed, showing the burned gas layers, the actual burning layer n (the flame sheet) and the unburned gases.

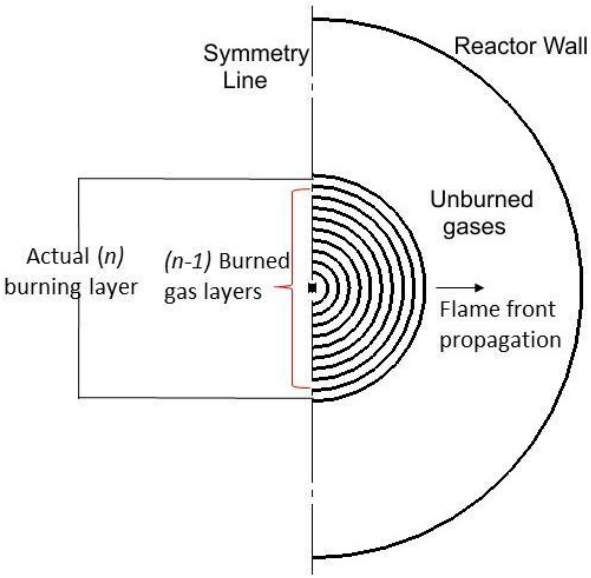

Figure 4.16– Sketch of the burned gas layer, actual burning layer (the flame sheet) and the unburned gases.

Each burned shell is submitted to an isentropic compression related to the previous time step (n-1). Similar isentropic compression holds for the unburned gas region. So, using the pressure from the experiments, the temperatures obtained from the isentropic compression calculations and knowing the flame sheet temperature obtained from the constant pressure combustion calculation using the CEA code, it is possible to solve the equation 4.12 applying the Newton-Raphson method. The Newton-Raphson method is stable and fast converging for monotonic functions. This is the case of the equation 4.12, making the Flame Code numerically stable and reliable (Ricardo Morel Hartmann, 2009).
The result provided by Newton-Raphson method is the burned mass fraction x_n. Using it, all of the flame characteristic of interest are then obtained: the flame radius is calculated using the equation 4.13, the burning velocity using the equation 4.8 and the thermal flame thickness using the equation 3.6.

$$r_{flame} = \left[\frac{3}{4\pi} m_i \left(x_n v_n + \sum_{1}^{n-1} (x_k v_k)\right)\right]^{1/3} \qquad (4.13)$$

The algorithm can be summarized as follows:

1. At the time step $t = 1$, or $n = 1$ in the equation 4.12, the first portion of fuel mixture is burned by the spark. The reactor is divided then in two regions: a very small burned gas region and an unburned gas region. The pressure is uniform and equal to $p(1)$;

2. As the flame propagates, a news layer n of the reactants is burned. This burning layer will expand, as its combustion is occurring at constant pressure $p(n)$ and constant enthalpy. The constant pressure combustion is based on the fact that, the characteristic combustion time has the same magnitude of the sound speed characteristic time in the unburned gases. After the end of the constant pressure combustion of the current burning layer, the expansion wave generated by this layer travels to and reaches the reactor walls. Then the reflected pressure wave propagates back towards the center of the reactor, thus equalizing pressure through the entire volume to a new $p(n + 1)$ value. The system burned gases + burned layer + unburned gases come then to a new state of equilibrium;

3. The step 2 is repeated until all the reactants are consumed.

The use of a constant pressure combustion for each layer followed by the compression and expansion of the unburned and burned regions is an acceptable simplification since the reactor is divided in small layers and each layer burns during a small fraction of the total combustion time. For example, for a stoichiometric mixture between methane and dry air at 1 bar and 300 K, the volumetric reaction rate $\acute{\omega}$ is estimated as 8.04E+04 kg/m³-s (Glassman & Yetter, 2008). Considering an initial inner flame radius of 10 mm, a flame thickness of 0.5 mm, a burned mass fraction of 0.001 and an initial reactor mass of 0.01818 kg, the characteristics burning time for such burning flame layer is 0.34 ms, a small fraction of the total time. The combustion of each layer can also be described as a thermodynamic cycle. The state 1 corresponds to the unburned gases at time t(n-1). A portion of this unburned gases is wrapped by the moving flame. The thermodynamic processes that follow are:

- Process 1 -> 2: Isentropic compression of the unburned gas. Temperature changes from $T(n - 1)$ to $T(n)$through a pressure variation from $p(n - 1)$ to $p(n)$, caused by the compression

wave generated during the combustion of the previous burned layer $(n-1)$;

- Process 2 -> 3: Heat addition at constant pressure, due to the combustion of the current layer;
- Process 3 -> 4: Isentropic compression of the layer that has been just burned. The temperature changes from $T(n)$ to $T(n+1)$ through a pressure difference between $p(n)$ and $p(n+1)$.

In the next step of the flame propagation, the processes are repeated, considering the actual pressures *p(n)* and *p(n+1)* as the inputs for the following cycle. Figure 4.17 depicts a *p-v* diagram and Figure 4.18 a T-s diagram of the idealized CVR flame cycle.

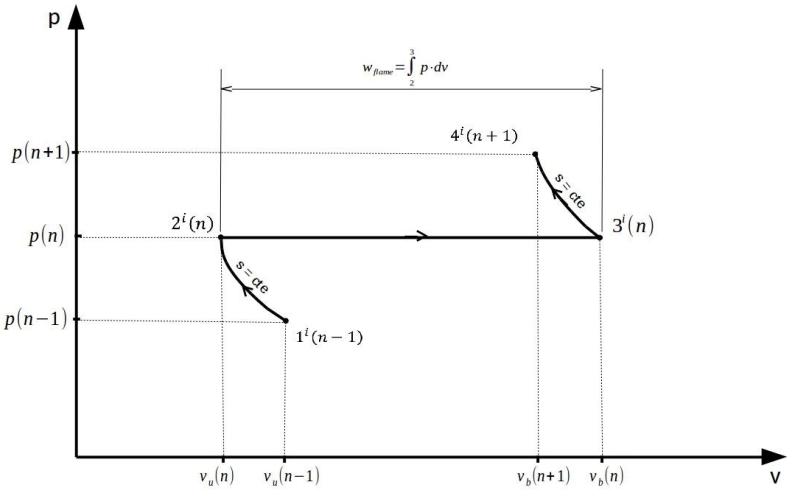

Figure 4.17–p-v diagram of the idealized CVR Flame Cycle. The axis are not scaled.

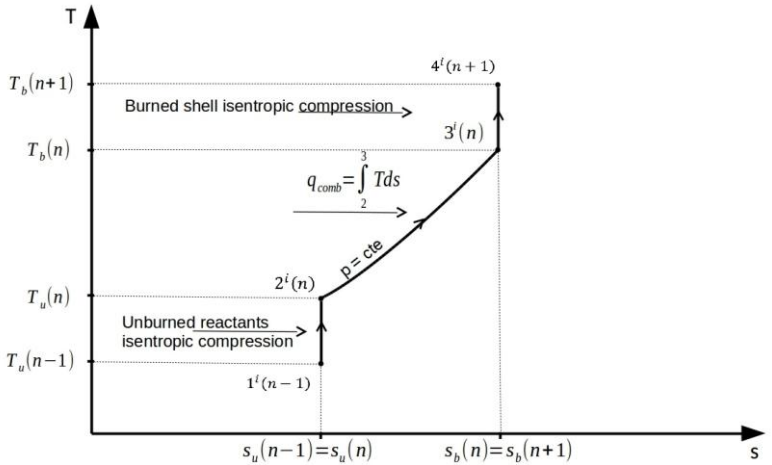

Figure 4.18– T-s diagram of the idealized CVR Flame Cycle. The axis are not scaled.

The actual flame propagation is also affected by heat losses. There are radiation losses from the flame to the walls and heat conduction as the flame approaches the walls. Also, the thermal and mass diffusion that occurs across the flame front affects the reaction rates and the products formed are not only CO_2 and H_2O, causing a departure from the equilibrium conditions computed by NASA CEA. To fully account for these effects, direct numerical calculation is needed, as performed by (Bonhomme, Selle, & Poinsot, 2013). As a result of these irreversibilities, process 2->3 is changed and 3->4 is no longer an isentropic compression. One interesting and useful aspect of the Flame Code is that the main input to the calculations is the measured pressure profile. This experimental pressure is a real process pressure profile and already carries "informations" of all energy dissipations that eventually occurred during flame propagation. The full algorithm can be found in Appendix II. In the ensuing section, the treatment of the pressure-time curve is described.

4.4.2 Pressure Signal Pre-treatment

The pressure signal presents fluctuations which are typical of dynamical measurement systems. Even though the hardware does some filtering of the input signal, since the burning velocity data treatment relies on calculation of time derivatives, additional smoothing is needed.
During the experiments, the pressure data of interest is synchronized

with the spark, using a spark current probe. The end of the recorded data is determined by the peak pressure. As an example, Figure 4.19 shows the experimental pressure time evolution for three mixtures of methane, iso-octane and Jet A-1 with air. The curves indicate that, for the same initial conditions, this mixture of iso-octane burns faster than methane. The curve for kerosene was obtained at higher initial temperature.

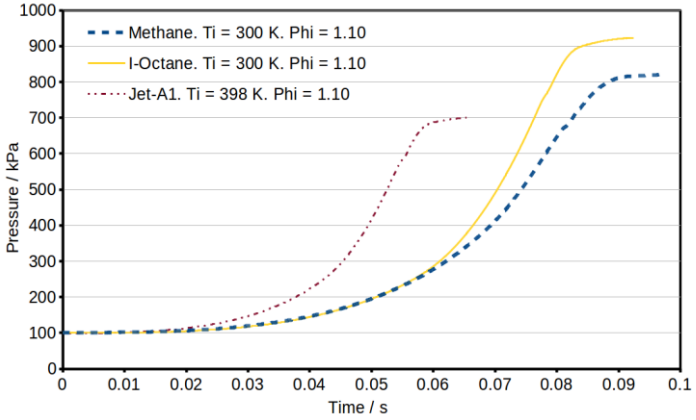

Figure 4.19– Experimental pressure profiles of three mixtures of methane, iso-octane and Jet A-1 with air, obtained using the laminar CVR. The acquisition rate is 10 kHz. Initial pressure of 1 bar.

Figure 4.20 presents a zoom of the data points of the Figure 4.19 for the time interval from 0 to 20 ms.

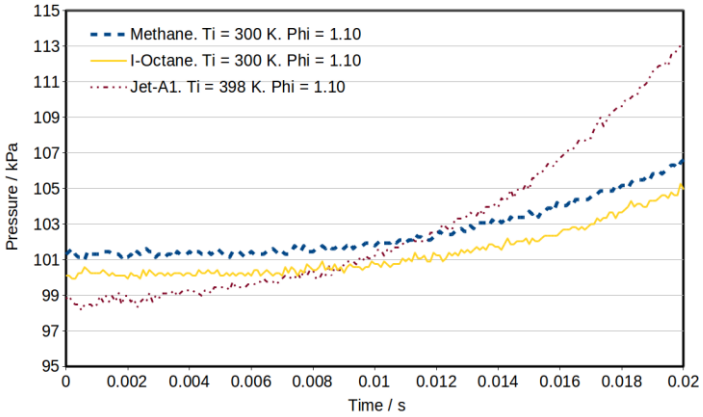

Figure 4.20–Experimental pressure profiles for three mixtures of methane, iso-octane and Jet A-1 with air, obtained using the laminar CVR. The graph zooms the initial instants of the flame propagation. The acquisition rate is 10 kHz. Initial pressure of 1 bar.

Since the data still present fluctuations, which would cause oscillations in the calculation of the time derivatives, the algorithm applies a smoothing technique. The first filter applied was a simple mean calculation. The original experimental points were grouped. The size of each data set is called the discretization number. For the majority of the experiments carried out, the discretization number was between 6 and 10. This first filter is here called Simple Mean Filter. The second filter uses the profile calculated by the Simple Mean Filter and applies a least square fitting method, resulting in a 5th degree polynomial. These two filters resulted in the best signal smoothing when compared to other methodologies. Figure 4.21 shows the initial portion of the pressure measurements for a mixture of Jet A-1 and air. Three pressure profiles are shown, the untreated measurements, the data treated using the simple mean filter and the curve-fitted 5th degree polynomial.

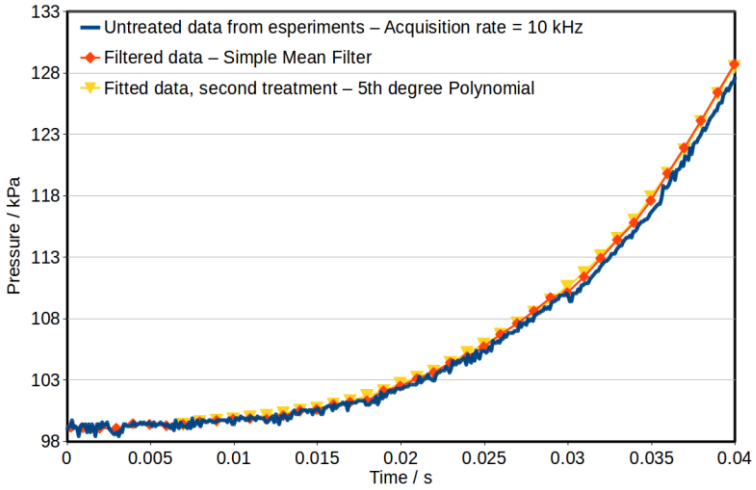

Figure 4.21–Comparison among representative pressure profiles: the untreated and two filtered profiles are shown. Jet A-1/air mixture, phi = 1.10, at 398 K and 1 bar.

The simple mean is able to filter high frequency oscillations, but misses the low frequency. For example, at 0.018 s, the measured data set shifts

laterally in time. The pressure calculated using the simple mean filter follows this shift. At 0.03 s, a similar shift also occurs. Again, the simple mean filter follows this shift, which would cause an abrupt variation of the time derivatives. The polynomial curve-fit, on the other hand, is smoother and monotonically increasing, thus the time derivative also varies monotonically as the physics of the problem suggests.
Another aspect considered in the data treatment is that, initially, the variation of pressure is very small. This is an important aspect that difficult the burning velocity calculation. These small variations may result in even slight negative time derivatives. In order to avoid the calculation of negative burning velocities, the Flame Code starts the calculation only after a stably increasing pressure slope is detected.

4.4.3 Comparison of the CVR Flame Code Results

The CVR Flame Code was tested using measurements for methane, n-heptane and isooctane. Initially, the conditions that result in a spherical and smooth flame are analyzed. Then, the flame code is used to predict the flame radius from the transient pressure curve and the results are compared to the optically measured flame radius. Then, the flame speed derived from the pressure curve is compared to data from the literature for the same fuels at the same initial conditions.

4.4.3.1 Assessment of the Flame Sphericity and Smoothness

Figure 4.22, Figure 4.23 and Figure 4.24 present a sequence of pictures for methane, n-heptane and isooctane air mixtures, respectively, taken by a Schlieren method when the flame radius was 50 mm. The equivalence ratios range from lean to rich mixtures.

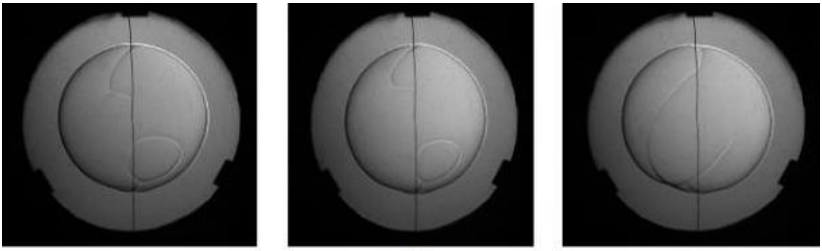

Figure 4.22– Schlieren pictures of methane-air mixtures. The acquisition rate is 10 kHz, the image pixels matrix is 256 x 256. The picture (a) is phi = 0.81, the picture (b) is phi = 1.0 and the picture (c) is phi = 1.29. All the experiments had initial temperature and pressure of 300 K and 1 bar.

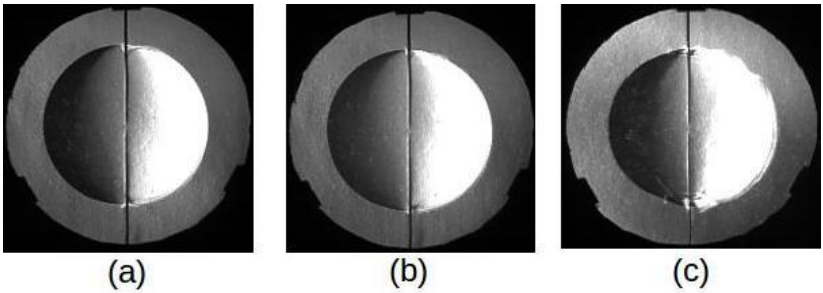

Figure 4.23– Schlieren pictures of n-heptane-air mixtures. The acquisition rate is 10 kHz, the image pixels matrix is 256 x 256. The picture (a) is phi = 0.80, the picture (b) is phi = 1.0 and the picture (c) is phi = 1.30. All the experiments had initial temperature and pressure of 300 K and 1 bar.

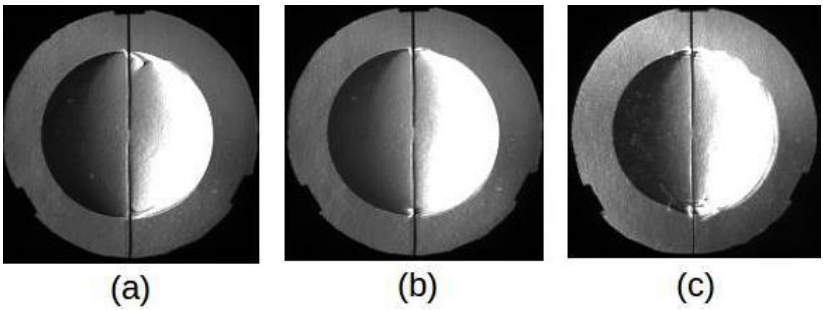

Figure 4.24– Schlieren pictures of n-heptane-air mixtures. The acquisition rate is 10 kHz, the image pixels matrix is 256 x 256. The picture (a) is phi = 0.79, the picture (b) is phi = 1.02 and the picture (c) is phi = 1.31. All the experiments had initial temperature and pressure of 300 K and 1 bar.

Comparing Figure 4.22, Figure 4.23 and Figure 4.24 it is possible to infer that the flames were spherical, symmetrical, and smooth in all the cases. It should be noticed that there was some wrinkling, mainly for the rich flames, due to flame-electrode interactions. These irregularities affect a very small portion of the total flame surface and, therefore, have a negligible effect. Figure 4.25 shows a sequence of pictures for hydrogen-air mixtures, using the same Schlieren system. Due to the different flammability limits for hydrogen, the range of equivalence

ratio is slightly different.

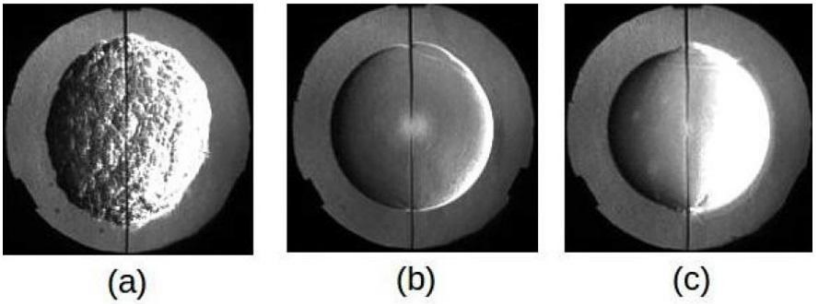

Figure 4.25– Schlieren pictures of hydrogen-air mixtures. The acquisition rate as 10 kHz, the image pixels matrix is 256 x 256. The picture (a) is phi = 0.50, the picture (b) is phi = 1.00 and the picture (c) is phi = 1.50. All the experiments had initial temperature and pressure of 300 K and 1 bar.

Figure 4.25(a) presents a high degree of wrinkling, which are typical of this lean hydrogen flame. The measurements here will not cover conditions that lead to wrinkling.

4.4.3.2 Comparisons of the Flame Radius Profiles

Figure 4.26, Figure 4.27 and Figure 4.28 show the comparison between the flame radius measured using the laminar CVR Schlieren setup and the flame radius calculated by the CVR Flame Code, for mixtures of methane, n-heptane and isooctane with air, respectively. Due to the limited size of the quartz glass windows for optical access in the laminar CVR, it is possible to perform Schlieren photography for radius up to approximately 60 mm. The uncertainty related with the flame radius measured by the Schlieren method for this experiment was reported by (E. M. Hartmann, 2014) as about 0.5 mm. The analysis of the three figures indicates a good agreement between the results from the flame code and those measured by Schlieren, with a maximum discrepancy of about 3% at the beginning of the pressure rise.

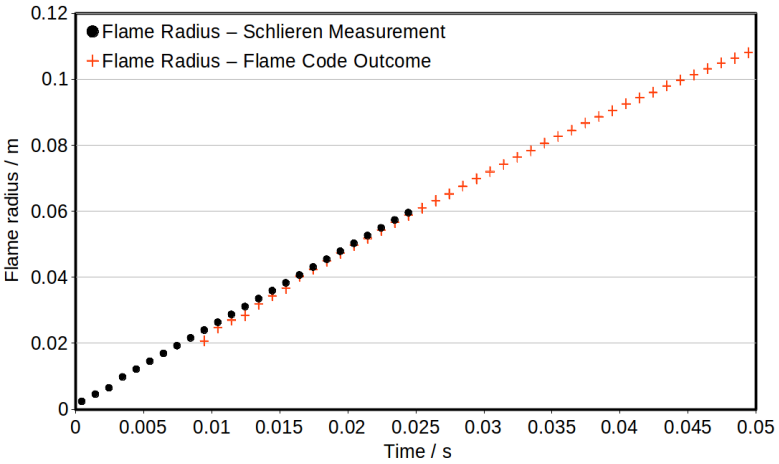

Figure 4.26–Flame radius measured using the laminar CVR Schlieren setup and the Flame Code. Stoichiometric mixture between methane and air at 300 K and 1 bar.

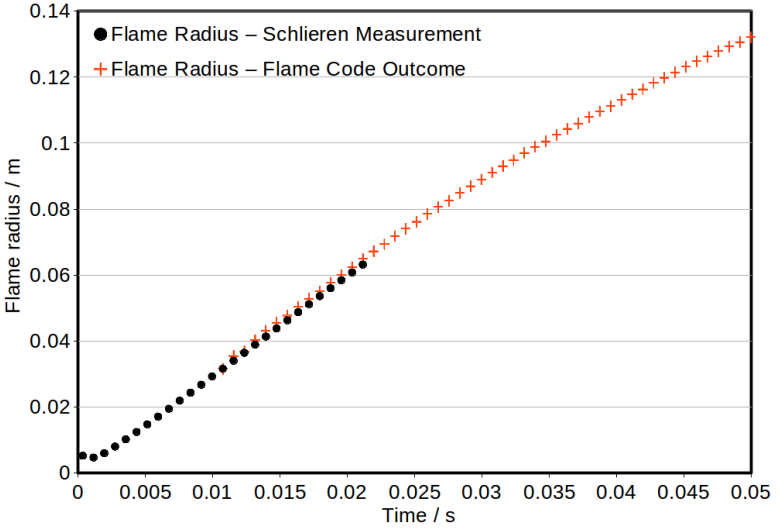

Figure 4.27–Flame radius measured using the laminar CVR Schlieren setup and the Flame Code. Stoichiometric mixture between n-heptane and air at 300 K and 1 bar.

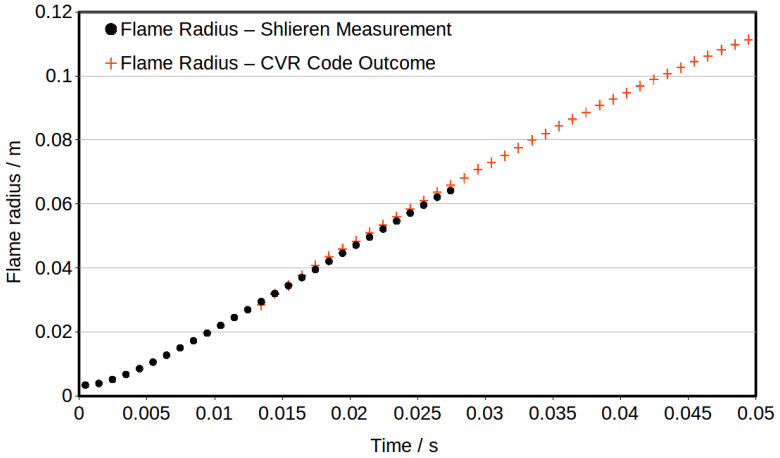

Figure 4.28–Flame radius measured using the laminar CVR Schlieren setup and the Flame Code. Stoichiometric mixture between iso-octane and air at 300 K and 1 bar.

All the experiments resulted in the same degree of agreement.

4.4.3.3 Comparison with Data from the Literature

Figure 4.29 shows the results of flame speed for methane, n-heptane and iso-octane. The curve-fitted curves are just used to guide the eyes. Figure 4.30 presents results for the laminar flame speed of methane-air mixtures from a collaborative study involving seven institutes, six from Europe and one from USA (Beeckmann et al., 2013). The result obtained using the GRIMECH 3.0 mechanism is also shown. The data was taken from three different experiments: constant volume reactor, counter flow burner and flat burner. The methods of measurement were also different for each experiment, employing particular optical setups when necessary. It should be noted that the results present a considerable scattering, mainly in the rich region. This scatter is attributed mainly to flame curvature and heat loss effects in the different methods. Figure 4.31 shows the comparison between the laminar CVR methane results and those published by (Beeckmann et al., 2013), the RWTH results in Figure 4.30. Figure 4.32 and Figure 4.33 present the comparison for n-heptane and iso-octane mixtures, respectively, to the results reported by (Davis & Law, 1998).

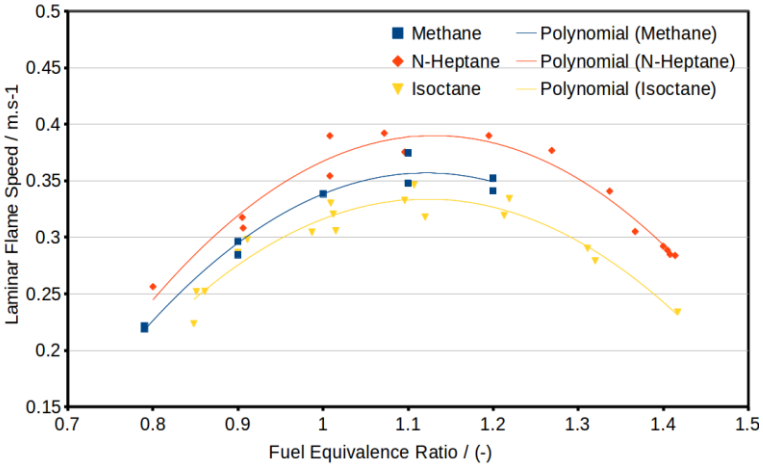

Figure 4.29– Laminar flame speed of air mixtures with methane, n-heptane and isooctane. Initial temperature and pressure of 300 K and 1 bar.

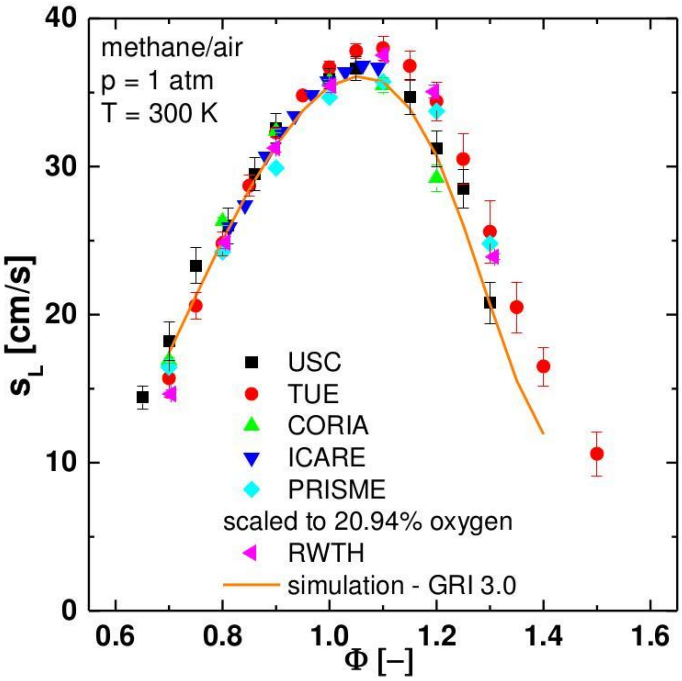

Figure 4.30– Laminar flame speed of methane/air mixtures at 300 K and 1 bar. Adapted from (Beeckmann et al., 2013).

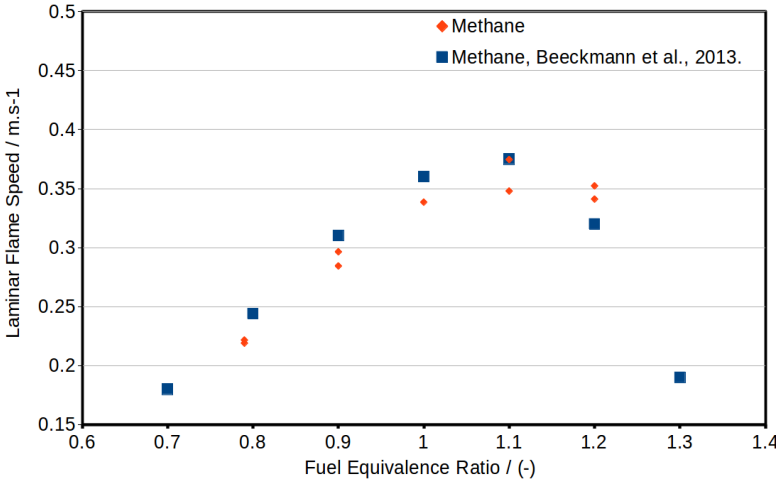

Figure 4.31– Laminar flame speed of methane/air mixtures at 300 K and 1 bar. Adapted from (Beeckmann et al., 2013).

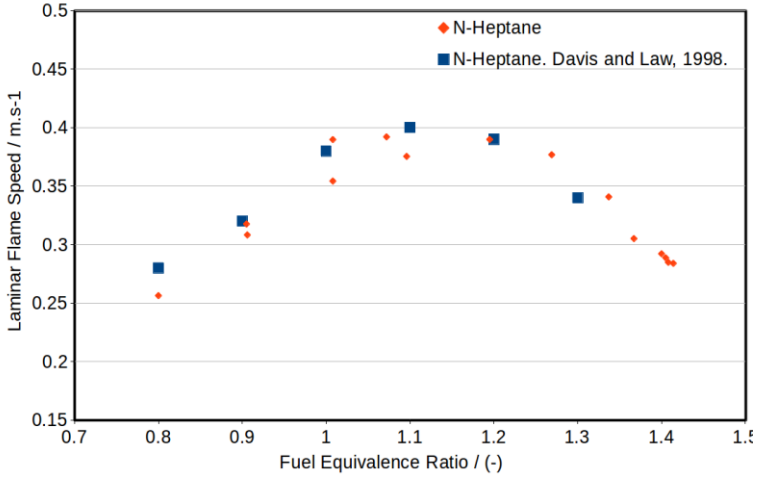

Figure 4.32–Comparison of laminar flame speed of n-heptane/air mixtures at 300 K and 1 bar. Some results were adapted from (Davis & Law, 1998).

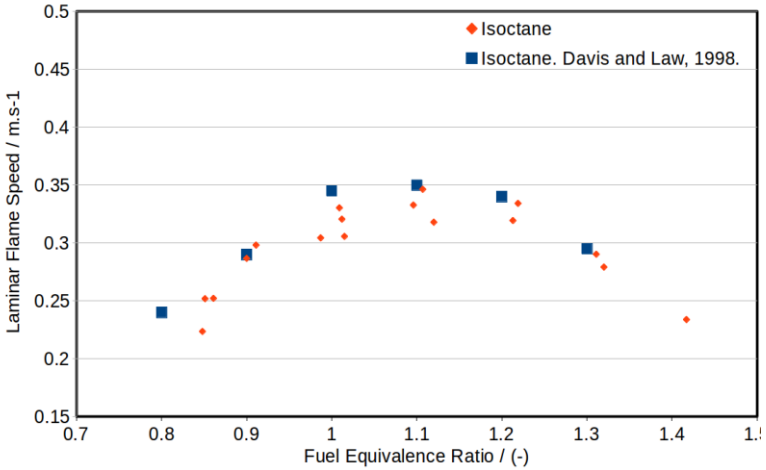

Figure 4.33–Comparison of laminar flame speed of iso-octane/air mixtures at 300 K and 1 bar. Some results were adapted from (Davis & Law, 1998).

The measurements obtained from the CVR present a larger scatter, but they compare well to the measurements reported in the literature. The scatter is mainly attributed to the difficulty in establishing the correct value of equivalence ratio. For the gaseous fuel (methane) the accuracy of the pressure measurements come into play. For the liquid fuels (isocotane and n-heptane) complete evaporation and mixing are the most important sources of error. Nevertheless, the agreement is considered sufficient for this work. Suggestions to decrease the error bounds are reported in (E. M. Hartmann, 2014).

After obtaining the flame speed the thermal flame thickness may be estimated. Other parameters that can be estimated are the flame expansion factor, the energy burned by the flame, the flame jump of internal energy, the work done by the flame, but these are not explored in this work.

Figure 4.349 shows a simplified flowchart of the CVR Flame Code and the relationship between the others measurement system components. Appendix II presents a more detailed description of the CVR Flame Code.

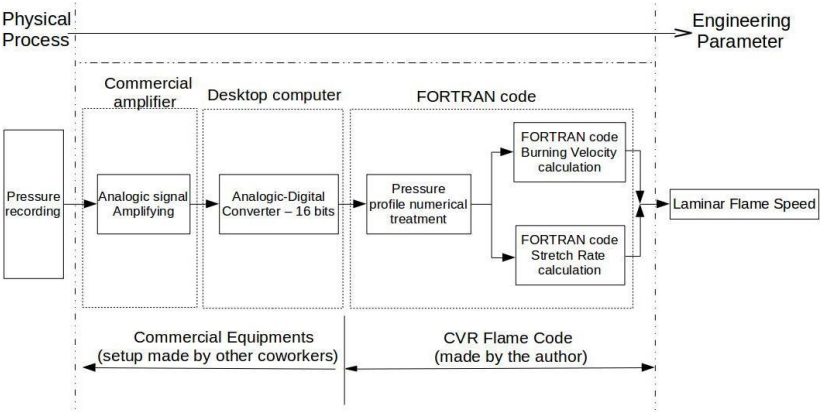

Figure 4.34– Simplified CVR Flame Code external information flow chart.

4.5 RCM and CVR Experimental Uncertainties Analysis

This section presents the uncertainty analysis applied to the experimental facilities. The main goal here is to present an introductory analysis, to give the reader an indicative of the degree of uncertainty related to the experimental results. The analysis starts with the RCM and then the CVRs experiments will be addressed. The main equation used for the analysis is (Montgomery, 2003),

$$u^2(G) = \sum_{i=1}^{n} \left(\frac{\partial f}{\partial X_i}\right)^2 u^2(X_i) + 2\sum_{i=1}^{n-1}\sum_{j=i+1}^{n} \left(\frac{\partial f}{\partial X_i}\right)\left(\frac{\partial f}{\partial X_i}\right) u(X_i)u(X_j)r(X_i, X_j) \qquad (4.14)$$

where G is the quantity to be indirect measured, $u(G)$ is the combined uncertainty related with the indirect measurement of the quantity G, f is the function between the quantity G and the input variable X, $u(X)$ is the uncertainty related with the measurement of the input quantity X and $r(X_i, X_j)$ is the correlation function for the inputs.

4.5.1 RCM Analysis

The result of a single RCM experiment is the ignition delay time, for a certain fuel equivalence ratio, temperature and pressure. The uncertainty in the results is related with the indirect measurements of the fuel equivalence ratio, ignition delay time and the direct measurement of the initial pressure, also used for the calculation of the initial temperature. Thus, the initial temperature is also an indirect measured quantity.

The equivalence ratio is calculated using the partial pressure method,

$$\Phi = \left(\frac{p_{fuel}}{p_{air}}\right) / f_{est} \tag{4.15}$$

where p_{Fuel} is the fuel partial pressure, p_{air} is the oxidant partial pressure and f_{est} is the stoichiometric fuel-air ratio.
Consider for instance the Jet A-1 sample described in the section 2.4, mixed with synthetic air (20% O2 in N2), for initial pressure of 2 bar inside of the mixing chamber described in the section 4.1.1. Table 4.3 shows the main characteristics of a lean, stoichiometric and rich mixtures.

Table 4.3–Theoretical partial pressure for mixtures between the studied Jet A-1 and synthetic air. Synthetic air is 20% O2 in N2.

Φ	0.5	1.0	1.5
$p_{fuel}\,/bar$	0.01230	0.02446	0.03647
$p_{air}\,/bar$	1.98769	1.97553	1.96352

The partial derivatives of the equivalence ratio related with the fuel and the air partial pressures are respectively,

$$\frac{\partial \Phi}{\partial p_{fuel}} = \left(\frac{1}{p_{air}}\right) / f_{est} \tag{4.16}$$

$$\frac{\partial \Phi}{\partial p_{air}} = \frac{-p_{fuel}}{p_{air}^2}\frac{1}{f_{est}} \tag{4.17}$$

Both the fuel and air partial pressure are measured using the same instrument, an absolute pressure transducer Baratron type 121 A. The absolute pressure is displayed with a resolution of 0.1 mbar. The uncertainty of the measurements is 0.05 mbar.
The expanded uncertainty in the equivalence ratio evaluation can be now calculated using the equations 4.15, 4.16 and 4.17, the values from the table Table 4.3 and the absolute pressure measurement uncertainty. Table 4.4 summarizes the expanded equivalence ratio uncertainty analysis applied to the studied Jet A-1 and synthetic air mixtures.

Table 4.4– Uncertainty analysis applied to the studied Jet A-1 and synthetic air. Synthetic air is 20% O2 in N2.

Φ	0.5	1.0	1.5
$\partial \Phi / \partial p_{fuel}$	40.6190	40.8690	41.1190
$\partial \Phi / \partial p_{air}$	-0.25154	-0.5061	-0.76393
$(\partial \Phi / \partial p_{fuel})^2$	1649.90	1670.27	1690.77
$(\partial \Phi / \partial p_{air})^2$	0.06327	0.25623	0.58359
u(TP) / bar	0.00005	0.00005	0.00005
$u(\Phi)$	0.002031	0.02043	0.02056
$u(\Phi)$/ %	0.41	2.04	1.37

It is interesting to note that the highest uncertainty is for the stoichiometric mixture, about 2%.

The uncertainty in the evaluation of the ignition delay time is related with the time assignments, like shown in Figure 4.3. The initial time t_1 is determined using the position profile, measured using a very sensitive position probe, *Burster* model 8712 EN. The end counting time t_2 is calculated using the pressure trace measured using a piezoelectric pressure transducer, like described in the section 4.1.1. Both signals, the piston position and inner combustion chamber pressure, are computed using a Matlab code, that calculates the instants t_1 and t_2.

As the piston position is determined using a very sensitive device, designed for faster applications compared with the RCM, the main uncertainty source will be due the pressure signal acquisition. The pressure profile is recorded using a quartz sensor followed by a charge amplifier (Kistler 6061 B, 5011B). The nominal uncertainties are 0.05 and 0.02 for the sensor and the amplifier respectively. Thus, the combined uncertainty in the pressure measurement chain is calculated by,

$$u(pressure) = \sqrt{u(sensor)^2 + u(amp)^2} = \sqrt{0.05^2 + 0.02^2} = 0.0504 bar \quad (4.18)$$

The instant t_2 is assigned as the peak of the pressure time derivative, as showed in in Figure 4.3. This derivative is large, about 1,200 bar/s. The acquisition rate for the pressure signal is 10 kHz, thus at each acquisition point, the pressure increasing is about 1,200/10,000 = 0.12 bar. This

is more than twice the uncertainty level in the pressure acquisition chain. Thus, the uncertainty in the determination of the time instants for the ignition delay time calculation will be neglected.
But, for the initial pressure used as reference for the results plotting, the pressure uncertainty is surely an issue. For this case, the uncertainty will be taken as 0.0504 bar, following equation 4.18. Considering the lowest experimental pre-compression pressure, 2 bar, the relative uncertainty is about 2.5%.

4.5.2 CVR Analysis

The experimental procedure for the both CVRs is quite similar. The reactor is filled with a new fuel-oxidizer mixture at each experimental shot, the spark is triggered and the pressure profile is then recorded. The main concern are the uncertainties related to the equivalence ratio evaluation and pressure signal acquisition, the calculation of the burning velocity and then, the obtainment of the laminar, or turbulent, flame speed.
As described in the section 4.3.1 the laminar, or turbulent, burning velocity is calculated using the equation 4.8. Except for the initial mass m_i, all other parameters are functions of the measured pressure profile, in non-linear relationships. The burned gases mass fraction $x_b$is obtained from the resolution of the volume conservation equation 4.12. The specific volume v_u can be calculated through the application of the ideal gas law, but it is necessary to have the value of a temperature, obtained from an isentropic compression calculation. The flame surface A_{flame} is also calculated using the specific volume and burned gases mass fraction. All of the variable are intrinsically correlated, thus the uncertainty assessment by means of equation 4.14 is very hard to achieve.
Both laminar and turbulent flame speeds, the main results showed in the chapters 174 and 178, are calculated through the use of curve-fitting strategies. These fitting processes have a characteristic quality coefficient, known as R-square. This R-square can be used as an indicative of the uncertainty of the results, the closer to the unity the best the agreement. For all of the studied Jet A1-1 and Jet A-1 + HEFA surrogates mixtures, the R-square coefficient was within the range between 0.95 and 1.00.
In the next two sub-section, the fuel equivalence ratio uncertainty will be addressed.

4.5.3 Turbulent CVR

The experimental procedure for the turbulent CVR is quite similar compared with the RCM, considering the equivalence ratio evaluation. The partial pressure method is also used and the pressure transducer is the same model, a Baratron type 121 A. So, one can expect that the uncertainties in the equivalence ratio calculation for the turbulent CVR will be similar those shown in the Table 4.4.

It should be noted that, the Table 4.4 shows values for a kerosene type fuel, which has a mean molecular formula $C_{11.5}$. For smaller hydrocarbons, the fuel partial pressure considering the same equivalence ratio, will increase. And the oxidizer partial pressure will decrease. By the evaluation of the equations 4.15, 4.16 and 4.17 it is possible to see that, in this case, equivalence ratio uncertainty will be lower compared with kerosene type fuels.

Taking a stoichiometric air methane mixture at initial pressure and temperature of 1 bar and 300 K, the equivalence ratio uncertainty will be about 0.5 %. In this study only isooctane, methane and n-heptane mixtures were measured in the Turbulent CVR.

In the turbulent CVR, the pressure profile was obtained also using a quartz sensor followed by a charge amplifier (Kistler 6061 B, 5011B). So, the uncertainty in the pressure measurements is also 0.12 bar.

4.5.4 Laminar CVR

The experimental procedure for the laminar CVR is very similar compared with the turbulent one. But for the laminar facility, the fuel mass is measured using a very sensitive weight machine (Katashi model KA2204), with a resolution of 0.0001 g and measurement uncertainty of 0.0002 g. Applying the equation 4.15, considering a Jet A-1/air stoichiometric mixture, the equivalence ratio uncertainty due the fuel mass measurement is about,

$$u(mass_{fuel}) = \sqrt{0.025^2 . 0.002^2} < 10^{-10} \qquad (4.19)$$

So, the uncertainty in the equivalence ratio for the laminar CVR is smaller than for the turbulent one. In the laminar CVR, the pressure profile was obtained using also a quartz sensor followed by a charge amplifier (Kistler 6041 BS31, 5018A). Thus, the uncertainty in the pressure measurements is also about 0.12 bar. Considering the utilized pressure transducer has a measurement range of 0 to 250 bar, the application of a transducer with a range about 0 to 15 bar will improve

the results quality.
Figure 4.35 shows the same results as Figure 4.33. There are also shown the uncertainty bars obtained using the Equations 4.14, 4.15, 4.16 and 4.17, calculated for the fuel equivalence ratio. Figure 4.35 can be considered as representative of the experimental results reported in section 4.4.3.3. It is possible to see the uncertainty in equivalence ratio is larger for rich mixtures and smaller for lean mixtures.

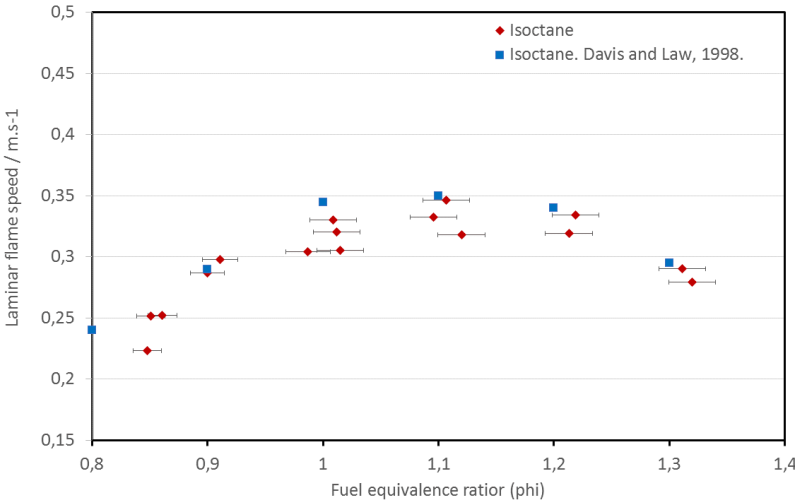

Figure 4.35–Comparison of laminar flame speed of iso-octane/air mixtures at 300 K and 1 bar. There are also shown uncertainties intervals in the fuel equivalence ratio. Some results were adapted from (Davis & Law, 1998).

As discussed in section 4.5.2, it is not possible to have the uncertainty for the laminar flame speed and then it is neglected Figure 4.35. The accurate assessment of the uncertainty in the laminar flame speed calculations in a very interesting task and will be carried out in a future work.

5 RESULTS AND ANALYSIS

In the following, results for ignition delay time, flame ignition and extinguishment and laminar and turbulent flame speed are presented and discussed.

5.1 Ignition Delay Time

Ignition delay times, IDT, for Jet A-1/oxidizer mixtures were measured using a heated rapid compression machine, at compressed pressures of 7, 8 and 15 bar, post-compression temperature span from 630 to 895 K and equivalence ratio varying from 0.3 to 1.3. Argon and carbon dioxide were utilized as diluting gas, in addition or not with nitrogen, depending on the target experimental condition.

5.1.1 Experimental matrix

The experimental matrix showed in Table 5.1 was planned to provide insights in the behavior of the Jet A-1 under study when submitted to variations in equivalence ratio, pressure and temperature.

Table 5.1 - Theoretical partial pressure for mixtures between the studied Jet A-1 and synthetic air. Synthetic air is 20% O_2 in N_2.

Condition number	Equivalence ratio Φ	Inert gases in the oxidant	Initial pressure (bar)	Initial temperature range (K)
1	0.3	Only N_2	15 +/- 0.5	662 – 731
2	0.3	Only N_2	15 +/- 0.5	840 – 890
3	0.7	N_2 and CO_2	7 +/- 0.5	655 – 890
4	0.7	Only N_2	8 +/- 0.5	748 – 822
5	0.7	N_2 and Ar	15 +/- 0.5	649 – 706
6	1.0	N_2 and CO_2	7 +/- 0.5	639 - 895
7	1.0	Only CO_2	15 +/- 0.5	640 - 677
8	1.3	N_2 and Ar	7 +/- 0.5	630 – 864

The initial pressure and temperature are taken as the maximal respective values at the TDC, instead of a time averaged value described by the equation 4.2. These values correspond to the time instant t = 0 ms,

showed in Figure 4.3. This approach is more suitable for comparisons between the RCM experimental and chemical kinetics simulations results.
It is very hard to obtain exactly the targeted initial pressure, thus an uncertainty interval was considered. The uncertainty range in the column initial pressure, +/- 0.5 bar, does mean that all the experimental shots outside this range were not used in the result graphs. Section 4.5 presented an introductory uncertainty analysis applied to the RCM experiments.
It should be noted almost all the ensuing figures have the same scale, both on horizontal and vertical axis to facilitate the results comparison.

5.1.2 Effect of fuel equivalence ratio

Figure 5.1 shows the results of the IDT for three experimental conditions, all of them at initial pressure of 7 bar. The results were grouped in equivalence ratios of 0.7, 1.0 and 1.3. Fifth order polynomials were curve-fitted to the data to guide the eye. It is possible to detect a decreasing trend in the IDT as the equivalence ratio increases. There is a clear negative temperature coefficient – NTC phenomenon. It is more pronounced for phi = 1.3. It is interesting also to note that, the NTC is longer for phi = 0.7, from the reciprocal temperature of 1.4 through 1.18. For the phi = 1.3 curve, the NTC is the shortest one, from the reciprocal temperature of 1.33 till 1.2. The NTC curve topology is becoming flat, as the equivalence ratio is shifted to the lean limit. It should be noted also that, in the NTC region, the distance between the curves phi = 0.7 and phi = 1.0 is remarkably larger than the distance between phi = 1.0 and phi = 1.3.

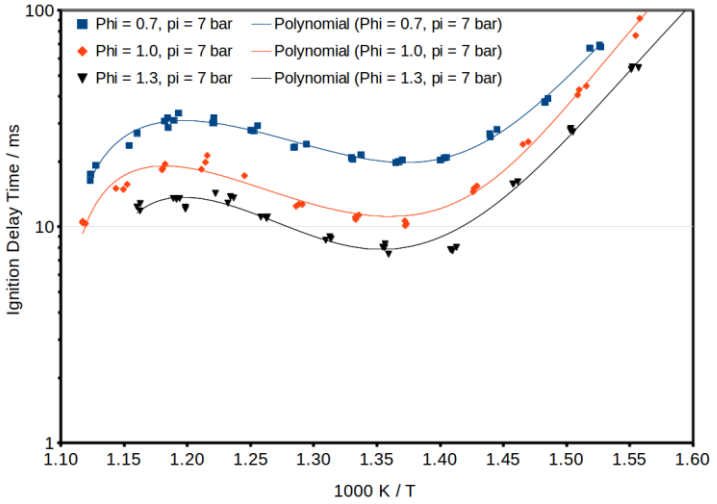

Figure 5.1– Ignition delay time as a function of reciprocal temperature. Results are shown for initial pressures of 7 bar and equivalence ratios of 0.7, 1.0 and 1.3. There are three 5th degree polynomial curves fitted to facilitate the results comparison.

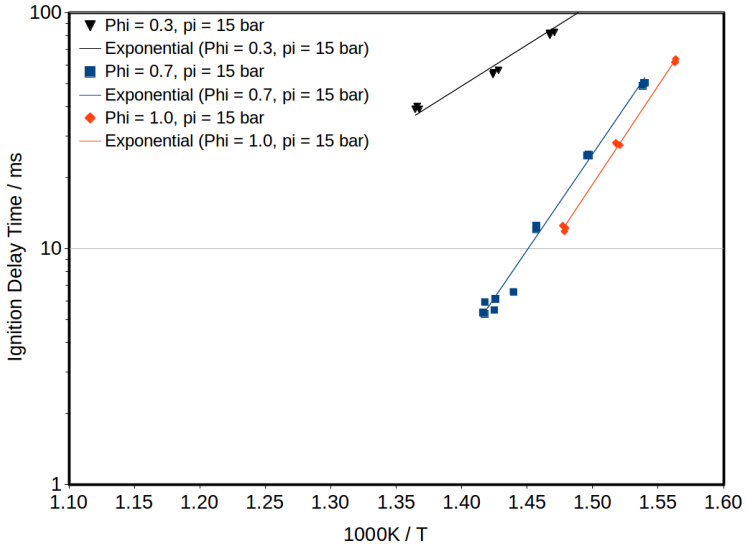

Figure 5.2– Ignition delay time as a function of reciprocal temperature. Results are shown for initial pressures of 15 bar and equivalence ratios of 0.3, 0.7 and 1.0. There are three exponential curves fitted to facilitate the results comparison.

Figure 5.2 shows the results of the IDT for three experimental conditions, all of them at initial pressure of 15 bar. The graph shows a comparison for temperatures range 640 – 732 K, reciprocal temperature from 1.56 till 1.36. The equivalence ratios studied covered the lean region, more related with the operation conditions present in the second region of a jet engine combustion chamber. The lean region is important mainly because the lean flammability and extinction limits are closer to the lean turbine operation condition, instead of the rich limits. Quite similar to Figure 5.1, there is a strong trend to IDT decrease with the increase of the equivalence ratio. Also a comparable behavior is the distance between the curves phi = 0.3 and *phi* = 0.7, that is bigger than the distance between *phi* = 0.7 and *phi* = 1.0. It should be also noted for Figure 5.2 the slope of the IDT curves is higher for higher equivalence ratios, and the slopes for *phi* 0.7 and *phi* = 1.0 are almost the same.

5.1.3 Effect of pressure

The influence of the pressure on the IDT of Jet A-1 flammable mixtures is presented using the curve for phi = 0.7 and p = 7 bar as reference. Figure 5.3 shows the comparison among the 7 bar reference curve with two curves, of 8 and 15 bar. The comparison regions were selected to provide some insights about the pressure sensitivity in the low temperature region, 650 – 700 K, and within of the NTC region, 715 – 850 K.

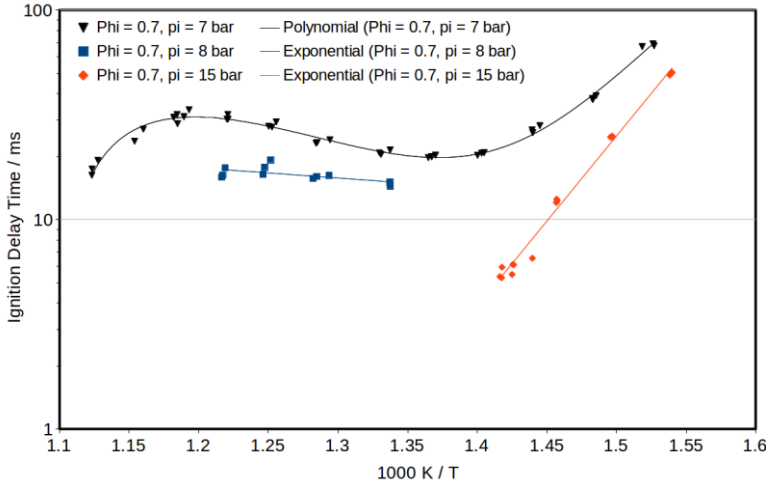

Figure 5.3– Ignition delay time as a function of reciprocal temperature. Results are shown for equivalence ratio of 0.7 and initial pressures of 7, 8 and 15 bar. There are three fitted curves to facilitate the results comparison.

Comparing the three curves, it is possible to see that the IDT decreases with the increase of the pressure. This decrease is more pronounced for the NTC region, where a smaller percentage increasing in the pressure leads a more pronounced decrease for the IDT, compared with the low temperature region. Similarly as showed in Figure 5.2 there is a difference in the slope of curves for the low temperature region. The slope is steeper as the pressure increases.

Figure 5.4 shows the comparison for mixtures with phi = 1.0 and initial pressures of 7 and 15 bar. Again, the IDT decreases as the pressure increases. The slope of the curve for 15 bar is slightly more pronounced compared with the 7 bar.

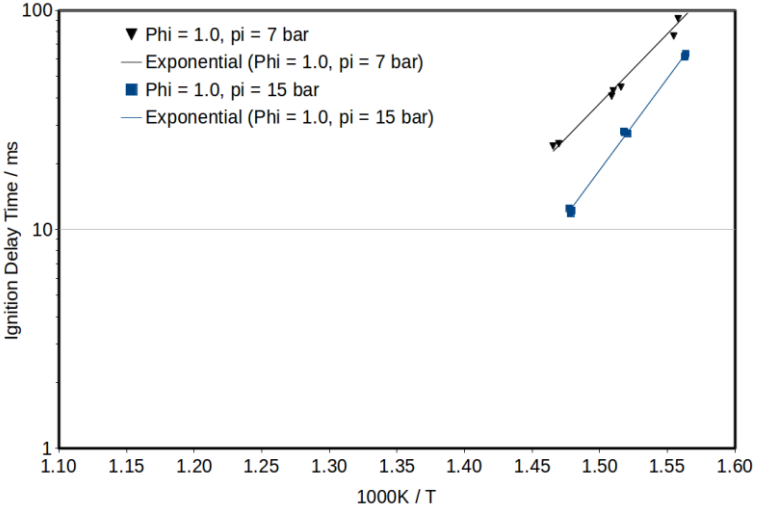

Figure 5.4– Ignition delay time as a function of reciprocal temperature. Results are shown for equivalence ratio of 1.0 and initial pressures of 7 and 15 bar. There are two exponential curves fitted to facilitate the results comparison.

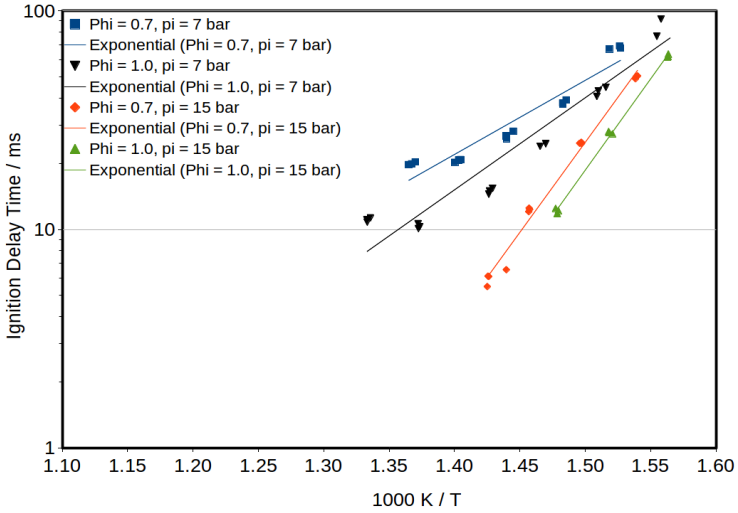

Figure 5.5– Ignition delay time as a function of reciprocal temperature. Results are shown for equivalence ratios of 0.7 and 1.0 and initial pressures of 7 and 15 bar. There are exponential curves fitted to facilitate the results comparison.

Figure 5.5 summarizes the comparison of the dependence on the pressure, in the low temperature region. There are four curves grouped for two different initial pressures. It is clear to see that for the same pressure the curves are closer and have almost the same slope. As the pressure increases the curve slopes clearly increases. So, the IDT curve slopes are more sensitive to the pressure compared with the equivalence ratio.

5.1.4 Analysis of two-stage ignition phenomenon

Figure 5.6 to Figure 5.11 show the results considering the two-stage ignition phenomenon. The results were organized to compare the influence of equivalence ratio and pressure, as already presented for the overall IDT in sections 5.1.2 and 5.1.3 respectively.

Figure 5.6 to Figure 5.8 compare the results for initial pressure of 7 bar and equivalence ratios of 0.7, 1.0 and 1.3, similarly as showed in Figure 5.1.

Comparing Figure 5.6 through Figure 5.8 it is possible to see that the points related to the first stage ignition and for the overall ignition remain closer for phi = 1. It is interesting to note that, this trend occurs for the same condition where there was a NTC flattening, as discussed

in the section 5.1.3. Figure 5.7 shows the same flattening trend compared with Figure 5.6.
Figure 5.8 to Figure 5.11 cover the low temperature ranges for initial pressures of 15 bar and equivalence ratios of 0.3, 0.7 and 1.0, similarly as showed in Figure 5.2.

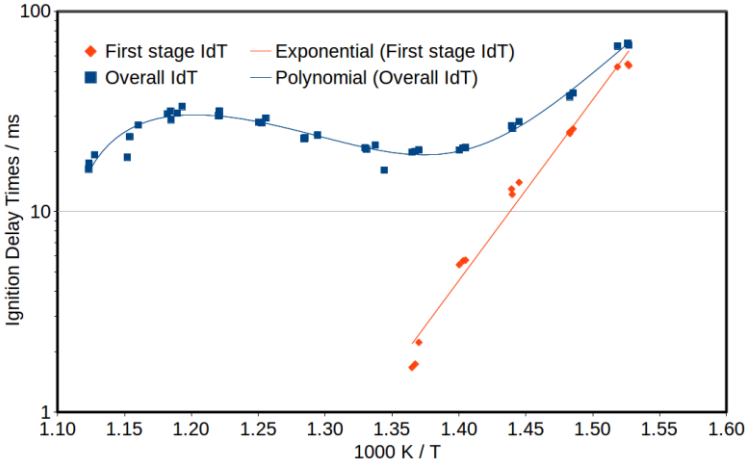

Figure 5.6– Ignition delay times for the Jet A-1 mixtures as function of reciprocal temperature, at initial pressure of 7 bar and equivalence ratio of 0.7.

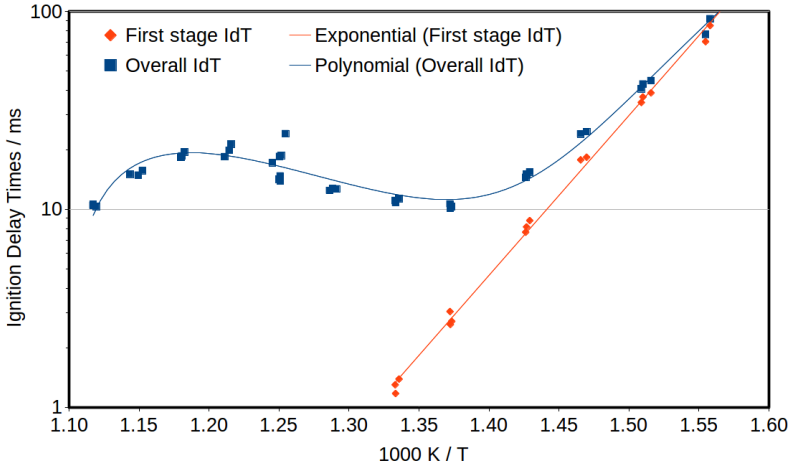

Figure 5.7– Ignition delay times for the Jet A-1 mixtures as function of reciprocal temperature, at initial pressure of 7 bar and equivalence ratio of 1.0.

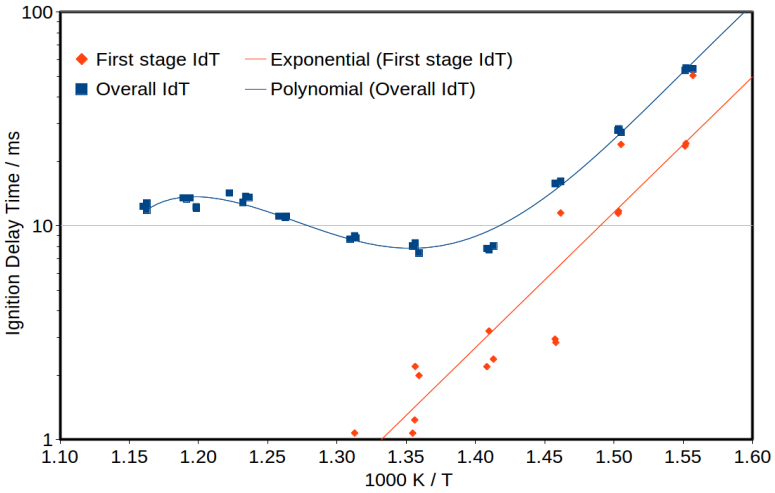

Figure 5.8– Ignition delay times for the Jet A-1 mixtures as function of reciprocal temperature, at initial pressure of 7 bar and equivalence ratio of 1.3.

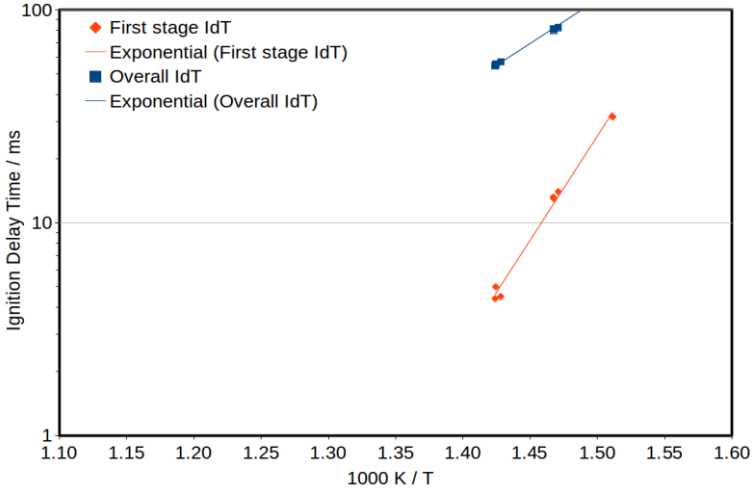

Figure 5.9– Ignition delay times for the Jet A-1 mixtures as function of reciprocal temperature, at initial pressure of 15 bar and equivalence ratio of 0.3.

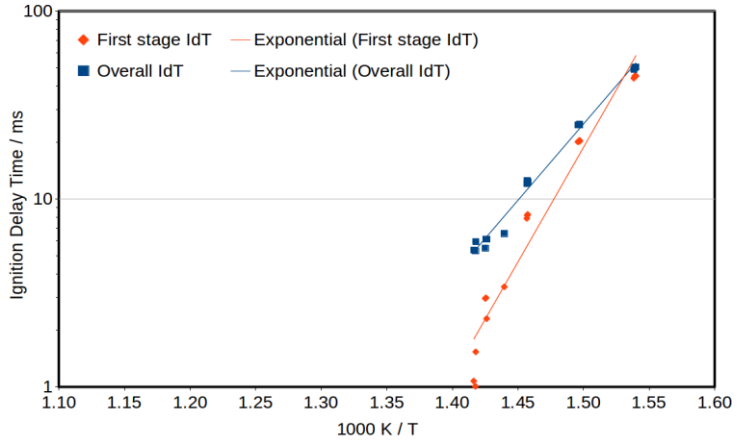

Figure 5.10– Ignition delay times for the Jet A-1 mixtures as function of reciprocal temperature, at initial pressure of 15 bar and equivalence ratio of 0.7.

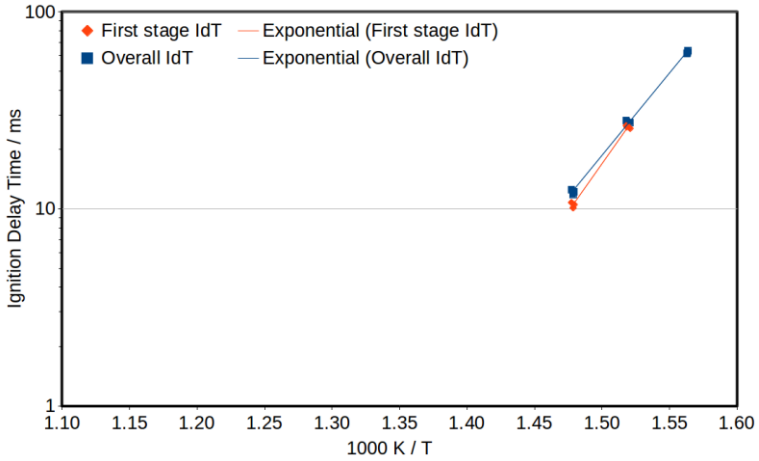

Figure 5.11– Ignition delay times for the Jet A-1 mixtures as function of reciprocal temperature, at initial pressure of 15 bar and equivalence ratio of 1.0.

Figure 5.12 and Figure 5.13 show the results of the first-stage ignition delay times. Figure 5.12Figure 5.13 shows the results in the low temperature range for initial pressure of 7 bar and equivalence ratios of 0.7, 1.0 and 1.3. It is possible to note that there are very small differences in the first stage IDT for different equivalence ratios. Also, the slope of the fitted curves are almost the same.

Figure 5.13 shows the results in the low temperature range for initial

pressure of 15 bar and equivalence ratios of 0.3, 0.7 and 1.0. It is possible to note again that, there are very small differences in the first stage IDT for different equivalence ratios. Also, the slope of the fitted curves are almost the same.

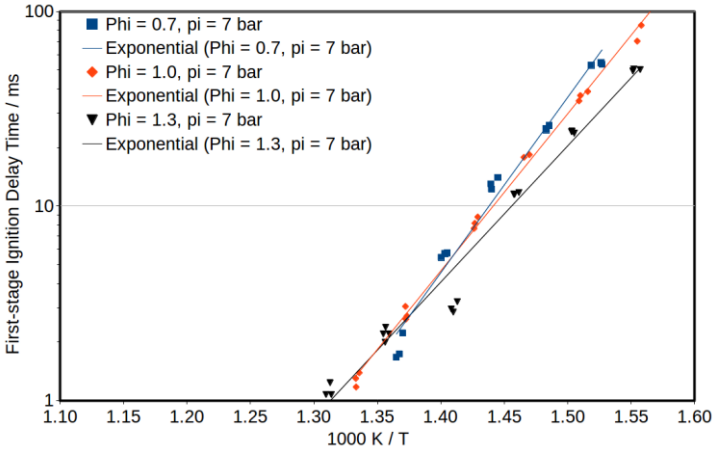

Figure 5.12– First-stage ignition delay times for the Jet A-1 mixtures as function of reciprocal temperature, at initial pressure of 7 bar and equivalence ratio of 0.7, 1.0 and 1.3.

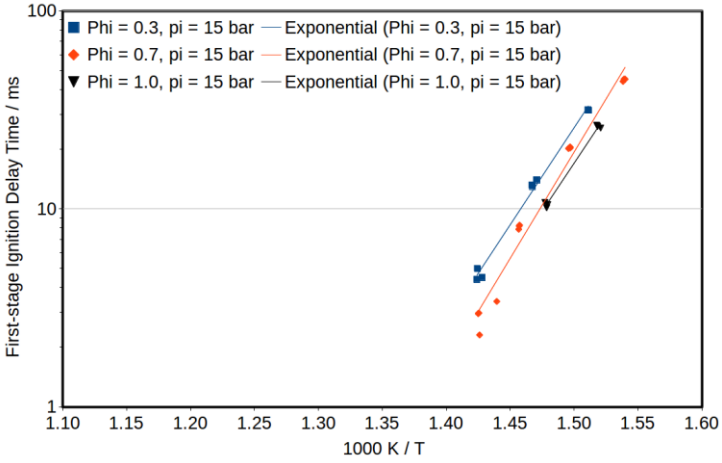

Figure 5.13– First-stage ignition delay times for the Jet A-1 mixtures as function of reciprocal temperature, at initial pressure of 15 bar and equivalence ratio of 0.3, 0.7 and 1.0.

Figure 5.14 groups the results for phi 0.7 and 1.0 and for initial pressures of 7 and 15 bar. It is remarkable that it confirms the results discussed for Figure 5.12 and Figure 5.13. It is easy to discern that the curve slopes are almost the same for the same pressure groups, varying with the equivalence ratios, and increase with the pressure increasing. The first-stage IDT curve slopes are clearly more sensitive to the pressure compared with the equivalence ratio.

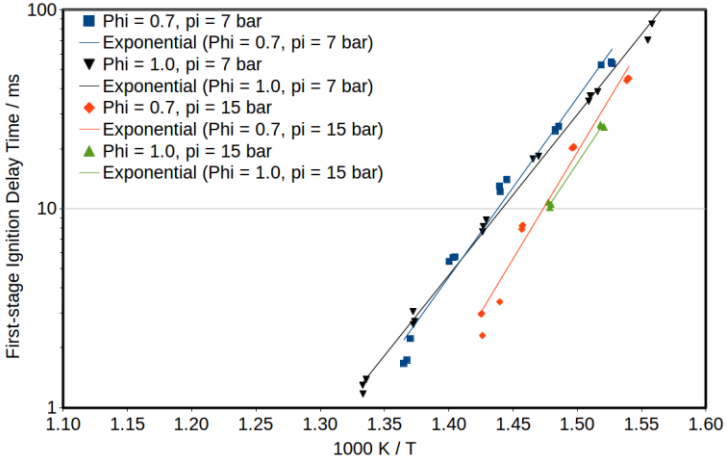

Figure 5.14– First-stage ignition delay times for the Jet A-1 mixtures as function of reciprocal temperature, at initial pressure of 7 and 15 bar and equivalence ratio of 0.7 and 1.0.

5.1.5 Comparison with Shock Tube measurements

Figure 5.15 brings an important discussion about experiments complementarity. Figure 5.15 shows results obtained for the same jet A-1 sample, using the ITT-RCM facility and the Shock Tube (ST) located at the Institute of Combustion and Dynamic of Gases (IVG) of the University of Duisburg Essen at Duisburg/Germany.

The discussion about experiment complementarity is important in the data interpretation. When some flammable mixture is being studied, and the experiments for the determination of ignition delay times are carried out in conjunction using a RCM and a ST, each one is indicated for a specific temperature and pressure ranges. Care must be taken in the data interpretation and comparison, as they are different machines, with different physical governing phenomena and operational procedures. But in the end, as both machines are measuring the same physical quantity, the results should match in the respective temperature

experimental range limits. It is possible to verify in Figure 5.15 the results obtained using the RCM and the ST are matching quite well. If a curve were fitted to the results containing all the RCM and ST points together, it is easy to check that this new continuous curve will be similar to the curves shown in Figure 5.1.

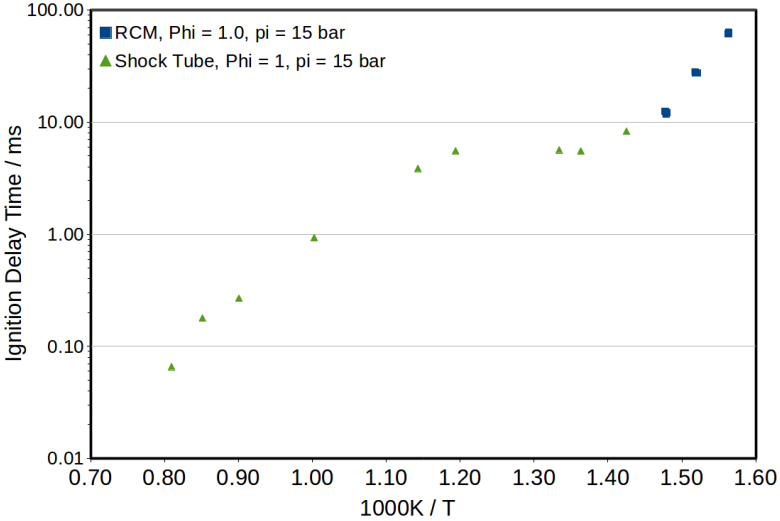

Figure 5.15– Ignition delay time as a function of reciprocal temperature. Shown are results obtained in experiments using the ITT RCM and a Shock Tube (IVG/University of Duisburg-Essen). The Shock Tube experiments were adapted from an internal technical report, contract FEESC-UFSC and IVG-UniDuisburg, Cancino, L. R. (2012).

Also, it is possible to note a weak NTC phenomenon depicted in Figure 5.15. But in a more rigorous analysis, it is not possible to say confidently if there is a NTC or simply a “temperature plateau”.

5.1.6 Curve-fitting the ignition delay time

One of the main goals of this investigation is to provide a set of fitting coefficients that could be used for ignition delay time predictions. The coefficients were obtained from the fitting curves shown in Figure 5.5, Figure 5.6, Figure 5.7 and Figure 5.8. The presentation of the coefficients is summarized in Table 5.2. The fitted coefficients where applicable to following exponential,

$$\tau_{exp} = a_1 exp\left(a_2 \frac{1000}{T}\right) \quad (5.1)$$

With the empirical fitting coefficients it is possible to predict the ignition delay times as function of the temperature in K. Also, the analysis of the coefficients applicable to the equation 5.1, allows to obtain the global activation energy of some mixtures between the Jet A-1 and oxidants.

Furthermore, with the raw coefficients for each curve, it is possible to develop some scaling process, and even to have an unique scaled equation as a function of equivalence ratio, pressure and temperature.

For a more physical meaningful relationship, the coefficients for an Arrhenius type equation are presented. The fitting coefficients are related to the results showed in Figure 5.5 and Figure 5.14. The results are for the overall and first-stage ignition delay time respectively. The fitting coefficients are shown equation 5.2,

$$\tau = A_1 exp\left(\frac{E_A}{R_u}\frac{1000}{T}\right) \quad (5.2)$$

where the τ is in ms, A_1 is the pre-exponential factor in ms, E_A is the activation energy in kJ/kgmol, R_u is the universal gas constant in kJ/kgmol-K and T is the temperature in K. Table 5.2 summarizes the experimental conditions and the obtained coefficients.

The analysis of the values showed in Table 5.2, shows that the activation energy is more sensible to the pressure and this is more pronounced for the overall IDT. This is in accordance with the discussions for the IDT curve slopes, carried out in sections 5.1.2 and 5.1.3.

Table 5.2 - Fitting curve coefficients for IDT prediction.

Φ	p_i(bar)	IDT type	Temperature range (K)	A_1(ms)	E_A/Ru(K)	R^2
0.7	7	First-stage	653 - 730	4.79E-07	6,601	0.9804
1.0	7	First-stage	640 - 750	2.28E-11	18,5993	0.9974
0.7	15	First-stage	665 – 700	1.53E-15	24,713	0.9748
1.0	15	First-stage	653 - 685	4.70E014	22,346	0.9921
0.7	7	Overall	653 - 735	3.93E-04	7,810	0.9184
1.0	7	Overall	625 - 700	4.02E-10	12,155	0.9973

1.0	7	Overall	720- 830	1.68E-00	-3,750	0.9973
1.0	7	Overall	835 - 900	1.06E-08	12,335	0.9973
0.7	15	Overall	649 - 701	1.09E-11	18,970	0.9881

Figure 5.16 shows fitting curves and the respective equations, for low, intermediate and high temperature regions. It is interesting to note that for phi 1.0 at 7 bar, the Arrhenius equations are quite similar for low and high temperatures, indicating, the activation energy for the both regions are quite similar.

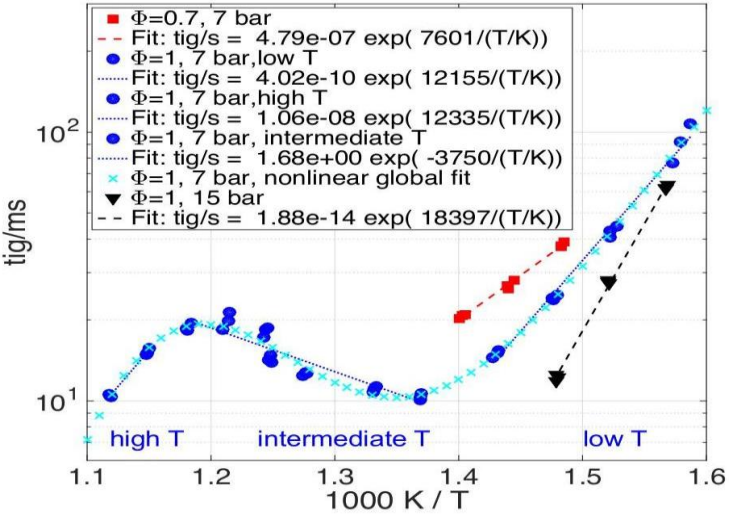

Figure 5.16– Arrhenius modeling applied to experiments at initial pressure of 7 and 15 bar and equivalence ratios of 0.7 and 1.o. Also shown the fitting curves and the respective equations, for low, intermediate and high temperature regions.

5.1.7 IDT Concluding Remarks

Ignition delay times for Jet A-1/oxidizer mixtures were measured using a heated rapid compression machine, at compressed pressures of 7, 8 and 15 bar, post-compression temperatures ranging from 630 to 895 K and equivalence ratios varying from 0.3 to 1.3.

In general the results showed a trend of decreasing IDT with the increase of pressure and equivalence ratio. For initial pressure of 7 bar and equivalence ratio of 0.7, 1.0 and 1.3, a noticeable NTC phenomenon was observed. The NTC curve was more pronounced for the stoichiometric and rich mixtures. For the lean mixtures, it was observed

that the curve became flatter. Furthermore, for the lean mixture limits it is expected that, the IDT curve behave like a straight line through all the temperature range of interest, like shown in Figure 5.17.

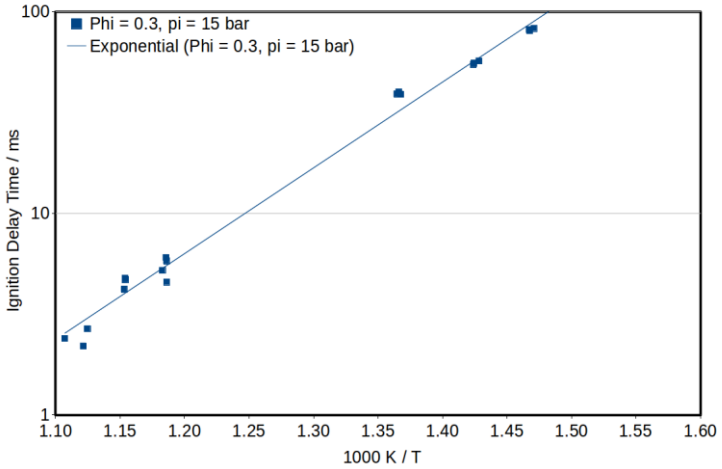

Figure 5.17– Ignition delay time as a function of reciprocal temperature. It is shown results for equivalence ratios of 0.3 and initial pressure 15 bar. It is also presented the fitted curve and respective exponential equation.

The results comparison for RCM and ST experiments showed a very good agreement between the data, as shown in Figure 5.15. The complementary analysis of Figure 5.15 shows a clear tendency to the flattening of the NTC curve topology with the pressure increasing, being so, one more indicative for the NTC flattening, and vanishing, for high pressures and equivalence ratios.

The analysis of the curve slopes in the Figure 5.5 and Figure 5.14 regarding the coefficients in Table 5.2, allow to conclude that activation energy for the first-stage IDT are the same order of magnitude. But, the activation energy for the overall IDT is clearly more influenced by the initial pressure. The higher the pressure, the higher will be the activation energy for the overall IDT.

It is important to recall that, as showed in Figure 2.1, the primary zone in the combustion chamber is a rich fuel region. The observed tendency of decreasing IDT, easiness to ignite, for higher pressures and equivalence ratios, match quite well with the operational characteristics experienced by the jet fuel in a typical modern jet engine combustion chamber.

5.2 Laminar Flame Speed and Thermal Flame Thickness for Jet Fuels

The results of laminar flame speed and thermal flame thickness for Jet A-1/air mixtures and for Jet A-1+HEFA Surrogate/air mixtures are now presented. Two different samples were tested: one sample of pure Brazilian commercial Jet A-1 and the second sample is a mixture 50% in volume between the same Jet A-1 and 50% of a surrogate of HEFA kerosene type fuel. The surrogate composition was 80% of n-dodecane and 20% of iso-octane, as described in section 1.3.

Figure 5.18 shows a comparison of the laminar flame speed results of the Jet A-1 described in Table 1.2 and results reported by (Vukadinovic, Habisreuther, & Zarzalis, 2013). The results of (Vukadinovic et al., 2013) were obtained with a CVR and methods similar as those employed in this work, using a cubic stainless steel reactor with inner volume of 2.28 liters. The flame was assessed using the Mie-scattering laser light method. Also shown, are results obtained using a German Jet A sample, in the way to compare directly the results between Jet A-1 and Jet A/air mixtures. The composition and properties of the German Jet A sample was taken as published by (Subith S. Vasu et al., 2008). It is possible to observe in Figure 5.18 the results of Jet A-1 and Jet A are very close. The results presented by (Vukadinovic et al., 2013) were obtained at higher temperature.

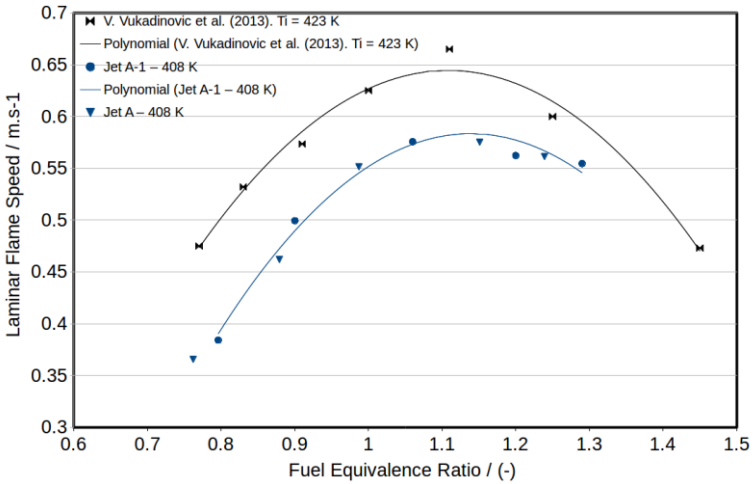

Figure 5.18–Laminar flame speed of air mixtures with Jet fuels, initial pressure of 1 bar. Laminar CVR experiments.

Figure 5.19 show the results comparing the use of pure Jet A-1 and its mixture with the HEFA surrogate that was described in section 1.3. In the way to guide the eyes and facilitate the results comparison, two lines obtained through 5th polynomial fitting, were employed.
There is a clear increase in the laminar flame speed of the HEFA mixtures, for all the covered fuel equivalence ratio. This increasing is about 5 and 7%, which is indeed a noticeable difference and must be take into account in the jet fuels performance analysis.

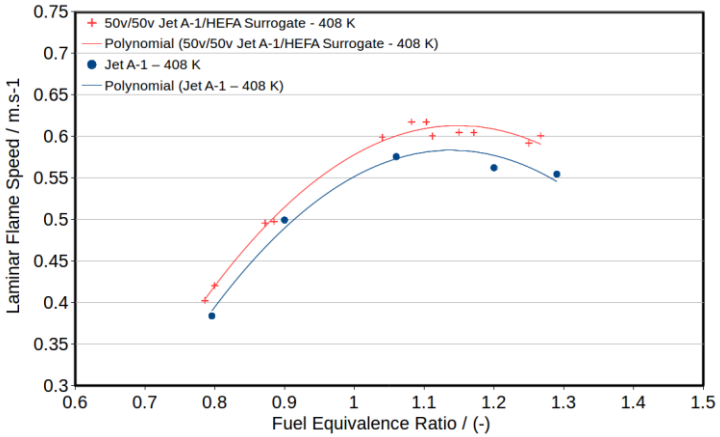

Figure 5.19– Laminar flame speed of air mixtures with Jet fuels, initial pressure of 1 bar. Laminar CVR experiments. HEFA surrogate comparison.

Figure 5.20 shows results of flame thickness, calculated using equation 3.6. It is possible to observe the HEFA surrogate presented a thinner flame thickness, compared with the pure Jet A-1, for all the covered fuel equivalence ratio.

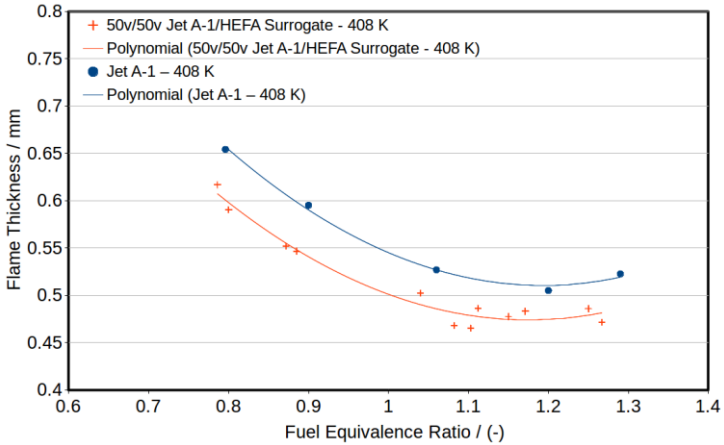

Figure 5.20– Thermal flame thickness of air mixtures with Jet fuels, initial pressure of 1 bar. Laminar CVR experiments. HEFA surrogate comparison.

It is possible to use information from the CVR Flame code, related to the reactant gaseous mixture, to predict the flame propagation behavior. Considering the jet fuels mixtures, Figure 5.21 and Figure 5.22 show the flame expansion factor and the thermal diffusivity. The flame expansion factor is the quotient between the specific volume of the burned products and unburned reactants.

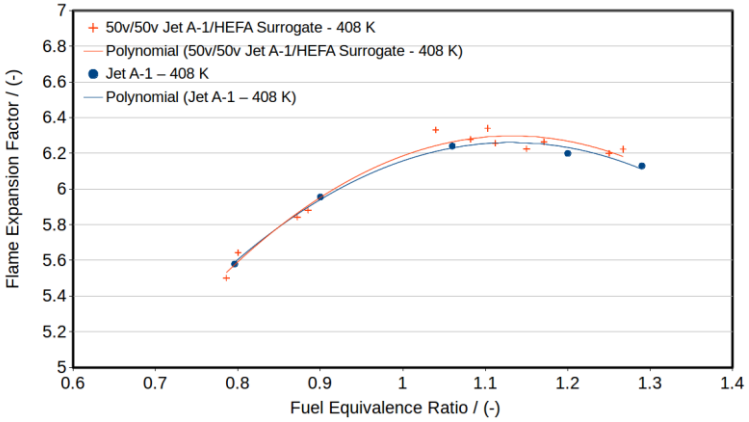

Figure 5.21– Flame expansion factor of jet fuels/air mixtures, initial temperature of 408 K and pressure of 1 bar.

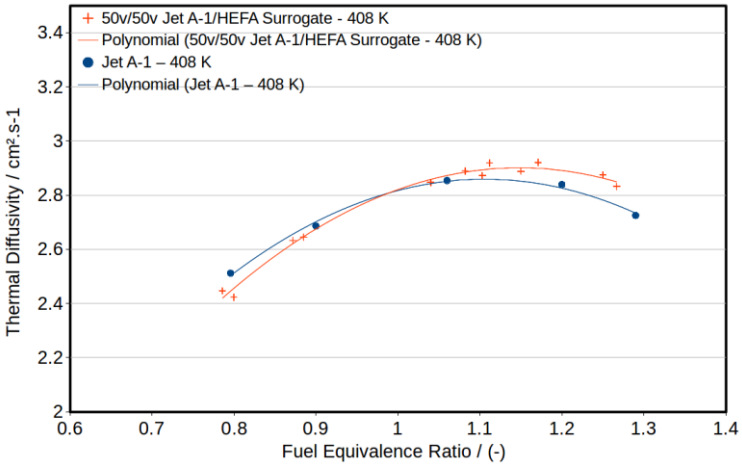

Figure 5.22– Heat diffusivity of jet fuels/air mixtures, initial temperature of 408 K and pressure of 1 bar.

It is possible to observe the flame expansion factor and the thermal diffusivity are almost the same for the pure Jet A-1 and its mixtures with the HEFA surrogate. However, the laminar flame speed is from 5% to 7% higher for the Jet A-1+HEFA than for the pure Jet A-1. Figure 5.23 shows results of the laminar flame speed for n-dodecane/air mixtures, at similar conditions presented in this work.

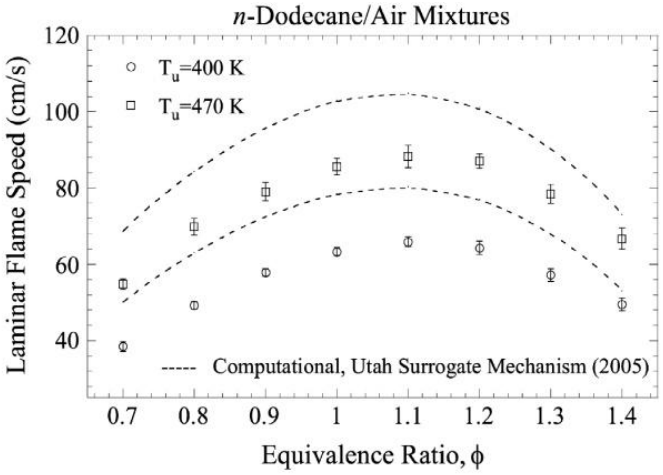

Figure 5.23–Laminar flame speed of n-dodecane air mixtures, initial pressure of 1 bar. Adapted from (Kumar & Sung, 2007).

It is possible to see the laminar flame speed of n-dodecane at 400 K is higher than the laminar flame speed of pure Jet A-1/air mixtures, at 408 K, comparing with the results showed in Figure 5.19. Thus, the addition of n-dodecane through the use of the HEFA surrogate, is expected to increase the laminar flame speed of the jet fuel, as indeed occurred and was observed in Figure 5.19.

5.3 Turbulent Flame Speed

This section presents the results of turbulent flame speed for Jet A-1/air mixtures and for Jet A-1+HEFA Surrogate/air mixtures. The methodology consisted in measuring the turbulent flame speed of methane/air, iso-octane/air and n-heptane/air mixtures under different intensities of the turbulent field. The results were then used to build a direct mathematical relationship to predict the turbulent flame speed under different levels of turbulent field intensity. The results presented in this section were obtained using the turbulent CVR described in section 4.2.2, post processed using the CVR Flame Code. In the context of the model used in the CVR flame code, the turbulent burning velocity is assumed as the velocity of a thin turbulent flame brush.

5.3.1 Turbulent Flame Speed for Pure Species

Figure 5.24 shows the results for the turbulent flame speed of methane/air mixtures under different turbulent RMS velocities u' at initial pressure and temperature of 300 K and 1 bar respectively.

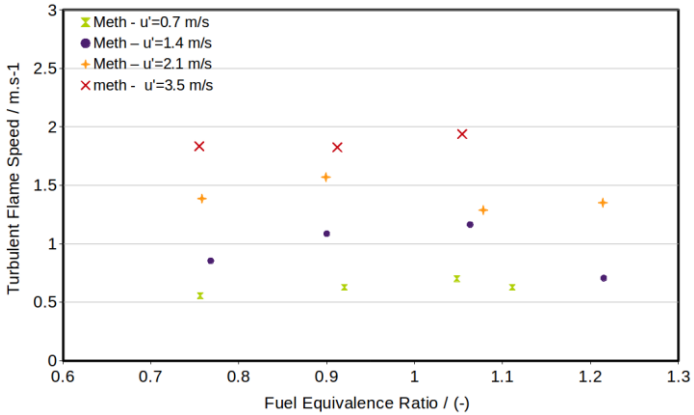

Figure 5.24–Turbulent Flame Speed of methane/air mixtures, temperature of 300 K and initial pressure of 1 bar. The experiments were carried out using the turbulent CVR.

The measurements are strongly dependent on the velocity fluctuation and weakly dependent on equivalence ratio. The small number of measurements does not allow to evaluate the standard deviation of the data around the mean.

Following the discussion in section 3.3, a predictive model is curve fitted to all measurements. Figure 5.25 presents the measurements for methane, iso-octane and n-heptane/air mixtures and the continuous line, which was the curve-fit using the proposed model.

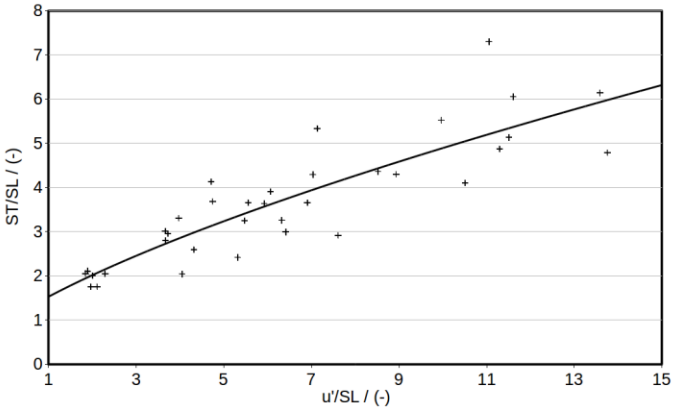

Figure 5.25– Dimensionless turbulent flame speed of methane, iso-octane and n-heptane/air mixtures as function of the turbulent intensity u'/SL. In the vertical axis, ST means turbulent flame speed and SL laminar flame speed. The observed line is a power law fitting curve. The results of turbulent flame speed, were obtained using the turbulent CVR Turbulent.

The modeled equation is repeated here as,

$$\frac{S_T}{S_L} = 1 + A\left(\frac{u'}{S_L}\right)^B \tag{5.3}$$

where S_T is the turbulent flame speed, S_L is the laminar flame speed, u' velocity fluctuation of the turbulent field, A and B are the model constants. Table 5.3 shows the values of the curve-fitted constants.

Table 5.3 - Constants fitted to the equation 51.

	Units	Value
A	(-)	0.6113 ± 0.1244
B	(-)	0.8027 ± 0.0934

The curve-fitting covers the entire range within the uncertainty of the measurements.

5.3.2 Estimate of Turbulent Flame Speed for Jet A-1 and Jet A-1 Surrogate/Air Mixtures

The turbulent flame speed for Jet A-1 and the 50%/50% v/v Jet A-1 + HEFA Surrogates mixtures with air were not directly measured in the turbulent CVR. The reason was the difficulty in promoting complete evaporation in the available experimental set-up.
Instead, the laminar flame speed was measured in the laminar CVR and the correlation measured for the pure species was used to estimate the turbulent velocities for the Jet A-1 and Jet A-1+HEFA fuels. Table 5.4 presents the measured values of laminar flame speed and thermal flame thickness, as already presented in section 5.2.

Table 5.4- Laminar Flame speed and thermal flame thickness of Jet A-1 and Jet A-1 + HEFA surrogate mixture.

Phi	Jet A-1		Jet A-1 + HEFA Surrogate	
	$S_L/m.s-1$	l_0^D/mm	$S_L/m.s-1$	l_0^D/mm
0.85	0.45	0.62	0.47	0.57
0.95	0.52	0.57	0.55	0.52
1.05	0.57	0.53	0.60	0.49
1.15	0.58	0.51	0.61	0.47
1.25	0.56	0.51	0.60	0.48
1.35	0.51	0.53	0.55	0.50

Figure 5.26 shows the predicted values of the turbulent flame speed for Jet A-1 and 50%/50% v/v Jet A-1 + HEFA Surrogates mixtures with air. The curves were grouped considering the turbulent RMS field velocity u' that can be set in the turbulent CVR experiments. **Erro! Fonte de referência não encontrada.** was based in Figure 5.26, the difference is on horizontal axis which is now the fuel equivalence ratio.

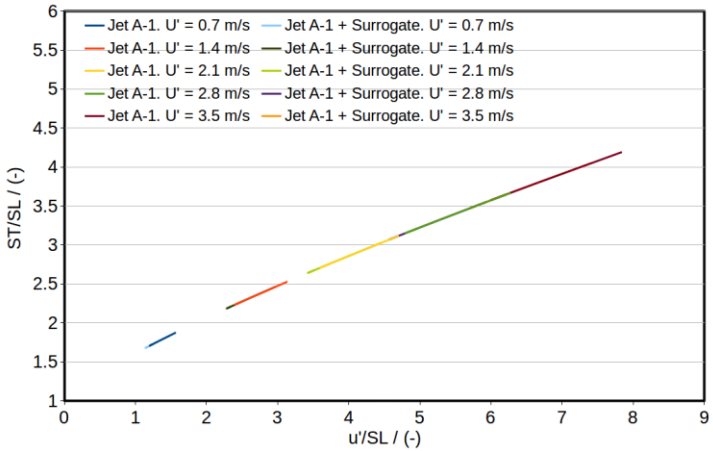

Figure 5.26– Predicted dimensionless turbulent flame speed of Jet fuels/air mixtures as function of the turbulence intensity.

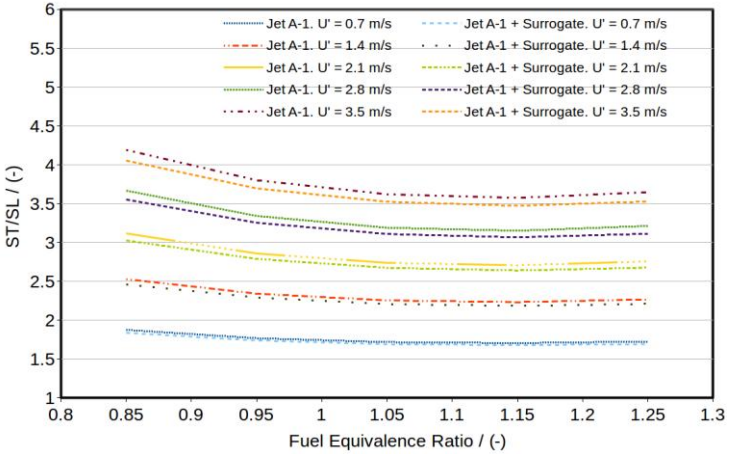

Figure 5.27– Predicted dimensionless turbulent flame speed of Jet fuels/air mixtures as function of the fuel equivalence ratio. In the vertical axis, ST means turbulent flame speed and SL laminar flame speed.

Figure 5.28 presents the turbulent flame speed of Jet fuels/air mixtures as function of the fuel equivalence ratio and turbulent RMS field velocity *u'*.

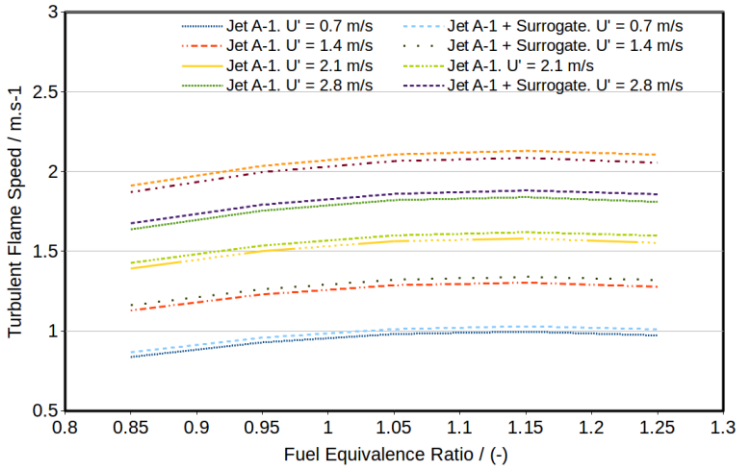

Figure 5.28– Predicted turbulent flame speed of Jet fuels/air mixtures as function of the fuel equivalence ratio and turbulent RMS field velocity u'.

It is possible to see in Figure 5.28 the predicted turbulent flame speed for the HEFA surrogate mixture is always higher, for all the spanned turbulent intensity and equivalence ratio. Figure 5.29 presents the calculated percentage increasing of the flame speed with addition of the HEFA surrogate. There are shown results of laminar experiments and results obtained using the predictive curves from Figure 5.28.

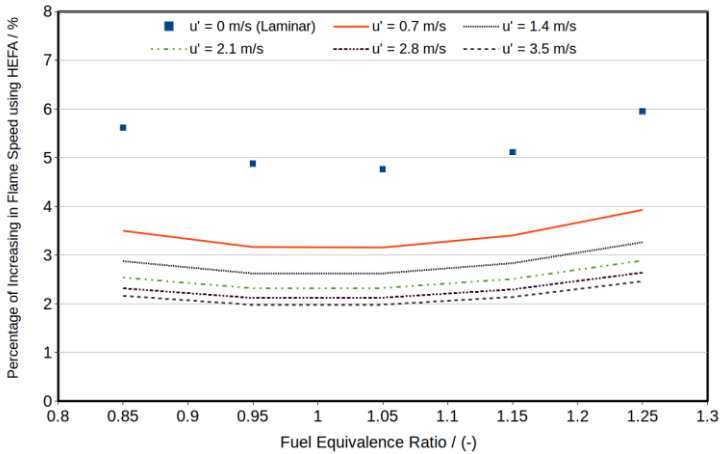

Figure 5.29– Percentage increasing in flame speed when the addition of HEFA surrogate.

It is possible to see the flame speed increasing is lower for stoichiometric mixtures and is higher for both leaner and rich mixtures. It is remarkable that higher the turbulence is, lower is the percentage increase, and the difference approaches an asymptotic level as turbulent RMS fluctuations approach to 3.5 m/s. The effect of chemical kinetics in the laminar flame speed was supplanted by the turbulence. Higher the turbulence, lower the difference will be, until some limit where the increasing of the turbulence will not affect the percentage difference, which stabilizes around 2%.

Considering the primary and the secondary zones of the combustion chamber, a higher turbulent flame speed will be helpful, as the total amount of the fuel can be burned faster. Thus, the exhaust gases will be cleaner and the radial temperature distribution in the outlet combustion chamber will be more homogeneous. This is favorable to a longer lifetime of turbine components, blades and guide vanes, protecting them from thermal stress and damages, as is desirable for a good overall performance of the jet engine (Bauer, 2013, 2014; Boyce, 2002). It is noticeable that the HEFA surrogate mixtures present slightly higher turbulent flame speed when compared with the pure Jet A-1 mixtures, but within the uncertainty of the estimates. Although the laminar flame speed for the Jet A-1+HEFA surrogate is 5% to 7% higher than pure Jet A-1, the effect of turbulence tends to decrease the relative difference to about 2%.
The tests here were conducted at 1 bar and 408 K. However, modern jet engine combustion chamber works under higher pressure and higher temperatures. The experiments carried out using the both laminar and turbulent CVR, can provide a burning velocity profile, as function of time, flame radius, and unburned gas temperature or pressure. Figure 5.30 shows the burning velocity profile as function of pressure and unburned gases temperature, for Jet A-1 and Jet A-1 + HEFA surrogate mixtures, measured in the laminar CVR. The temperature and pressure conditions displayed in these curves are closer to the real jet engine combustion chamber conditions.

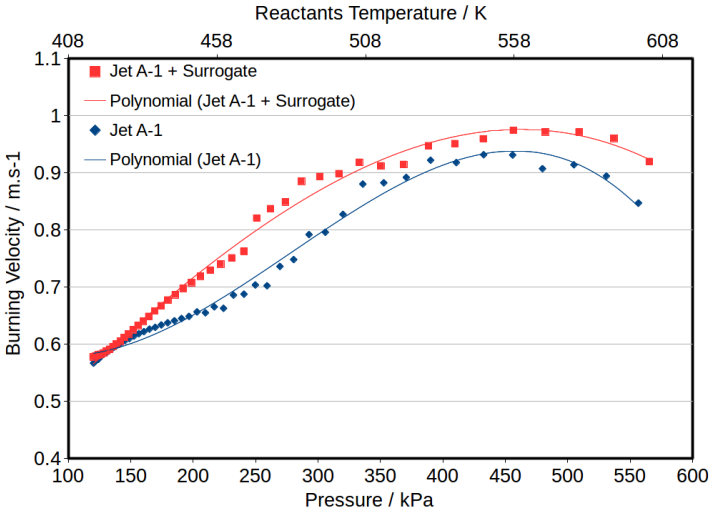

Figure 5.30– Burning velocity profiles for Jet A-1 and 50% (v/v) Jet A-1 + HEFA Surrogates mixtures with air, phi = 1.06, Ti = 408 K, pi = 1 bar, obtained with the laminar CVR. The flames reach the walls of the reactor at pressures around 450 kPa, when the curves start to decrease.

It is possible to see the HEFA surrogate mixture presents a higher burning velocity through all the pressure and temperature of interest.
The consideration of the actual operational conditions of the modern jet engines should also include the effect of the turbulence flow field within it. Figure 5.31 presents the region of the current turbulent conditions used in the experiments of turbulent flame speed and flame kernel extinguishment in the Borghi diagram. The conditions used are close to the conditions reported by (Gomez, 2011) as pertaining to combustion in gas turbines, thus being adequate to extract preliminary conclusions. Experiments at higher turbulent conditions are needed, but are beyond the capabilities of the experimental set-up used in this work.

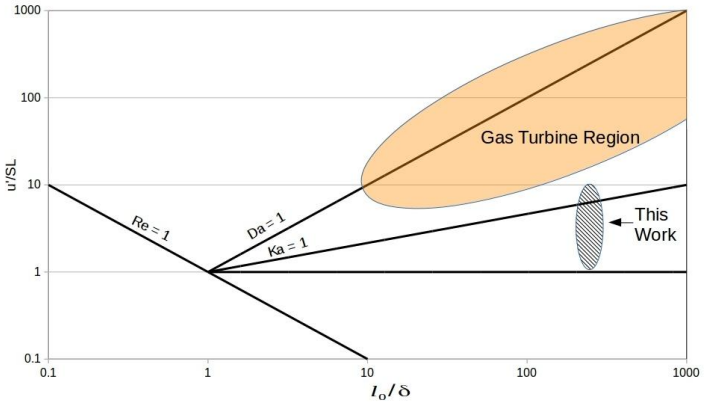

Figure 5.31– Borghi diagram adapted to show the results obtained in this work. The Gas Turbine Region filled in orange was adapted from (Gomez, 2011).

5.4 Flame Laminar Lean Flammability Limit

Laminar lean flammability limit for Jet A-1and for Jet A-1+HEFA Surrogate/air mixtures where determined using spark ignition in the laminar CVR, as described in section 4.2.3. The equivalence ratio range was varied from 0.7 to 0.8. Figure 5.32 and Figure 5.33 show two different flame radius sequences, photographed using the Schlieren system, for Jet A-1/air mixtures. The picture sequence starts with the spark, making the pictures at 1 ms brighter due the presence of the spark.

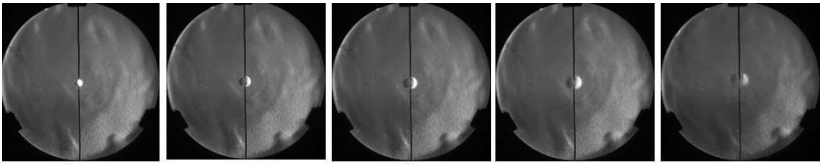

Figure 5.32– Flame radius sequence photographed using the Schlieren system. Jet A-1/air mixtures at initial temperature and pressure of 408 K and 1 bar respectively. In this experimental shot flame propagation was no detected, the mixture was considered not-flammable.

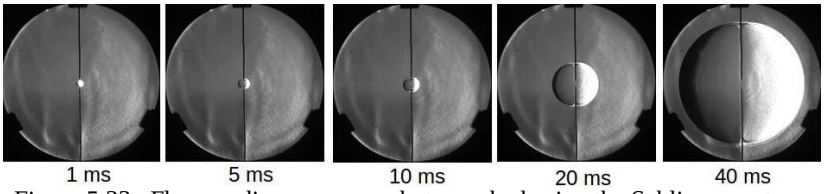

Figure 5.33– Flame radius sequence photographed using the Schlieren system. Jet A-1/air mixtures at initial temperature and pressure of 408 K and 1 bar respectively. In this experimental shot flame propagation was detected, the mixture was considered flammable.

The figures illustrate the difference between flammable and non-flammable mixtures. For the non-flammable mixture the flame kernel remains visible up to 50 ms.

5.4.2 Laminar Lean Flammability Limit for Jet A-1 and Jet A-1 Surrogate/Air Mixtures

Figure 5.34 shows the laminar lean flammability limit for Jet A-1 and Jet A-1 surrogate/air mixtures, as function of the spark energy and fuel equivalence ratio. Figure 5.35 shows the results of the cumulative density function - CDF, calculated using Equation 3.4.

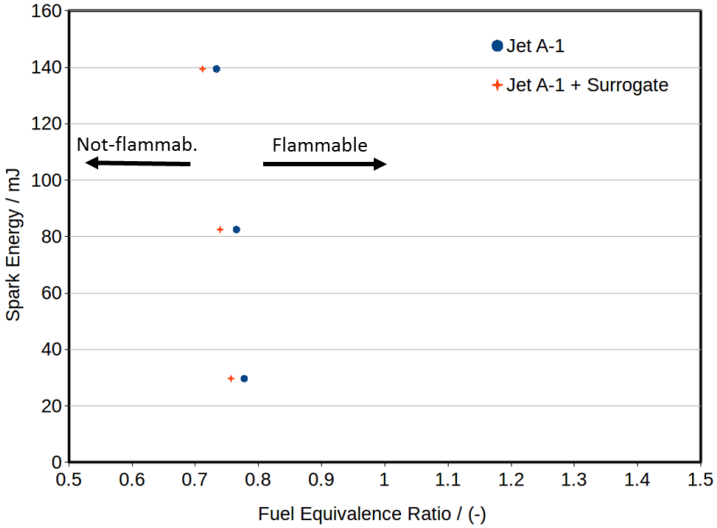

Figure 5.34– Lean Laminar flammability limit for Jet A-1 and Jet A-1 HEFA surrogate mixtures with air at 1 bar and 408 K.

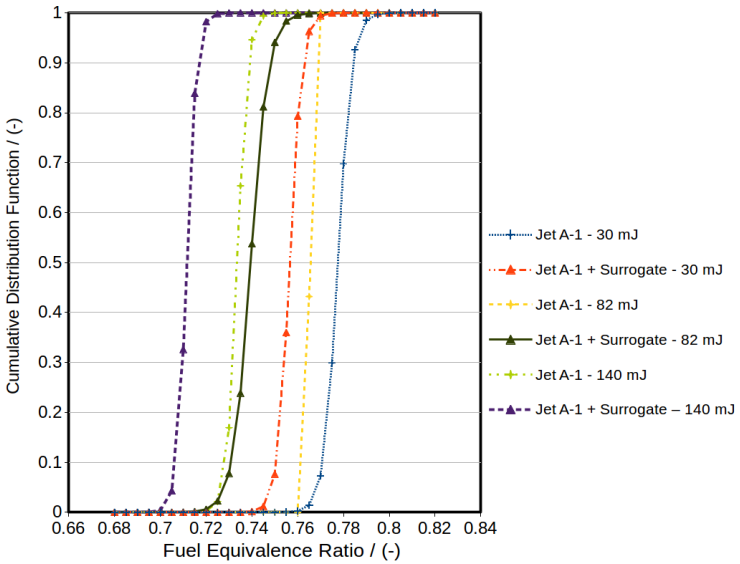

Figure 5.35– Cumulative Distribution Function applied to calculate lean laminar lean flammability limit of Jet A-1 and Jet A-1 HEFA surrogate mixtures with air at 1 bar and 408 K. It is shown a narrow equivalence ratio scale.

The results shown in Figure 5.34 has the same scale as the Figure 3.4, which shows the methane ignitibility curve and flammability limits. The use of same equivalence ratio scale allows to infer that the results in Figure 5.34 are in the higher ignitibility curve region, tending to the asymptote. This confirms the reported results are indeed the lean flammability limits, as discussed in section 3.1. Figure 5.36 shows the zoomed results of lean laminar flammability limits, focusing in the lean region.

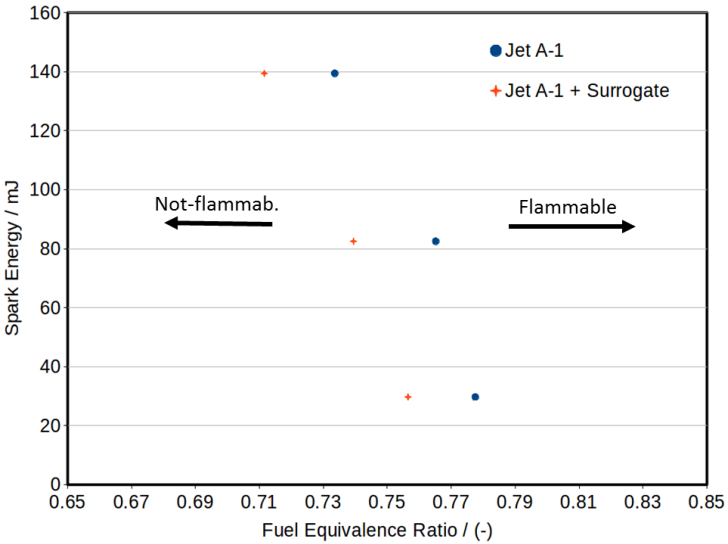

Figure 5.36– Lean laminar flammability limits for Jet fuels mixtures. Ti = 408 K, pi = 1 bar.

It is possible to observe in Figure 5.36 the addition of the HEFA surrogate shifted the flammability limit to the leaner side in about 3 – 4%. This is indeed a positive effect for the ignition of the mixture in the primary zone of the combustion chamber of the jet engine for an eventual relight process. The observation of Figure 5.34 and Figure 5.35 allows to conclude that the use of the HEFA surrogate widened the lean laminar flammability limit, i. e., the HEFA surrogate mixtures are more flammable. Table 5.5 summarizes the results for Jet A-1 and Jet A-1 + HEFA surrogate/air mixtures.

Table 5.5 – Results of lean laminar flammability limits for Jet fuels mixtures. Ti = 408 K, pi = 1 bar.

	Jet A-1	Jet A-1 + HEFA Surrogate
Fuel Equivalence Ratio	0.73	0.71

5.5 Turbulent Lean Extinguishment

Figure 5.37 presents lean turbulent flame kernel extinction limits of methane, isooctane and ethanol/air mixtures. The methodology was described in section 4.2.4.

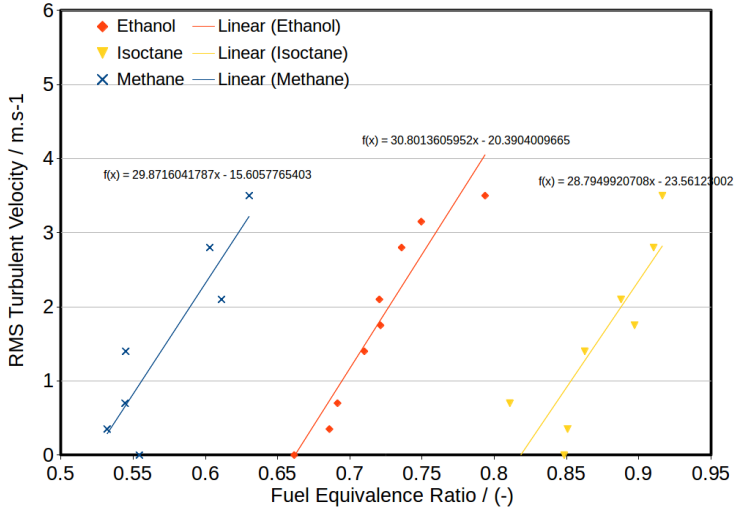

Figure 5.37– Lean turbulent flame kernel extinction limit of ethanol, iso-octane and methane/air mixtures at temperature of 305 K and 1 bar of initial pressure. The results were obtained using the turbulent CVR. There are also shown, the linear fitting applied to each experimental sequence and its respective equation.

The results present a linear behavior with linear coefficient of 29.87, 30.80 and 28.79 for methane, ethanol and iso-octane respectively, with average of 29.822. The detailed chemical kinetics mechanisms are different for the three species (Cancino, Fikri, Oliveira, & Schulz, 2009; Curran et al., 1998; Glassman & Yetter, 2008; Turns, 2012; Warnatz et al., 2006). However, the slope of the turbulent extinguishment limit is similar for the fuels. Possibly, this conclusion may be extended to jet fuel mixtures, considering the turbulence range covered in this study. A quick estimate can be done using a linear relationship, as follows,

$$\Phi_2 = \frac{(u_2^{'} - u_1^{'})}{B_{turb}} + \Phi_1 \qquad (5.4)$$

where the subscript 2 refers to the target turbulent condition and the subscript 1 refers to the laminar condition and B_{turb} is the average linear

coefficient obtained from the Figure 5.37. Taking this average linear coefficient from Figure 5.37, the lean laminar flammability limit of the HEFA surrogate mixture as 0.7115, using a RMS turbulent flow velocity of 3.5 m/s, the estimated lean turbulent flame kernel extinction limit of the Jet A-1 + HEFA Surrogate mixture is approximately 0.83. This result is about 17% higher than the lean laminar flammability limit. Comparing the influence on the flame speed, the turbulence has a quite strong influence on the flame kernel extinguishment.

6 CONCLUSION

This work intended to present a basic characterization of aspects related to the chemical composition of jet fuels as applied to modern jet engines. The selected combustion characteristics are the ignition delay time, the lean laminar flammability limit, the turbulent flame kernel extinguishment, the laminar, and turbulent flame speeds. In the following, the main conclusions for each set of measurements and analysis are summarized.

6.1 Ignition Delay Time

Ignition delay times for Jet A-1/air mixtures were measured using a heated rapid compression machine, at compressed pressures of 7, 8 and 15 bar, post-compression temperatures ranging from 630 to 895 K and equivalence ratios varying from 0.3 to 1.3.

The procedure for the Jet A-1 and HEFA surrogate vaporization and mixture formation on the RCM facility worked adequately in the conditions tested. The design and construction of the facility for the Jet fuel mixture preparation was one of the most time demanding tasks. The lack of accurate Jet A-1 vapor pressure curve as function of temperature was one of the main reason for this time demand.

In general, the results showed the expected trend of decreasing the IDT with the increase of pressure and temperature. For the equivalence ratio, it was observed a decrease in IDT with the increase in the equivalence ratio from 0.7 to 1.3. Considering the primary zone of the combustion chamber, which works at rich conditions for almost all the operational regimes, this is an advantageous result. The measurements revealed the existence of NTC in the range between 700 K and 850 K. This phenomenon may influence relight conditions at low temperature.

The IDT for the Jet A-1-HEFA surrogate was not measured due to difficulties in evaporation of the fuel. However, since the HEFA Surrogate studied in this work is composed by 80% of n-dodecane, it is expected that the mixture Jet A-1 + HEFA Surrogate will ignite faster when compared with the pure Jet A-1 air mixtures. Furthermore, the surrogate mixture of 80% of n-dodecane and 20% of iso-octane is expected to have a less pronounced NTC when compared to pure n-dodecane, thus providing a smoother ignition delay curve of the HEFA surrogate combustion.

6.2 Lean laminar flammability limit

The addition of the HEFA surrogate broadened the lean laminar flammability limit, shifting the flammability limit to the leaner side in about 3 – 4%. This is a good result in terms of fuel consumption, since it points to a reduction in unburned hydrocarbons in the engine. However, the main positive effect is to turn the mixture more flammable. This is a positive effect for the ignition of the mixture in the primary zone of the combustion chamber and for an eventual relight process.
The results obtained for the lean laminar flammability limit are in good agreement with the results of the ignition delay times obtained with the rapid compression machine. As just discussed, the addition of a high amount of n-dodecane present in the HEFA surrogate showed the tendency to decrease the ignition delay time, speeding up the energy releasing process in the early stages of flame kernel formation. This will facilitate the flame kernel stabilization and development to a flame propagation. Therefore the HEFA surrogate mixture is more ignitable and more flammable, having a positive effect in the ignition and flame propagation inside of the jet engine combustion chamber.

6.3 Lean turbulent flame kernel extinction limit

Turbulence acts to narrow the lean flammability limits due to the flame kernel extinguishment. A linear relationship of extinguishment and turbulence was obtained. An estimate indicated the lean turbulent flame kernel extinction limit of the Jet A-1 + HEFA Surrogate mixture in the conditions of the turbulent CVR is about 17% higher than the lean laminar flammability limit. Turbulence has a positive effect on the atomization process and mixture formation in the combustion chamber (Boyce, 2002). The favorable results of ignition delay times and lean laminar flammability limits obtained with the HEFA Surrogate mixture are positive in the direction of operation with higher turbulence. The results of lean turbulent flame kernel extinction limit indicates that the HEFA surrogate mixture is also more stable at turbulent conditions.

6.4 Laminar and turbulent flame speeds

The development, tests and validation of the CVR Flame Code was one of the core development activities. The analysis of the pressure transient curve provides a host of characteristics, such as the laminar flame speed and thermal flame thickness, the flame expansion factor, the total work done by the flame and the burning velocity profiles for higher

temperatures/pressures, and the global activation energy, as well as, all the averaged thermodynamic properties of the reactants and burned products are calculated. Therefore, it is possible to perform further thermodynamic analysis applied to the measured flame propagation.
The results of the laminar and turbulent flame speeds showed that the addition of the HEFA surrogates enhanced the burning rates. The laminar flame speed of the Jet A-1+HEFA surrogate was from 5% to 7% higher than that of pure Jet A-1. However, the increase in the turbulent burning rate is lower, about 2% for higher turbulent fields (u' = 3.5 m/s). The conditions used here are close to the conditions reported by (Gomez, 2011) in the Borghi diagram as pertaining to combustion in gas turbines, being adequate to extract preliminary conclusions. Experiments at higher turbulent conditions are needed, but are beyond the capabilities of the experimental set-up used in this work.

6.5 Lean Blow-off

(Zhang, Noble, Meyers, Xu, & Lieuwen, 2005) showed that if the Damköhler number is larger than a critical value, the blow-off will be avoided. Basically, if the flow time remains the same, the decrease of the chemical time will increase the Damköhler number, having a positive effect in avoiding lean blow-off. As showed above, the addition of the HEFA surrogate mixture tends to decrease the ignition delay time and increase the turbulent burning velocity. In the both cases, the chemical time will decrease. The experimental results of the ignition delay time, laminar and turbulent flame speeds indicated that the addition of 50% of the HEFA surrogate to the Jet A-1 will improve the stability of the flame, being favorable to avoid the lean blow-off phenomenon.

(Bergthorson & Thomson, 2015) reported a comprehensive review on alternative fuels and design for thermal machines, including jet engines. Figure 6.1 shows a rendering of an alternative design for futures machines. The main difference to current designs is that the newer one does not present a fuel rich primary region. In this new design, the fuel is injected through two flows, both of them being lean premixed mixtures. Using this strategy, the flame temperature is reduced, decreasing the NOx emissions. Additionally, the lean mixture will produce less soot, CO and unburned hydrocarbons. (Bergthorson & Thomson, 2015) suggested that, for this new lean premixed configuration, the ignition will play a key role. Mixture with easy

ignitable fractions, like n-dodecane, will be preferable, turning the machine operation more safe, reliable and efficient. The addition of 50% of the HEFA surrogate to the Jet A-1 may also improve the fuel performance considering the future alternative design of the jet engine combustion chamber.

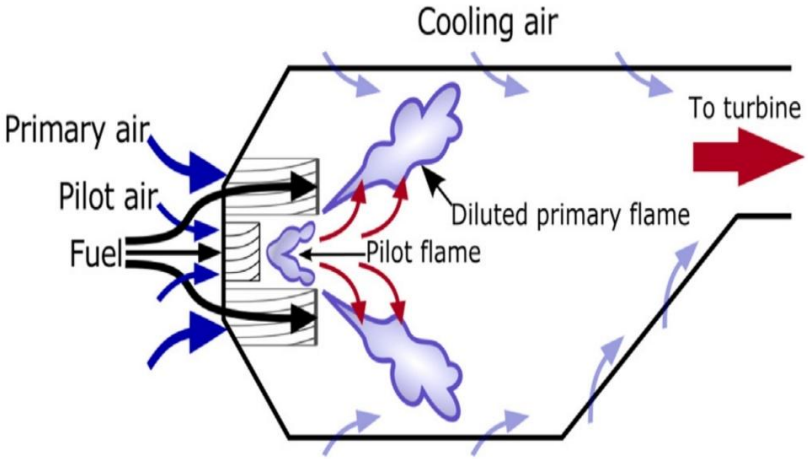

Figure 6.1– Alternative Design for Future Jet Engines Combustion Chamber. Adapted from (Bergthorson & Thomson, 2015).

6.6 Suggestions for future work

Based on the results and discussions, some future activities are now suggested.

- Perform ignition delay measurements for the Jet A-1 + HEFA surrogate mixtures in the ITT/RCM facility. Last time improvements in the mixture preparation and chamber heating may allow for these experiments.
- Perform lean turbulent flame kernel extinction limit measurements for pentyne (C_5H_8) mixtures, using the turbulent CVR at ITT/KIT. This experiments could be used in comparison with the conclusions gained with the Jet A-1 and Jet A-1 + HEFA surrogate mixtures results in terms of the lean laminar flammability limits.
- Perform additional measurements for turbulent burning velocities with pentyne/air mixtures, using the turbulent CVR at ITT/KIT. This results could be used to compare the turbulent

burning velocity model with larger Damköhler numbers.

- Perform a chromatographic analysis to the Jet A-1 sample in order to have a more realistic view of its composition and to measure the specific heat at constant pressure, specific enthalpy and specific entropy of the Jet A-1 sample, in the framework of the JANAF results, as described by (Gordon & McBride, 1994). This should to improve the accuracy of the results obtained using the CVR Flame Code.
- Propose a simplified surrogate comprising up to 5 components (considering iso-octane and n-dodecane) to fit the obtained results of ignition delay time, lean flammability limit and laminar flame speed of the studied Jet A-1 sample. Apply a detailed chemical reaction mechanism and model the kinetics for ignition delay times.

7 APPENDIX I – TXT FILES

The CVR experimental results are written in a txt type file. The output txt file is standardized, with two main regions: a head including all the experimental informations like the initial temperature, pressure, equivalence ratio, the atomic compositions of the fuel, the nitrogen-oxygen ratio of the oxidant, the number of experimental points and some additional informations needed by the code. The second region comprises the experimental results, organized in three standardized columns: the time in seconds, the pressure in kPa and the flame front radius measured by the Schlieren set up.

```
nheads    0025          !"Number of rows in the Head of this document."
npoints   0992          !"Number of experimental points."
ngrids    0100          !"Number of time steps. Input to the code."
schl_ti    0039          !"Initial time when the measured radius is at least 10 mm.
WARNING: time in ms !!
schl_tf      0207              !"Final time for the Schlieren radius measurement.
WARNING: time in ms !!
Ti          0408.09        !"Initial temperature. in K."
pi          0100.11        !"Initial pressure. in kPa."
phi         000.980        !"Equivalence ratio."
fuel        Jet-A(g)       !Fuel NAME.**
carbon      0011.53        !"Number of carbon atoms in the fuel."
hydrogen    0021.70        !"Number of hydrogen atoms in the fuel."
oxygen      0000.00        !"Number of oxygen atoms in the fuel."
N2_O2       0003.76        !"Molar ratio nitrogen/oxygen in the air"
expnumb     0748           !"Number of the experiment"
! The name of this file should be as follow: fuel_turb_Number.txt
!The fuel name should have four characters. the test number should have four.For
example isooctane:ioct_turb_0001.txt
! The first column is the time [s], the second is the ABSOLUT pressure [kPa] and
the third is the flame radius [m].
! The first column shall have at maximum five characters and four characters after
the comma. The second shall have
! at maximum nine characters and four characters after the comma. The third shall
have at maximum eight characters
! and six characters after the comma.
!**Fuel names: [isoctane=C8H18,isooctane], [n-heptane=C7H1,.n-heptane],
[ethanol=C2H5OH], [Hydrogen=H2].
!**Fuel names: [Methane=CH4], [Jet-A = Jet-A(g)] .
```

! ----------
-End of the Head.
0.0000 100.1100 0.001889
0.0001 100.4334 0.002470
0.0002 100.2717 0.002647
0.0003 100.4334 0.002731
0.0004 100.2717 0.002845
0.0005 100.1100 0.003002
0.0006 099.9483 0.003179
0.0007 100.2717 0.003410
0.0008 100.2717 0.003588
0.0009 100.2717 0.003684
0.0010 100.1100 0.003853
0.0011 100.2717 0.004009
0.0012 100.2717 0.004176
0.0013 100.2717 0.004512
0.0014 100.4334 0.004682
.
.
.
.
.
!End of file.

8 APPENDIX II – CVR FLAME CODE FLOWCHART

Figure 8.1 shows a flowchart of the CVR Flame Code, as described in the section **Erro! Indicador não definido.**. The name "CEA2" is the nomenclature assigned to the chemical equilibrium code used to obtain the thermodynamic properties.

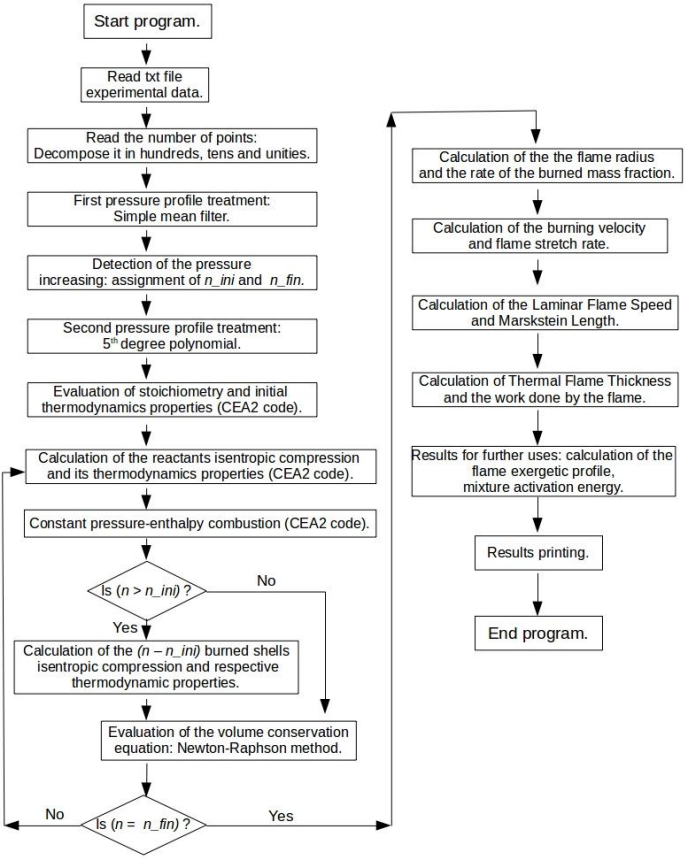

Figure 8.1– Simplified flowchart of the CVR Flame Code.

9 REFERENCES

Anderson, B. E., Beyersdorf, a. J., Hudgins, C. H., Plant, J. V., Thornhill, K. L., Winstead, E. L., … Bhargava, a. (2011). *Alternative Aviation Fuel Experiment (AAFEX)*. Retrieved from http://hdl.handle.net/2060/20110007202

Andrews, G. E., & Bradley, D. (1972). Determination of Burning Velocities: A Critical Review. *Combustion and Flame*, *18*, 133–153.

ASTM International. (2014). Standard Specification for Aviation Turbine Fuel Containing Synthesized Hydrocarbons D7566-14a, 1–27. http://doi.org/10.1520/D7566-14a.components

Bacha, J., Barnes, F., Franklin, M., Gibbs, L., Hemighaus, G., Hogue, N., … Company, C. P. (2006). Chevron Aviation Fuels Technical Review. *Aviation*.

Bane, S. P. M. (2010). Spark Ignition : Experimental and Numerical Investigation With Application to Aviation Safety Thesis by, *2010*.

Battin-Leclerc, F. (2008). Detailed chemical kinetic models for the low-temperature combustion of hydrocarbons with application to gasoline and diesel fuel surrogates. *Progress in Energy and Combustion Science*, *34*, 440–498. http://doi.org/10.1016/j.pecs.2007.10.002

Bauer, H.-J. (2013). Thermal Turbomachines I. Karslruhe - Germany. Retrieved from www.its.kit.edu

Bauer, H.-J. (2014). Thermal Turbomachines II. Karlsruhe - Germany. Retrieved from www.its.kit.edu

Beeckmann, J., Chaumeix, N., Dagaut, P., Dayma, G., Egolfopoulos, F., & Foucher, F. (2013). Collaborative Study for Accurate Measurements of Laminar Burning Velocity, 1–6.

Bergmann, J. C., Tupinambá, D. D., Costa, O. Y. a, Almeida, J. R. M., Barreto, C. C., & Quirino, B. F. (2013). Biodiesel production in Brazil and alternative biomass feedstocks. *Renewable and Sustainable Energy Reviews*, *21*, 411–420. http://doi.org/10.1016/j.rser.2012.12.058

Bergthorson, J. M., & Thomson, M. J. (2015). A review of the combustion and emissions properties of advanced transportation biofuels and their impact on existing and future engines. *Renewable and Sustainable Energy Reviews*, *42*, 1393–1417. http://doi.org/10.1016/j.rser.2014.10.034

Bernard Lewis, G. von E. (1961). *Combustion, Flames and Explosion of*

Gases (Second). New York: Academic Press Inc.

Blakey, S., Rye, L., & Wilson, C. W. (2011). Aviation gas turbine alternative fuels: A review. *Proceedings of the Combustion Institute*, *33*(2), 2863–2885. http://doi.org/10.1016/j.proci.2010.09.011

Bonhomme, A., Selle, L., & Poinsot, T. (2013). Curvature and confinement effects for flame speed measurements in laminar spherical and cylindrical flames. *Combustion and Flame*, *160*(7), 1208–1214. http://doi.org/10.1016/j.combustflame.2013.02.003

Boyce, M. P. (2002). *GasTurbine Engineering Handbook*.

Bradley, D., Lawes, M., Liu, K., & Mansour, M. S. (2013). Measurements and correlations of turbulent burning velocities over wide ranges of fuels and elevated pressures. *Proceedings of the Combustion Institute*, *34*(1), 1519–1526. http://doi.org/10.1016/j.proci.2012.06.060

Bradley, D., Lawes, M., & Materego, M. (2015). Interpretation of Auto-ignition Delay Times Measured in Different Rapid Compression Machines. In *ICDERS 2015* (pp. 1–6). Leeds, England. Retrieved from icders2015.org

Cancino, L. R., Fikri, M., Oliveira, a. a M., & Schulz, C. (2009). Autoignition of gasoline surrogate mixtures at intermediate temperatures and high pressures: Experimental and numerical approaches. *Proceedings of the Combustion Institute*, *32 I*, 501–508. http://doi.org/10.1016/j.proci.2008.06.180

Coronado, C. J. R., Carvalho, J. a., Andrade, J. C., Cortez, E. V., Carvalho, F. S., Santos, J. C., & Mendiburu, A. Z. (2012). Flammability limits: A review with emphasis on ethanol for aeronautical applications and description of the experimental procedure. *Journal of Hazardous Materials*, *241-242*, 32–54. http://doi.org/10.1016/j.jhazmat.2012.09.035

Corporan, E., DeWitt, M. J., Belovich, V., Pawlik, R., Lynch, A. C., Gord, J. R., & Meyer, T. R. (2007). Emissions characteristics of a turbine engine and research combustor burning a Fischer-Tropsch jet fuel. *Energy and Fuels*, *21*(5), 2615–2626. http://doi.org/10.1021/ef070015j

Corporan, E., Edwards, T., Shafer, L., Dewitt, M. J., Klingshirn, C., Zabarnick, S., … Klein, J. (2011). Chemical, thermal stability, seal swell, and emissions studies of alternative jet fuels. *Energy and Fuels*, *25*(3), 955–966. http://doi.org/10.1021/ef101520v

Coward, H. F. and, & Jones, G. W. (1953). *Limits of Flammability of Gases and Vapors*. Washington DC.

Curran, H., Curran, H., Gaffuri, P., Gaffuri, P., Pitz, W. J., Pitz, W. J., … Westbrook, C. (1998). A Comprehensive Modeling Study of -Heptane Oxidation. *Combustion and Flame*, *114*(1-2), 149–177. http://doi.org/10.1016/S0010-2180(97)00282-4

Dagaut, P., & Cathonnet, M. (2006). The ignition, oxidation, and combustion of kerosene: A review of experimental and kinetic modeling. *Progress in Energy and Combustion Science*, *32*(1), 48–92. http://doi.org/10.1016/j.pecs.2005.10.003

Davis, S. G., & Law, C. K. (1998). Laminar flame speeds and oxidation kinetics of iso-octane-air and n-heptane-air flames. *Symposium (International) on Combustion*, *27*(1), 521–527. http://doi.org/10.1016/S0082-0784(98)80442-6

DeWitt, M. J., Corporan, E., Graham, J., & Minus, D. (2008). Effects of aromatic type and concentration in Fischer-Tropsch fuel on emissions production and material compatibility. *Energy and Fuels*, *22*(4), 2411–2418. http://doi.org/10.1021/ef8001179

Dry, M. E. (2002). The Fischer-Tropsch process: 1950-2000. *Catalysis Today*, *71*(3-4), 227–241. http://doi.org/10.1016/S0920-5861(01)00453-9

Edwards, T., Colket, M., Cernansky, N., Dryer, F., Egolfopoulos, F., Friend, D., … Williams, S. (2007). Development of an Experimental Database and Kinetic Models for Surrogate Jet Fuels. *45th AIAA Aerospace Sciences Meeting and Exhibit*, 1–21. http://doi.org/10.2514/6.2007-770

Egolfopoulos, F. N., Hansen, N., Ju, Y., Kohse-Höinghaus, K., Law, C. K., & Qi, F. (2014). Advances and challenges in laminar flame experiments and implications for combustion chemistry. *Progress in Energy and Combustion Science*, *43*, 36–67. http://doi.org/10.1016/j.pecs.2014.04.004 Review

EPE. (2015). *Brazilian Energy Balance - 2014*. Brasilia. Retrieved from https://ben.epe.gov.br/

Filipe Reis. (2011). Cenário para uma Aviação Sustentável - o Papel dos Biocombustíveis. São Jośe dos Campos/Brazil: Seminário Combustíveis Alternativos para Aviação/DCA-BR.

Filogonio, A. T. (2011). O uso de Combustíveis “Drop-in” na Aviação Comercial. São José dos Campos/Brasil: EMRAER.

Glassman, I., & Yetter, R. A. (2008). *Combustion*. (A. Press, Ed.) (Fourth). San Diego - USA.

Gomez, A. (2011). Highly Turbulent Counterflow Flames: A Laboratory-Scale Benchmark for Turbulent Combustion Studies. In T. C. Institute. (Ed.), *Technical Meeting of the Eastern States Section of the Combustion Institute. University of Connecticut.* (pp. 1–12). Storrs, Connecticut. Retrieved from http://www.eng.yale.edu/gomez-lab/research/pdf/ESCI11-InvitedGomez.pdf

Gordon, S., & McBride, B. J. (1994). *Computer Program for Calculation of Complex Chemical Equilibrium Compositions and Applications I. Analysis*.

Graham, J. L., Striebich, R. C., Myers, K. J., Minus, D. K., & Harrison, W. E. (2006). Swelling of nitrile rubber by selected aromatics blended in a synthetic jet fuel. *Energy and Fuels*, *20*(2), 759–765. http://doi.org/10.1021/ef050191x

Hartmann, E. M. (2014). *Instrumentação e Operacionalização de um Reator de Volume Constante para Medição de Velocidade de Chama Laminar*. UFSC. Retrieved from http://tede.ufsc.br/teses/PEMC1572-D.pdf

Hartmann, R. M. (2009). *Análise da Propagação de Chamas Pré-Misturadas em Reator de Volume Constante*.

Hartmann, R. M., Schiessl, R., Oliveira, A. A. M., & Maas, U. (2014). *Extinction limits in atmospheric turbulent lean CH4 and C2H5OH/air mixtures*. San Francisco - USA.

Hopkinson, B. (1906). Explosions of Coal-Gas and AIr. *Proceedings of the Royal Society of London*, *77*(518), 387–413. Retrieved from http://www.jstor.org/stable/92806

Huber, G. W., Iborra, S., & Corma, A. (2006). Synthesis of transportation fuels from biomass: Chemistry, catalysts, and engineering. *Chemical Reviews*, *106*(9), 4044–4098. http://doi.org/10.1021/cr068360d

Kolmogorov, A. N. (1941). The Local Structure of Turbulence in Incompressible Viscous Fluid for very Large Reynolds Numbers. Retrieved from http://www.astro.puc.cl/~rparra/tools/PAPERS/kolmogorov_1951.pdf

Kumar, K., & Sung, C. (2007). Laminar flame speeds and extinction limits of preheated. *Combustion and Flame*, *151*, 209–224. http://doi.org/10.1016/j.combustflame.2007.05.002

Kumar, K., & Sung, C. J. (2010). A comparative experimental study of the autoignition characteristics of alternative and conventional jet fuel/oxidizer mixtures. *Fuel*, *89*(10), 2853–2863. http://doi.org/10.1016/j.fuel.2010.05.021

Langley, H. J. (1963). *A Reliability Test Method for "One-Shot" Items*. *US Defense Technical Information Center*.

Law, C. K., & Sung, C. J. (2000). Structure, aerodynamics, and geometry of premixed flamelets. *Progress in Energy and Combustion Science*, *26*(4), 459–505. http://doi.org/10.1016/S0360-1285(00)00018-6

Law, C. K., & Wu, C. K. (1984). On the determination of laminar flame speeds from stretched flames. In *Twentieth Symposium (International) on Combustion/The Combustion Institute* (pp. 1941–1949).

Lee, D., & Hochgreb, S. (1998). Rapid Compression Machines : Heat Transfer and Suppression of Corner Vortex. *Combustion and Flame*, *114*(3), 531–545.

Lindenmaier, S. (2002). *Zeitaufgelöste Laser-diagnostische Untersuchung der Funkenzündung*. University of Stuttgart.

Lohmann, R., & Jeroszko, R. (1983). *Broad Specification Fuels Technology Program Phase I*.

Matalon, M. (2007). Intrinsic Flame Instabilities in Premixed and Nonpremixed Combustion. *Annu. Rev. Fluid Mech*, *39*, 163–91. http://doi.org/10.1146/annurev.fluid.38.050304.092153

Maurice, L. Q., Lander, H., Edwards, T., & Harrison, W. E. (2001). Advanced aviation fuels: A look ahead via a historical perspective. *Fuel*, *80*(5), 747–756. http://doi.org/10.1016/S0016-2361(00)00142-3

McBride, S. G. and B. J. (1994). *Computer Program for Calculation of Complex Chemical Equilibrium Compositions and Applications*.

Meeks, E., Naik, C. V., Puduppakkam, K. V., Modak, A., Egolfopoulos, F. N., Tsotsis, T., & Westbrook, C. K. (2011). Experimental and Modeling Studies of the Combustion Characteristics of Conventional and Alternative Jet Fuels. Final Report, (May). Retrieved from http://hdl.handle.net/2060/20110012013

Metghalchi, M., & Keck, J. C. (1982). Burning Velocities of Mixtures of Air with Methanol, Isooctane, and Indolene at High Pressure and Temperature. *Combustion and Flame*, *48*, 191 – 210.

Mittal, G., & Sung, C. J. (2006). Aerodynamics inside a rapid compression machine. *Combustion and Flame*, *145*(1-2), 160–180. http://doi.org/10.1016/j.combustflame.2005.10.019

Montgomery, D. C. (2003). *Applied Statistics and Probability for Engineers Third Edition*. *Phoenix Usa* (Vol. 37). http://doi.org/10.2307/1269738

Naik, C. V., Westbrook, C. K., Herbinet, O., Pitz, W. J., & Mehl, M. (2011). Detailed chemical kinetic reaction mechanism for biodiesel components methyl stearate and methyl oleate. *Proceedings of the Combustion Institute*, *33*(1), 383–389. http://doi.org/10.1016/j.proci.2010.05.007

Nair, S., & Paulose, H. (2014). Emergence of green business models: The case of algae biofuel for aviation. *Energy Policy*, *65*, 175–184. http://doi.org/10.1016/j.enpol.2013.10.034

Padilha, E. (2015). Perspectivas Setor de Aviação Civil no Brasil - 2015 a 2035. Retrieved from http://www.aviacao.gov.br/

Pereira, F. M., Oliveira, a. a M., & Fachini, F. F. (2011). Maximum superadiabatic temperature for stabilized flames within porous inert media. *Combustion and Flame*, *158*(11), 2283–2288. http://doi.org/10.1016/j.combustflame.2011.04.001

Poinsot, T., & Veynante, D. (2005). *Theoretical and Numerical Combustion* (Second).

Rahim, F., Eisazadeh-Far, K., Parsinejad, F., Andrews, R. J., & Metghalchi, H. (2008). A thermodynamical model to calculate burning speed of methne-air-diluent mixtures. *International Journal of Thermodynamics*, *11*(4), 151–160.

Ranzi, E., Frassoldati, A., Grana, R., Cuoci, A., Faravelli, T., Kelley, A. P., & Law, C. K. (2012). Hierarchical and comparative kinetic modeling of laminar flame speeds of hydrocarbon and oxygenated fuels. *Progress in Energy and Combustion Science*, *38*(4), 468–501. http://doi.org/10.1016/j.pecs.2012.03.004

Rosfjord, T. (1984). *Aviation-Fuel Property Effects on Combustion*.

Settles, G. S. (2001). *Schlieren and Shadowgraph Techniques*. Springer.

Shepherd, J. E., Nuyt, C. D., & Lee, J. J. (2000). Flash Point and Chemical Composition of Aviation Kerosene (Jet A), (Explosion Dynamics Laboratory Report FM99-4), 38. Retrieved from http://caltechgalcitfm.library.caltech.edu/48/01/galcit_fm99-4.pdf

Simmie, J. M. (2003). Detailed chemical kinetic models for the combustion of hydrocarbon fuels. *Progress in Energy and Combustion Science*, *29*(6), 599–634. http://doi.org/10.1016/S0360-1285(03)00060-1

Soares, R. W. (2011). Biocombustíveis: Possíveis Benefícios Ambientais, Econômicos e Sociais. São José dos Campos/Brasil: Seminário Combustíveis Alternativos para Aviação/DCA-BR.

Sotelo-Boyás, R., Trejo-Zárraga, F., & Felipe de Jesús Hernández-Loyo. (2012). Hydroconversion of Triglycerides into Green Liquid Fuels. http://doi.org/10.5772/48710

Turns, S. R. (2012). *An Introduction to Combustion* (Third). New York: McGraw Hill.

Vasu, S. S., Davidson, D. F., & Hanson, R. K. (2008). Jet fuel ignition delay times: Shock tube experiments over wide conditions and surrogate model predictions. *Combustion and Flame*, *152*(1-2), 125–143. http://doi.org/10.1016/j.combustflame.2007.06.019

Vasu, S. S., Davidson, D. F., & Hanson, R. K. (2009). High-pressure shock tube experiments and modeling of n-dodecane/air ignition. *Shock Waves, IV*, 293–298.

Vukadinovic, V., Habisreuther, P., & Zarzalis, N. (2013). Influence of pressure and temperature on laminar burning velocity and Markstein number of kerosene Jet A-1: Experimental and numerical study. *Fuel*, *111*, 401–410. http://doi.org/10.1016/j.fuel.2013.03.076

Warnatz, J., Maas, U., & Dibble, R. W. (2006). *Combustion - Physical and Chemical Fundamentals, Modeling and Simulation, Experiments, Pollutant Formation*. *New York*. Retrieved from http://books.google.com/books?hl=en&lr=&id=2bgQBg-nOpoC&oi=fnd&pg=PA1&dq=Combustion+Physical+and+chemical+fundamentals,+modeling+and+simulation,+experiments,+pollutant+formation&ots=MccdCmtDBz&sig=9qb73Ig-8DQNOYCMvzLWnJ02lXo

Werler, M., Cancino, L. R., Schiessl, R., Maas, U., Schulz, C., & Fikri, M. (2015). Ignition delay times of diethyl ether measured in a high-

pressure shock tube and a rapid compression machine. *Proceedings of the Combustion Institute*, *35*(1), 259–266. http://doi.org/10.1016/j.proci.2014.06.143

Westbrook, C. K., Pitz, W. J., Herbinet, O., Curran, H. J., & Silke, E. J. (2009). A comprehensive detailed chemical kinetic reaction mechanism for combustion of n-alkane hydrocarbons from n-octane to n-hexadecane. *Combustion and Flame*, *156*(1), 181–199. http://doi.org/10.1016/j.combustflame.2008.07.014

Williams, F. A. (1986). *Combustion Theory* (Second). Boston: Perseu Books.

Zabetakis, M. G. (1965). *Flammability characteristics of combustible gases and vapors*. (B. O. M. Us Dept Of The Interior, Ed.)*Bulletin* (Vol. 627). US Dept. of the Interiror, Bureau of Mines. Retrieved from http://oai.dtic.mil/oai/oai?verb=getRecord&metadataPrefix=html&identifier=AD0701576

Zhang, Q., Noble, D. R., Meyers, A., Xu, K., & Lieuwen, T. (2005). Characterization of Fuel Composition Effects in H2/CO/CH4 Mixtures Upon Lean Blowout. *Aerospace Engineering*, 1–13. http://doi.org/10.1115/1.2718566